Temperature Modulation and Local Heat Transfer in the Microcirculation

by

Liang Zhu

A dissertation submitted to the Graduate Faculty in Engineering in partially fulfillment of the requirements for the degree of Doctor of Philosophy, The City University of New York

1995

This manuscript has been read and accepted for the Graduate Faculty in Engineering in satisfaction of the dissertation requirement for degree of Doctor of Philosophy.

9/7/95
Date

Professor Sheldon Weinbaum
Chair of Examining Committee

9/7/95
Date

Professor Gerard G. Lowen
Executive Officer

Professor Sheldon Weinbaum

Professor Daniel E. Lemons

Professor Latif M. Jiji

Professor Lisa X. Xu

Professor Steven House

Supervisory Committee

The City University of New York

Abstract

Temperature Modulation and Local Heat Transfer in the Microcirculation

by

Liang Zhu

Advisers: Professor Sheldon Weinbaum

Professor Daniel E. Lemons

In this dissertation an experimental study was conducted to investigate axial thermal equilibration between thermally significant countercurrent artery-vein pairs in an exteriorized tissue preparation, rat cremaster muscle. An accurate three-dimensional model is developed for a two-dimensional tissue preparation with arbitrarily embedded countercurrent vessels to interpret the experimental results. The rat cremaster muscle preparation was also used to measure the hyperthermic response of individual microvessels subject to local heating and the enhancement in the effective thermal conductivity due to blood perfusion has been calculated for this hyperthermic response under normal and drug induced vessel dilation conditions, using the expression for k_{eff} in the Weinbaum-Jiji bioheat equation.

A brief introduction to temperature modulation and local heat transfer in the microcirculation is given in chapter 1. In chapter 2, a three-dimensional analytical solution is developed for treating two or more axially interacting countercurrent vessels arbitrarily

embedded in a thin tissue preparation with surface convection as a model for the heat exchange between vessels and the tissue in rat cremaster muscle. The solution was used to guide the design of our experiments in which the axial temperature distribution along thermally significant countercurrent microvessels was measured for the first time in a living tissue.

In chapter 3, a new experimental approach is described for obtaining the first direct measurements of the axial countercurrent thermal equilibration in a rat cremaster muscle preparation using high-resolution infrared thermography. Detailed surface temperature measurements were obtained from this preparation in which vasoactive pharmacological agents were employed to change the local blood flow Peclet number in the feeding artery. The theoretical model developed in chapter 2 is modified to include axial conduction in the tissue and the presence of the supporting glass slide. This modified model is employed to interpret the experimental results. It is shown that the axial thermal equilibration depends significantly on the tissue inlet temperature, the blood flow Peclet number and the environmental convective coefficient. The theoretical model also predicts the range of conditions in which conduction or countercurrent blood flow is the dominant mode for axial thermal equilibration.

Chapter 4 describes the use of the rat cremaster muscle to study the dynamic vasomotor response of the microcirculation to local heating. Experimental studies were performed on cremaster 1A, 2A, 3A and 4A arterioles to assess the measurements of the *in vivo* changes in diameter and blood flow when the temperature was raised in 2 degree increments from 34 to 42 ℃. These experimental measurements as well as detailed anatomic

data were used to evaluate the Weinbaum-Jiji expression for the enhancement in the effective conductivity. The theory predicts that significant enhancement in k_{eff} starts to occur for vessels that are 70μm in diameter or larger. Results also indicate that the Weinbaum-Jiji expression for k_{eff} is valid in cremaster muscle for both normal and hyperthermic conditions provided the largest vessels are < 200μm in diameter.

To My Husband

Yong

Acknowledgments

The author wishes to express her deepest gratitude and appreciation to Professor Sheldon Weinbaum and Professor Daniel E. Lemons for their constant support, encouragement, patient and guidance which made it possible for the author to enter the frontier of this promising and challenging field of research.

The author would also like to thank Professor Lisa X. Xu and Professor Latif M. Jiji for many helpful discussions and to thank Mr. Peter Butler, Ms. Ji Song and Mr. Yulong Wu for their help and cooperation with the experimental portions of this research.

The author is grateful to Professor Gerard G. Lowen for handling administrative details in such a warm and friendly manner.

This research was supported by NFH grant CBT-8702582, NIF grant 5R01 HL2609 and PSC-CUNY grant 664441.

Table of Contents

List of Symbols

Bi	Biot number, $h\rho_w^*/k_t$
C_f	specific heat of blood
C_{sa}, C_{sv}	source strength
D	half width of tissue
h	thermal convection coefficient
H	total thickness of tissue
k	thermal conductivity
K'	ratio of conductivities of vessel to tissue
l	vessel center to center spacing
L	equilibration length
Nu_a	Nussel number defined in equation (2.23)
q_a	heat transfer per unit length of vessel in equation (2.21)
Pe	Peclet number of blood vessel
r	radial coordinate
Sa	eccentricity of vessel in tissue
T	temperature
u	average blood flow velocity
$\tilde{u}$	ratio of u_v to u_a
V	centerline red cell velocity
W	Green's function
x, y, z	Cartesian coordinates

Greek Symbols

Γ	boundary
γ_f	density of blood
θ	dimensionless temperature
θ_{a0}	dimensionless artery bulk temperature at z=0
λ	eigenvalue
ξ, η	coordinates of heat source
ρ	radial coordinate
ρ_w	dimensionless radius of vein
σ	shape factor
ϕ, ψ	polar angle in cylindrical coordinate
Ω	domain inside boundary Γ

Subscript

a	artery (or single vessel)
b	bulk
f	fluid in vessels
g	glass
s	source
t	tissue
v	vein
w	wall

List of Tables and Figures

Figure

Chapter 1. Introduction

It is well known that local blood flow and vascular geometry play an important role in the heat transfer within the bodies of mammals and the regulation of core temperature. How local microvascular blood flow controls the local thermal conductivity of tissue and how local tissue temperature regulates local blood flow have been subjects of continuous interest for over half a century.

Most investigations of vascular heat exchange in humans and other mammals prior to 1980 examined the heat transfer between the large countercurrent arteries and veins in the limbs [8, 27, 29, 31]. Skin temperature distributions along the axis of the human arm, around the circumference of the forearm, and through the center of the forearm were examined by Pennes [29] in 1948. These studies were used to quantitatively analyze the influence of cutaneous and muscle blood flow on skin temperature and became the basis for the mathematical model, the Pennes bioheat equation. Bazett *et al.* [8] showed that temperatures in the major axial arteries and veins of the human arm were influenced by environmental temperature and they suggested that heat exchange between these vessels served a heat conservation function. Scholander [31] demonstrated the ability of one structure, a vascular rete, to thermally isolate the sloth extremity from the central body and thus enhance central heat conservation. The importance of countercurrent heat exchange was examined by Mitchell and Myers [27] who developed a limb heat transfer model that treated the central artery and vein as a one-dimensional countercurrent heat exchanger with constant vessel radius. They concluded that very little heat could be conserved in the deep

vessels by the mechanism of countercurrent heat exchange. Although these early observations were important in introducing the concept of arterial-venous heat exchange, they neither correctly explained how and when heat transfer actually occurred in a complicated vascular network nor did they perform the experiments at the microvascular level.

Several quantitative continuum models have been developed for interpreting existing experimental data. Most of these models combine experimental and theoretical studies to elucidate how and where vascular heat transfer occurs. The first quantitative relationship that described heat transfer in living tissue was proposed by Pennes [29] in 1948. Reasonable agreement between the theory and experimental results was obtained although the fundamental hypothesis on which this equation rests are doubtful or have never been confirmed. This equation assumed a uniform perfusion source term that supposedly described blood-tissue heat transfer occurring in the capillary beds. This fundamental assumption has been questioned by several investigators since 1980. Chen and Holmes [12] first showed, using simple theoretical models, that thermal equilibration occurred in 50 to 500 μm diameter vessels and not in the capillary beds. Later models by Weinbaum *et al.* [37] suggested that the primary mechanism by which the microvascular blood flow alters the tissue heat transfer is incomplete countercurrent exchange in the thermally significant microvessels. A new fundamental bioheat transfer equation was derived by Weinbaum and Jiji [36], which combined the convective effect of countercurrent pairs and capillary bleed-off from these vessels with the traditional conduction term and showed that these effects could be represented as an enhancement in thermal conductivity, k_{eff}. The Weinbaum-Jiji

theory predicts that for animals at rest the blood flow contribution to k_{eff} is due to the larger countercurrent microvessels. There is relatively little enhancement in conductivity in tissue regions where all the microvessels are 50 μm in diameter or smaller except at very high flow rates where the blood flow rate is increased by an order of magnitude or more above resting conditions, such as during exercise or local hyperthermia.

Since 1980, several *in vivo* and *in vitro* experiments have been performed to elucidate the difference between those theoretical models and the effect of blood flow on tissue-vessel heat exchange. In Weinbaum *et al.* [37] thermocouple traverses across a rabbit thigh were performed *in vivo* in order to show the importance of countercurrent heat exchange. The arterial temperature was found to be nearly equal to the venous temperature for any countercurrent pair encountered along the traverse. Subsequently, Lemons *et al.* [25] obtained detailed temperature profiles which strongly supported the premise in the Weinbaum-Jiji equation that thermal equilibration occurred in the larger countercurrent microvessels. High resolution temperature measurements in the vicinity of numerous vessels of 50 to 500 μm in diameter, were reported for a rabbit thigh. The smallest vessel size which could maintain measurable temperature differences with the tissue was found to be about 100 μm in diameter for arteries and 400 μm in diameter for veins, and the temperature differences were only of the order of 0.1 to 0.2 °C. Furthermore, for vessels smaller than 100 μm in diameter it would be extremely difficult to measure axial temperature profiles using the microthermocouple technique. Crezee *et al.* [15] inserted a small plastic tube into the tissue of an excised bovine kidney and measured the disturbance in the temperature field in a plane perpendicular to the tube when heated water was circulated through it, and the

kidney cortex was perfused at different rates. These investigators also used thermocouples to map the temperature distribution in the tissue of isolated perfused bovine tongues at various perfusion rates [14]. The temperature measurements in these experiments were found to agree better with predictions of the Weinbaum-Jiji model using k_{eff} than predictions of the Pennes equation. Roemer *et al.* [30] measured steady state temperature profiles in canine thighs heated by scanned focused ultrasound. A comparison was made with both Pennes and Weinbaum-Jiji models, and the results were a better qualitative agreement with the former. However, these experiments were performed either *in vitro* with saline perfused blood vessels or *in vivo* without blood perfusion control. No investigator has been able to perform experiments in which axial temperature profiles and axial thermal equilibration in different sized microvessels (<100 μm dia.) are measured along the length of an arterial network in an *in vivo* tissue preparation or to evaluate how this equilibration is related to the local blood perfusion.

The effect of blood flow on vessel-tissue heat exchange was also examined in several experimental studies in which the effective thermal conductivity of the perfused tissue was measured using heat clearance techniques [2, 7, 28, 33, 41]. A self-heated thermistor probe was placed in the tissue and the local blood perfusion rate was either predicted using various heat transfer models that relate the measured conductivity to perfusion rate or estimated by comparison with *in vitro* measurements in which the flow to an entire artificially perfused organ was measured rather than the local perfusion in the vicinity of the probe. Two recent investigations [1, 41] have tried to relate the vascular anatomy of the renal cortex to the conductivity of the perfused tissue using the expression for the effective conductivity derived

in Weinbaum and Jiji [36] for countercurrent heat exchange between thermally significant artery-vein pairs in the microcirculation. The Weinbaum-Jiji theory is difficult to apply to this organ because of the complexity of the vascular anatomy and the fact that, unlike skeletal muscle tissue, the arteries and veins in the renal cortex do not occur primarily as countercurrent pairs. It was therefore necessary to develop an experimental approach which permited simultaneous observation of the temperature, flow and diameter of countercurrent microvessels in the muscle so that one would be able to relate the effective conductivity to the microvascular geometry and flow and to show the relative contribution of conduction, capillary perfusion and the countercurrent convection mechanism.

Local temperature and blood flow are reciprocally dependent. As was mentioned above, when diameter changes occur in a microvascular network, the heat transfer within that network must also be affected as a result of the enhancement in thermal conductivity. The new tissue temperature, on the other hand, will alter the smooth muscle function, leading to vasodilation or vasoconstriction and this results in a changed blood flow rate [34]. Since heat transfer is sensitive to blood vessel dimension and flow rate, it is important to consider some conditions or factors that will predictably alter microvascular dimensions and flow rate. Heat stress and hyperthermia are factors that act both locally and via central reflexes to alter local vascular geometry and to modify the total blood flow rate through the entire microvascular network. Alterations in temperature in normal conditions or during hyperthermia application may cause vessels to change their tone via direct effects on vascular smooth muscle or indirectly by altering the vascular response to endothelial factors, hormones and neurotransmitters [34]. There have been only a few prior experimental

investigations to study microvascular heat transfer and the enhancement in conductivity that is associated with the hyperemic response to hyperthermia. Two related studies are the experiments by Jain and Ward-Hartley [23] and Hogan *et al.* [21]. In the first study the rabbit ear chamber was used to examine the blood flow response to heating of the tumor microcirculation. The purpose of this experiment was to explore hyperthermia as a cancer treatment modality in which the tumor circulation is arrested and not to examine the change in local tissue heat transfer that results from the microvascular changes in flow. The tumor microvessels are also highly irregular and do not occur as countercurrent pairs [23]. The second study examined the effect of moderate heating up to 38 ^{0}C on the rat cremaster muscle after sympathetic nerve blockade or sympathectomy. This investigation did not control pH, PO_2 and PCO_2 and vasoconstriction was observed with elevated temperature in contrast to the hyperemic response that one would ordinarily anticipate for hyperthermia and observed in the present experiments. At present there is no experimental approach for studying the changing macroscopic thermal behavior of tissue that results from the dynamic vasomotor response of the microcirculation to local heating or hyperthermia.

Most investigators usually examine vascular heat transfer in the limbs, renal cortex or bovine tongues rather than in two-dimensional tissue preparations. Rabbit ear, frog mesentery, rat cremaster muscle, hamster check pouch, are a few of the more widely used two-dimensional tissue preparations. These preparations have been extensively used in the past to measure key parameters in microvascular beds (e.g. hematocrit distribution), in mass transfer studies using fluorescent tracers, in studies of vasoactive drugs, and in other applications. These preparations are nearly transparent and of uniform thickness. In such

preparations the blood flow in several successive generations of vessels can be examined. In the experiments described herein, the rat cremaster muscle (Figure 1) was used because the feeding blood vessels are countercurrent artery-vein pairs. Depending on rat age and size, the feeding arteriole varies from 50 to 200 μm in diameter. Previous theoretical studies suggest that these are the most important vessels in blood-tissue energy exchange. However, no experiments to study microvascular heat transfer have been successfully performed in microvascular tissue preparations. This is mostly due to the interference of the temperature measuring devices on the tissue temperature field surrounding the microvessels, since the spatial temperature fluctuation is of the same order or smaller than the sensing volume of available temperature measuring devices such as thermocouples.

In this dissertation we have developed a non-invasive high-resolution technique to study heat exchange at the microvascular level. High-resolution infrared thermography is a noninvasive technique that can be used to measure the detailed *in vivo* surface temperature field above individual microvessels in a two-dimensional tissue preparation. Furthermore, vasoconstrictors and vasodilators, such as norepinephrine (NE) and sodium nitroprusside, respectively, can be added in a graded manner to change the blood flow through the whole tissue preparation. It is, therefore, possible to experimentally measure the axial thermal equilibration length of the feeding countercurrent vessel pair and to examine the relationship between this length and the blood flow rate in the tissue preparation. The rat cremaster muscle preparation was used here to not only obtain the direct experimental identification of the heat transfer site but to also quantify the parameters that determine which blood vessels are thermally significant. The preparation was also used to measure the centrally and

locally mediated hyperthermic response of individual microvessels in skeletal muscle tissue subject to local heating in a tissue bath where muscle temperature and blood flow could be accurately measured. The rat cremaster muscle preparation has the important advantage that, unlike the renal cortex, all 1A and 2A vessels and most 3A vessels appear as countercurrent artery-vein pairs. One is thus able to accurately measure countercurrent vessel number density, diameter, and blood flow in several successive generations of vessels. Therefore, it provides a realistic *in vivo* model for evaluating the enhancement of thermal conductivity due to countercurrent flow and the possibility of relating this enhancement to the centrally and locally mediate changes in the vasomotor tone of the microcirculation.

The primary objectives of this research were : (a) To develop a theoretical model to study the thermal equilibration between two or more vessels embedded in a uniform two-dimensional tissue preparation with surface convection. This model was used to show the feasibility of our experimental study for the first direct measurements of the axial thermal equilibration in rat cremaster muscle. (b) To examine the axial countercurrent thermal equilibration in microvessels between 40 and 200 μm in diameter in an exteriorized rat cremaster muscle using high resolution infra-red thermography. The theoretical model mentioned above is modified to include axial conduction in the tissue and the presence of the supporting glass slide. This modified model was employed to interpret the experimental results. (c) To develop a combined theoretical and experimental approach for studying the dynamic vasomotor response of the microcirculation to changes in temperature. The observed changes in vascular diameter and flow due to local heating are combined with the Weinbaum-Jiji equation to predict the enhancement in thermal conductivity and to establish

the limits of validity of the Weinbaum-Jiji theory. This dissertation is divided into three major chapters, one devoted to each of the three related principal objectives mentioned above.

Chapter 2. Model for Heat Transfer from Embedded Blood Vessels in a Two-Dimensional Tissue Preparation

In this chapter, an approximate three-dimensional solution for the heat transfer from a periodic array of blood vessels in a tissue preparation of uniform thickness with surface convection is constructed using a newly derived fundamental solution for a Green's function for this flow geometry. This approximate solution is exact when the ratio K' of the blood to tissue conductivity is unity and a highly accurate approximation when $K' \neq 1$. Having demonstrated the accuracy of the approximate solution, we apply this basic solution to develop a model for the heat transfer from a countercurrent artery-vein pair in an exteriorized rat cremaster muscle preparation. The numerical results provide important new insight into the design of microvascular experiments in which the axial variation of the thermal equilibration in microvessels can be measured for the first time.

2.1 Introduction

The heat exchange between countercurrent microvascular artery-vein pairs has attracted widespread attention since the combined theoretical and experimental studies [25, 36, 37] first suggested that this might be the dominant heat transfer mechanism in local microvascular blood-tissue heat transfer. Earlier theoretical predictions by Chen and Holmes [12] and Chato [10] had shown that thermal equilibration between blood and tissue occurred primarily in vessels that were 50 to 500 μm in diameter. While the experimental evidence in [25] strongly supports the hypothesis in [36, 37] as to the importance of countercurrent

microvascular heat exchange, there has been no experimental study that has measured this thermal equilibration in an *in vivo* tissue preparation.

Microvascular blood flow is commonly examined in a variety of two-dimensional tissue preparations. Rat cremaster muscle is one such tissue preparation. In this chapter we develop a theoretical model to study the thermal equilibration between two or more vessels embedded in a uniform two-dimensional tissue preparation with surface convection. This is a simplified model for our experimental studies using the exteriorized rat cremaster muscle preparation.

Many simplified models have been previously developed to study the heat transfer between vessels or pipes and a surrounding medium. The problem of a single vessel in a semi-infinite medium with uniform temperature or uniform heat flux boundary conditions was considered in [20, 32]. This approach was used by DiFelice and Bau [16] to describe the convective heat transfer between two buried pipes in an infinite medium. Recent interest in modeling countercurrent vessels in perfused tissue and limbs has motivated several recent solutions for two small-eccentricity vessels (equal or unequal) embedded in a cylinder in which both the vessels and the cylinder surface were at constant temperature in the cross-sectional plane [5, 43]. Zhu *et al.* [42] treated a similar problem but developed a new solution approach, which allowed both the vessels and the cylinder surface to have axially varying non-uniform convective boundary conditions. The latter theory was an extension of the exact solution of Wissler [39] for the perfect countercurrent heat transfer between two vessels with parabolic flow profiles and non-uniform wall temperature in an infinite medium, where the artery, vein and tissue had the same linear axial temperature gradient. Recently,

Wu *et al.* [40] have constructed a new analytic solution approach for treating any finite number of vessels arbitrarily placed in a cylinder with surface convection. This last solution can be used to more realistically model the heat transfer between the major axial arteries and veins in the limb, since it is not limited to small eccentricities.

There has been no previous model or solution approach which is suitable for treating the heat transfer between vessels embedded in a thin two-dimensional tissue preparation representative of rat cremaster muscle. The techniques developed by previous investigators can not be applied to the mixed rectangular and cylindrical coordinate geometry. Our new solution approach is based on a newly derived fundamental solution for a Green's function for the heat transfer from a periodic array of blood vessels in a tissue preparation of uniform thickness with surface convection (Figure 2). This solution is exact when the ratio K' of the blood to tissue conductivity is unity and a highly accurate approximation when $K' \neq 1$. This basic solution is then applied to develop a model for the heat transfer from a countercurrent artery-vein pair in the rat cremaster muscle preparation.

2.2 Formulation

For the general case we consider two or more vessels embedded in a thin tissue layer of thickness $H=H_1+H_2$, as shown in Figure 3. A steady-state temperature field is assumed in both the vessels and the surrounding tissue. The axes of the vessels are perpendicular to the plane of the figure in the z direction. It is assumed that the velocity profile in the vessels is parabolic and the blood flow Peclet number >> 1. Thus, if the vessel length $L_{length} >> H$, axial conduction and end effects can be neglected [42].

The non-dimensional parameters are introduced as follows:

$$\rho_a=\frac{\rho_a^*}{\rho_{ar}^*},\ \rho_v=\frac{\rho_v^*}{\rho_{ar}^*},\ \rho_w=\frac{\rho_w^*}{\rho_{ar}^*},\ x=\frac{x^*}{\rho_{ar}^*},\ y=\frac{y^*}{\rho_{ar}^*},\ z=\frac{z^*}{\rho_{ar}^* Pe},\ H_{1,2}=\frac{H_{1,2}^*}{\rho_{ar}^*},\ D=\frac{D^*}{\rho_{ar}^*},$$

$$Pe=\frac{2\gamma_f C_f \rho_{ar}^* u_a}{k_f},\ Bi_{1,2}=\frac{h_{1,2}\rho_{ar}^*}{k_t},\ \theta_{a,v,t}=\frac{T_{a,v,t}-T_\infty}{T_{a0}-T_\infty},\ \bar{u}=\frac{u_v}{u_a}$$

here the subscripts a, v refer to artery and vein, asterisks denote dimensional variables, T_∞ is the environment temperature, and ρ^*_{ar} and ρ^*_w are the dimensional radii of the artery and vein. This coordinate system is sketched in Figure 3. To simplify the analysis, we assume that the temperature gradient $\partial\theta_{a,v}/\partial z$ in the convective term of the vessel energy equations can be approximated by the axial gradient of the vessel bulk temperatures, $d\theta_{ab,vb}/dz$ as previously justified in [42]. The simplified dimensionless governing equations and boundary conditions for the vessels and the tissue are

$$\frac{1}{\rho_a}\frac{\partial}{\partial\rho_a}\left(\rho_a\frac{\partial\theta_a}{\partial\rho_a}\right)+\frac{1}{\rho_a^2}\frac{\partial^2\theta_a}{\partial\phi_a^2}=(1-\rho_a^2)\frac{d\theta_{ab}}{dz},\qquad \rho_a\le 1 \tag{2.1}$$

$$\frac{1}{\rho_v}\frac{\partial}{\partial\rho_v}\left(\rho_v\frac{\partial\theta_v}{\partial\rho_v}\right)+\frac{1}{\rho_v^2}\frac{\partial^2\theta_v}{\partial\phi_v^2}=\bar{u}\left(1-\frac{\rho_v^2}{\rho_w^2}\right)\frac{d\theta_{vb}}{dz},\qquad \rho_v\le\rho_w \tag{2.2}$$

$$\frac{\partial^2\theta_t}{\partial x^2}+\frac{\partial^2\theta_t}{\partial y^2}=0,\quad \rho_a>1,\ \rho_v>\rho_w,\ -D\le x\le D,\ -H_2\le y\le H_1 \tag{2.3}$$

$$\theta_a=\theta_t,\qquad \rho_a=1 \tag{2.4a}$$

$$K'\frac{\partial\theta_a}{\partial\rho_a}=\frac{\partial\theta_t}{\partial\rho_a},\qquad \rho_a=1 \tag{2.4b}$$

$$\theta_v=\theta_t,\qquad \rho_v=\rho_w \tag{2.5a}$$

$$K'\frac{\partial\theta_v}{\partial\rho_v}=\frac{\partial\theta_t}{\partial\rho_v}, \qquad \rho_v=\rho_w \tag{2.5b}$$

$$\frac{\partial\theta_t}{\partial y}=-Bi_1\theta_t, \qquad y=H_1 \tag{2.6a}$$

$$\frac{\partial\theta_t}{\partial y}=Bi_2\theta_t, \qquad y=-H_2 \tag{2.6b}$$

For a periodic array of equally spaced vessels, as shown in Figure 2, there is no heat flow across the boundaries at $x=\pm D$. For vessel pairs whose spacing between pairs $2D$ is much larger than the tissue thickness H, this no flux boundary condition is also closely approximated. Thus, for either case we shall require the adiabatic condition:

$$\frac{\partial\theta_t}{\partial x}=0 \qquad x=\pm D \tag{2.7}$$

In Eqs.2.1 and 2.2, θ_{ab} and θ_{vb} are the artery and vein bulk temperatures that are defined as

$$\theta_{ab}=\frac{2}{\pi}\int_{-\pi}^{\pi}\int_0^1\theta_a(1-\rho_a^2)\rho_a\,d\rho_a\,d\phi_a \tag{2.8}$$

$$\theta_{vb}=\frac{2}{\pi\rho_w^2}\int_{-\pi}^{\pi}\int_0^{\rho_w}\theta_v\left(1-\frac{\rho_v^2}{\rho_w^2}\right)\rho_v\,d\rho_v\,d\phi_v \tag{2.9}$$

2.3 Solution for Single Vessel

In this section, two solutions are constructed for the temperature field within and surrounding a single vessel in a periodic array of blood vessels for the flow and tissue geometry depicted in Figure 2. The first employs a newly derived Green's function or fundamental solution that is placed at the origin of each vessel. This solution is exact only

when K'=1. The second is a significantly more complicated solution using an integral equation formulation of this Green's function. This latter solution is exact for all values of K'. The accuracy of the first solution for K'≠1 is examined by comparing it with the exact integral equation solution. It is shown that the approximate solution for K'≠1 is also highly accurate for most conditions of interest. The approximate solution is, therefore, used to construct the more general solution in section 2.4 for two or more eccentrically located vessels, shown in Figure 3.

2.3.1 Approximate Solution

The governing equations and boundary conditions for a single vessel are Eqs.2.1, 2.3, 2.4, 2.6, 2.7. The solution of Eq.2.1 for the vessel temperature θ_s can be decomposed into two parts, a particular solution $\theta_{p,s}$ and a general solution $\theta_{h,s}$ in the form of a Fourier series, whose superposition is given by

$$\theta_s = (\rho_s^2 - \frac{1}{4}\rho_s^4 - \frac{3}{4})\frac{1}{4}\frac{d\theta_{sb}}{dz} + \frac{a_{s0}}{2} + \sum_{j=1}^{\infty} a_{sj}\rho_s^j \cos(j\phi_s) \qquad (2.10)$$

Since j is a positive integer, this solution has no singular point.

We assume that the tissue temperature field can be constructed by placing an anisotropic line source of strength C_{ss} at the center of each vessel in the periodic array. This fundamental solution is given by

$$\theta_t = C_{ss} W(x,y:0,0) \qquad (2.11)$$

where W is a Green's function, which satisfies Laplace's equation in the rectangular region, $-D \le x \le D$ and $-H_2 \le y \le H_1$, except for the source point (0,0) at the center of the vessel and the

boundary conditions (2.6) and (2.7). The boundary value problem for this singular solution is

$$\begin{cases} \dfrac{\partial^2 W}{\partial x^2}+\dfrac{\partial^2 W}{\partial y^2}=\delta(x-\xi)\delta(y-\eta) & (2.12) \\ \dfrac{\partial W}{\partial x}=0 \qquad \text{at } x=\pm D & (2.13a) \\ \dfrac{\partial W}{\partial y}=\mp Bi_{1,2}W \qquad \text{at } y=\pm H_{1,2} & (2.13b) \end{cases}$$

where (ξ,η) are the coordinates of the source point. The solution to (2.12) for the Green's function W(x,y:0,0) is given in Appendix 1 by equation (A.12)

$$W=(C_1y+C_2)+\sum_{n=1}^{\infty}\frac{1}{D}\cos[\frac{n\pi}{2}]\cos[\sqrt{\lambda_n}(x-D)][A_1e^{\sqrt{\lambda_n}y}+B_1e^{-\sqrt{\lambda_n}y}] \qquad y\geq 0 \qquad (2.14a)$$

$$W=(D_1y+D_2)+\sum_{n=1}^{\infty}\frac{1}{D}\cos[\frac{n\pi}{2}]\cos[\sqrt{\lambda_n}(x-D)][A_2e^{\sqrt{\lambda_n}y}+B_2e^{-\sqrt{\lambda_n}y}] \qquad y\leq 0 \qquad (2.14b)$$

where the A_i, B_i, C_i, D_i, i=1,2 are constants, which depend on the Biot number and the tissue geometry, and are listed in (A.8) and (A.10) of Appendix 1 and the eigenvalues $\lambda_n=(n\pi/2D)^2$.

The coefficients a_{ij} in Eq.10 for the vessel temperature are determined by the matching conditions (4) for the continuity of temperature and heat flux on the vessel surface. For temperature continuity,

$$C_{ss}W(x,y:0,0)|_{\rho_s=1}=(\rho_s^2-\frac{1}{4}\rho_s^4-\frac{3}{4})\frac{1}{4}\frac{d\theta_{sb}}{dx}+\frac{a_{s0}}{2}+\sum_{j=1}^{\infty}[\rho_s^j a_{sj}\cos(j\phi_s)]|_{\rho_s=1} \qquad (2.15)$$

where in W(x,y:0,0), $x=\rho_s\cos\phi_s$, $y=\rho_s\sin\phi_s$. Multiplying both sides of (2.15) by $\cos(j\phi_s)$ and integrating from $-\pi$ to π, we obtain

$$a_{s0}=\int_{-\pi}^{\pi}[\frac{C_{ss}}{\pi}W(x,y:0,0)]|_{\rho_s=1}d\phi_s \qquad (2.16a)$$

$$a_{oj}=\int_{-\pi}^{\pi}[\frac{C_{oo}}{\pi}W(x,y:0,0)]\frac{\cos(j\phi_o)}{\rho_o^j}|_{\rho_o=1}d\phi_o \qquad j=1,2,.....\infty \tag{2.16b}$$

where the strength of the source C_{oo} still needs to be determined. Continuity of heat flux requires that

$$[C_{oo}\frac{\partial W(x,y\ :\ 0,0)}{\partial\rho_o}]|_{\rho_o=1}=\frac{K'}{4}\frac{d\theta_{oo}}{dx}+\sum_{j=1}^{\infty}[K'j\rho_o^{j-1}a_{oj}\cos(j\phi_o)]|_{\rho_o=1} \tag{2.17}$$

Multiplying both sides of Eq.2.17 by $\cos(j\phi_o)$ and integrating from $-\pi$ to π, we obtain

$$C_{oo}=\frac{K'\pi}{2}\frac{d\theta_{oo}}{dx} \tag{2.18a}$$

$$a_{oj}=\frac{1}{K'}\int_{-\pi}^{\pi}[\frac{C_{oo}}{\pi}\frac{\partial W(x,y\ :\ 0,0)}{\partial\rho_o}]\frac{\cos(j\phi_o)}{j\rho_o^{j-1}}|_{\rho_o=1}d\phi_o \qquad j=1,2,.....\infty \tag{2.18b}$$

Eq.2.18a is an integral average constraint requiring that there be a global conservation of energy for the total heat flux crossing the vessel surface $\rho_o=1$. In contrast, Eq.2.18b is a local heat flux condition. Eqs.2.16b and 2.18b provide two independent relations for the a_{oj} coefficients. Thus, for both temperature and heat flux to be continuous locally at $\rho_o=1$ these two expressions for the a_{oj} must be equal. Equating (2.16b) and (2.18b), we have

$$\frac{C_{oo}}{\pi}\int_{-\pi}^{\pi}[W(x,y:0,0)\frac{K'}{\rho_o^j}-\frac{\partial W(x,y:0,0)}{\partial\rho_o}\frac{1}{j\rho_o^{j-1}}]\cos(j\phi_o)|_{\rho_o=1}d\phi_o=0 \qquad j=1,2,.....\infty \tag{2.19}$$

In Appendix 2, it is shown that Eq.2.19 is exactly satisfied only when $K'=1$. The solution given by Eqs.2.10, 2.11, 2.16 and 2.18a is, therefore, exact when $K'=1$ and approximate when $K'\neq1$. For $K'\neq1$ it satisfies the outer boundary conditions since θ_t is proportional to the Green's function 2.14 which satisfies the outer boundary conditions, while at $\rho_o=1$ only

the continuity of temperature is satisfied locally. However, as will be shown in section 2.3.3, the global constraint on heat flux (2.18a) provides a very strong compatibility condition and the approximate solution for K'≠1 is remarkably accurate for nearly all flow conditions of interest.

To complete the analysis, we shall obtain expressions for the bulk temperature, the conduction shape factor σ_s and the Nusselt number Nu_s. Substituting (2.10) into (2.8), we obtain

$$\theta_{sb} = -\frac{11}{96}\frac{d\theta_{sb}}{dz} + \frac{a_{s0}}{2} \tag{2.20}$$

where a_{s0} is proportional to $d\theta_{sb}/dz$ from (2.16a) and (2.18a). Eq.2.20 can be integrated axially subject to an entrance condition at $z=0$. Once $\theta_{sb}(z)$ is known, Eqs.2.10 and 2.11 provide the complete solution for the temperature field in both the vessel and the tissue. The integrals for the a_{sj} in Eq.2.16 involve only a single integration that requires insignificant computational time.

The shape factor σ_s for heat transfer between a vessel in the periodic array and the tissue layer is defined by

$$\sigma_s = \frac{q_s}{2\pi K_t (T_{sb} - T_\infty)} = -\frac{K'}{4}\frac{\dfrac{d\theta_{sb}}{dz}}{\theta_{sb}} \tag{2.21}$$

Here q_s is the heat transfer per unit vessel length and is equal to $-\gamma C_f \pi \rho^*_\infty{}^2 u_s (dT_{sb}/dz^*)$. One observes from Eq.2.20 and 2.21 that σ_s depends only on the single unknown coefficient a_{s0} which is given by (2.16a). Thus, substituting (2.20) into (2.21) and using (2.16a) and (2.18a), one obtains

$$\sigma_s = -\frac{K'}{4}\frac{1}{-\frac{11}{96}+\frac{K'}{2}\int_{-\pi}^{\pi} W(x,y:00)\big|_{\rho_s=1}d\phi_s} \tag{2.22}$$

(2.22) provides a single closed form expression for the shape factor σ_s.

The vessel Nusselt number is defined by

$$Nu_s = \frac{q_s}{\pi K_f (T_{sb}-T_{sw})} = -\frac{1}{2}\frac{\frac{d\theta_{sb}}{dz}}{\theta_{sb}-\theta_{sw}} \tag{2.23}$$

where, θ_{sw}, the dimensionless mean wall temperature of the vessel, is given by

$$\theta_{sw} = \frac{1}{2\pi}\int_{-\pi}^{\pi}\theta_s(1,\phi_s)d\phi_s = \frac{a_{s0}}{2} \tag{2.24}$$

Substituting (2.24) into (2.23), we obtain

$$Nu_s = 48/11 \tag{2.25}$$

This Nusselt number is the same value as for a fully developed temperature profile in a pipe with constant heat flux to the environment. One can show that the homogeneous terms in the summation in (2.10) do not contribute to Nu_s.

2.3.2 Exact Solution for K'≠1 Using Green's Theorem

Since the solution in section 2.3.1 is exact only when K'=1, we shall also construct for comparison an exact solution, valid for all values of K'. This solution will be based on a generalization of the Green's function (2.12), which is valid at any point in the domain, and the application of Green's theorem. The resulting integral equation will be reduced to a linear system of matrix equations for the unknown coefficients a_{ij} that appear in (2.10) after applying the boundary and matching conditions at the vessel surface.

If θ_t satisfies Laplace's equation and $W(x,y:\xi,\eta)$ is a Green's function with a source point (ξ,η) located within the tissue region, $-D \le x \le D$ and $-H_1 \le y \le H_2$, Green's theorem reduces to

$$-\theta_t(x,y) = \frac{1}{C}\oint_\Gamma [W(x,y:\xi,\eta)\frac{\partial \theta_t(\xi,\eta)}{\partial n} - \theta_t(\xi,\eta)\frac{\partial W(x,y:\xi,\eta)}{\partial n}]d\Gamma \qquad (2.26)$$

where C is a constant, which is equal to 1 if (x,y) is an inner point of the tissue region. When (x,y) is a boundary point C is given by the formula

$$C = \frac{\textit{included interior angle}}{2\pi}$$

The generalization of the Green's function $W(x,y:\xi,\eta)$ which satisfies boundary conditions (2.13) for a source at any point (ξ,η) is given by equation (A.11) in Appendix 1. Since the Green's function already satisfies the outer boundary conditions (2.13), one can show that the integral along the outer boundary, where conditions (2.13) apply, vanishes and (2.26) reduces to

$$\theta_t(x,y) = \frac{1}{C}\int_{\Gamma_{out}} [\theta_t(\xi,\eta)\frac{\partial W(x,y:\xi,\eta)}{\partial n} - W(x,y:\xi,\eta)\frac{\partial \theta_t(\xi,\eta)}{\partial n}]d\Gamma$$

$$= -\frac{1}{C}\int_{-\pi}^{\pi} [\theta_t(r_a,\psi_a)\frac{\partial W(x,y:r_a,\psi_a)}{\partial r_a} - W(x,y:r_a,\psi_a)\frac{\partial \theta_t(r_a,\psi_a)}{\partial r_a}]r_a|_{r_a=1}d\psi_a \qquad (2.27)$$

where the source point $(\xi,\eta)=(r_a\cos\psi_a,\ r_a\sin\psi_a)$. Since the integral in (2.27) is along the vessel surface, Eq.2.10 for θ_a can be used to evaluate both θ_t and $\partial\theta_t/\partial r_a$ in the integral on the right-hand side of (2.27). Applying matching conditions (2.4a) and (2.4b), one obtains

$$\theta_f(x,y)=-\frac{1}{C}\int_{-\pi}^{\pi}\left\{\frac{a_{s0}}{2}+\sum_{n=1}^{\infty}\left[r_s^n a_{sn}\cos(n\psi_s)\right]\right\}\frac{\partial W(x,y:r_s,\psi_s)}{\partial r_s}$$
$$-K'W(x,y:r_s,\psi_s)\left\{\frac{1}{4}\frac{d\theta_{sb}}{dz}+\sum_{n=1}^{\infty}\left[nr_s^{n-1}a_{sn}\cos(n\psi_s)\right]\right\}|_{r_s=1}d\psi_s \qquad (2.28)$$

Eq.2.28 is an integral equation to determine the tissue temperature field except that the coefficients a_{sn} are unknown. Choosing (x,y) as a point on the vessel surface, i.e. $(x,y)=(\rho_s\cos\phi_s,\ \rho_s\sin\phi_s)|_{\rho_s=1}$ and requiring that the left side of (2.28) be given by (2.10), one obtains

$$\frac{a_{s0}}{2}+\sum_{j=1}^{\infty}a_{sj}\cos(j\phi_s)=$$
$$-2\int_{-\pi}^{\pi}\left\{\frac{a_{s0}}{2}\frac{\partial W}{\partial r_s}+\sum_{n=1}^{\infty}\cos(n\psi_s)a_{sn}\left[\frac{\partial W}{\partial r_s}-K'nW\right]-\frac{1}{4}\frac{d\theta_{sb}}{dz}K'W\right\}|_{r_s=1,\rho_s=1}d\psi_s \qquad (2.29)$$

We now multiply both sides of (2.29) by cos ($j\phi_s$) and integrate from $-\pi$ to π, this yields

$$a_{sj}=-\frac{2}{\pi}\int_{-\pi}^{\pi}d\phi_s\cos(j\phi_s)\int_{-\pi}^{\pi}\left\{\frac{a_{s0}}{2}\frac{\partial W}{\partial r_s}+\sum_{n=1}^{\infty}\cos(n\psi_s)a_{sn}\left[\frac{\partial W}{\partial r_s}-K'nW\right]\right.$$
$$\left.-\frac{1}{4}\frac{d\theta_{sb}}{dz}K'W\right\}|_{r_s=1,\rho_s=1}d\psi_s\ ,\qquad j=0,1,2,.....\infty \qquad (2.30)$$

Eq.2.30 is a linear system of algebraic equations for the unknown coefficients a_{sj}. When this system is truncated at j=M, we obtain M+1 linear equations for the M+1 coefficients $a_{s0}.....a_{sM}$. When the values of these coefficients are substituted back into (2.28), we have a full description of the tissue temperature field at any location (x,y). The accuracy of the solution depends on the order of the truncation, but in principle the solution becomes exact as $M\to\infty$.

Although this approach can be used to treat two or more vessels and provides exact results for any value of K', the numerical evaluation of the integral in (2.30) is very time-

consuming, and not convenient for engineering purposes. Therefore, in this chapter we shall use (2.30) only to evaluate the accuracy of the approximate solution in section 2.3.1 when $K' \neq 1$ and use the latter solution to construct the solution for countercurrent vessel pairs.

2.3.3 Accuracy of the Approximate Solution for Single Periodically Spaced Vessel

In Figures 4 and 5 we compare the predictions of the approximate and exact solutions for the shape factor σ_s when $K' \neq 1$ for two extreme cases, $K'=10$ and $K'=0.1$, for a single periodically spaced vessel, as shown in Figure 2. The tissue thickness H is four times the vessel diameter and the spacing, $2D=20$, is sufficiently large for vessel-vessel interaction to be small. Figure 4 shows that the accuracy of the approximate solution is better than 0.5 percent for $0.1<Bi<10$ and $0.1<K'<10$. Figure 5 shows that the error associated with the eccentricity, $Sa=(H_2-H_1)/2$, is somewhat larger than that associated with the Biot number Bi. As the eccentricity is increased, the error in the approximate solution increases monotonically reaching a maximum of 3 percent for $K'=10$, and 0.5 percent for $K'=0.1$, at $Sa=2.8$. For this value of Sa the top of the vessel is within 0.2 diameters of the upper surface of the tissue.

2.3.4 Single Vessel Shape Factor

The shape factor for the single periodically spaced vessel is examined for a wide range of the governing parameters, vessel periodicity $2D$, eccentricity Sa and Biot number Bi in Figures 6, 7 and 8. The effect of vessel periodicity $2D$ is shown in Figure 6 for four different tissue thicknesses, $H=2.2$, 4, 8, 16, and for Bi=0.1, 1 and 10 when $H_1=H_2$ and $K'=1$. One

observes that the shape factor approaches a constant when $2D/H > 2$ for a wide range of Biot numbers. This indicates that when $D>H$ the interaction between vessels is small and the use of the adiabatic boundary condition (2.7) for the two-vessel geometry in Figure 3 will be reasonable, although this boundary condition is not strictly satisfied. For most two-dimensional tissue preparations, $2D>>H$, and H lies between 4 and 8 in the first and second vessel generations. Figure 7 shows how the shape factor varies as a function Bi for various K' with H=8 and $2D$=20. Note that the shape factor σ_s is nearly independent of Bi for Bi>2. The dependence of the shape factor on the eccentricity Sa is shown in Figure 8 for H=8, $2D$=20 and Bi=1. Note that σ_s is a weak function of Sa, but its sensitivity to Sa increases for K'>>1.

2.4 Countercurrent Artery-Vein Pairs

2.4.1 Two Vessel Solution

The theory and experiments in [12, 25, 29, 36, 37] suggest that in the microcirculation countercurrent artery-vein pairs are now regarded as the primary blood-tissue heat transfer unit. We would, therefore, like to extend the solution approach in section 2.3.1 to two vessels undergoing countercurrent heat exchange. In nearly all two-dimensional tissue preparations the average spacing of vessel pairs $2D$ is much larger than the tissue thickness H and, thus, the interaction between vessel pairs can be neglected. The cross sectional geometry and the coordinate system are shown in Figure 3.

Following the procedure for the single vessel, we write the solution for a countercurrent artery-vein pair as

$$\theta_a = (\rho_a^2 - \frac{1}{4}\rho_a^4 - \frac{3}{4})\frac{1}{4}\frac{d\bar{\theta}_{ab}}{dz} + \frac{a_{a0}}{2} + \sum_{j=1}^{\infty} a_{aj}\rho_a^j \cos(j\phi_a) + b_{aj}\rho_a^j \sin(j\phi_a) \qquad (2.31)$$

$$\theta_v = (\rho_v^2 - \frac{1}{4}\frac{\rho_v^4}{\rho_{vr}^2} - \frac{3}{4}\rho_{vr}^2)\frac{\bar{u}}{4}\frac{d\bar{\theta}_{vb}}{dz} + \frac{a_{v0}}{2} + \sum_{j=1}^{\infty} a_{vj}\rho_v^j \cos(j\phi_v) + b_{vj}\rho_v^j \sin(j\phi_v) \qquad (2.32)$$

where, due to the eccentricity of the vessel location, terms involving sin(jϕ) in both (2.31) and (2.32) cannot be omitted as in Eq.2.10 for a single vessel.

Using the same technique as in section 2.3.1, we position two sources of strength C_{ss} and C_{sv} at the centers of the artery and vein, respectively. The tissue temperature is then a linear combination of Green's functions representing these sources and is expressed by

$$\theta_t = C_{ss}W(x,y:\xi_a,\eta_a) + C_{sv}W(x,y:\xi_v,\eta_v) \qquad (2.33)$$

where W(x,y:ξ,η) is the more general fundamental solution (A.11) in Appendix 1 and is given by

$$W = (C_1 y + C_2) + \sum_{n=1}^{\infty} \frac{1}{D}\cos[\sqrt{\lambda_n}(\xi - D)]\cos[\sqrt{\lambda_n}(x - D)][A_1 e^{\sqrt{\lambda_n}y} + B_1 e^{-\sqrt{\lambda_n}y}] \qquad y \geq \eta \quad (2.33a)$$

$$W = (D_1 y + D_2) + \sum_{n=1}^{\infty} \frac{1}{D}\cos(\sqrt{\lambda_n}(\xi - D)]\cos(\sqrt{\lambda_n}(x - D)][A_2 e^{\sqrt{\lambda_n}y} + B_2 e^{-\sqrt{\lambda_n}y}] \qquad y < \eta \quad (2.33b)$$

The coefficients a_{aj}, b_{aj}, a_{vj}, b_{vj}, C_{ss} and C_{sv} are evaluated in the same manner as for the single vessel in (2.16) and (2.18). We only list the final expressions.

$$C_{ss} = \frac{K'\pi}{2}\frac{d\bar{\theta}_{ab}}{dz} \qquad (2.34a)$$

$$C_{sv} = \frac{K'\pi\rho_{vr}^2\bar{u}}{2}\frac{d\bar{\theta}_{vb}}{dz} \qquad (2.34b)$$

$$a_{s0} = \int_{-\pi}^{\pi} \left[\frac{C_{ss}}{\pi} W(x,y:\xi_s,\eta_s) + \frac{C_{sv}}{\pi} W(x,y:\xi_v,\eta_v)\right]\Big|_{\rho_s=1} d\phi_s \tag{2.34c}$$

$$a_{sj} = \int_{-\pi}^{\pi} \left[\frac{C_{ss}}{\pi} W(x,y:\xi_s,\eta_s) + \frac{C_{sv}}{\pi} W(x,y:\xi_v,\eta_v)\right]\frac{\cos(j\phi_s)}{\rho_s'}\Big|_{\rho_s=1} d\phi_s \qquad j=1,2,\ldots\infty \tag{2.34d}$$

$$b_{sj} = \int_{-\pi}^{\pi} \left[\frac{C_{ss}}{\pi} W(x,y:\xi_s,\eta_s) + \frac{C_{sv}}{\pi} W(x,y:\xi_v,\eta_v)\right]\frac{\sin(j\phi_s)}{\rho_s'}\Big|_{\rho_s=1} d\phi_s \qquad j=1,2,\ldots\infty \tag{2.34e}$$

$$a_{v0} = \int_{-\pi}^{\pi} \left[\frac{C_{ss}}{\pi} W(x,y:\xi_s,\eta_s) + \frac{C_{sv}}{\pi} W(x,y:\xi_v,\eta_v)\right]\Big|_{\rho_v=\rho_v^-} d\phi_v \tag{2.34f}$$

$$a_{vj} = \int_{-\pi}^{\pi} \left[\frac{C_{ss}}{\pi} W(x,y:\xi_s,\eta_s) + \frac{C_{sv}}{\pi} W(x,y:\xi_v,\eta_v)\right]\frac{\cos(j\phi_v)}{\rho_v'}\Big|_{\rho_v=\rho_v^-} d\phi_v \qquad j=1,2,\ldots\infty \tag{2.34g}$$

$$b_{vj} = \int_{-\pi}^{\pi} \left[\frac{C_{ss}}{\pi} W(x,y:\xi_s,\eta_s) + \frac{C_{sv}}{\pi} W(x,y:\xi_v,\eta_v)\right]\frac{\sin(j\phi_v)}{\rho_v'}\Big|_{\rho_v=\rho_v^-} d\phi_v \qquad j=1,2,\ldots\infty \tag{2.34h}$$

As in the single vessel case, the foregoing solution is exact when K' is unity and an accurate approximation when K'≠1.

To complete the analysis, the bulk temperatures θ_{sb} and θ_{vb} satisfy the coupled equations

$$\theta_{sb} = -\frac{11}{96}\frac{d\theta_{sb}}{dz} + \frac{a_{s0}}{2} \tag{2.35a}$$

$$\theta_{vb} = -\frac{11}{96}\varepsilon\rho_w^2\frac{d\theta_{vb}}{dz} + \frac{a_{v0}}{2} \tag{2.35b}$$

where a_{s0} and a_{v0} from 2.34(a,b,c,f) are linear combinations of $d\theta_{sb}/dz$ and $d\theta_{vb}/dz$. The a solution of (2.35a) and (2.35b) requires the specification of two boundary conditions in the axial direction. For countercurrent flow, these boundary conditions are the prescribed bulk temperatures at the inlets of the vessels. Once the bulk temperatures are determined, (2.31), (2.32) and (2.33) provide the solution for the temperature field in the vessels and the tissue.

2.4.2 Application to Rat Cremaster Muscle

A representative solution for countercurrent flow in a first generation artery-vein pair in rat cremaster muscle is shown in Figure 9. For this calculation we have chosen $2D/H$=32 to insure that the adiabatic boundary condition at $x=\pm D$ be accurately satisfied. A typical vessel tissue geometry for the rat cremaster muscle is: artery diameter, 120μm, vein diameter, 200μm, and tissue thickness, 300μm. The ratio of artery to vein velocity is determined by requiring that the mass flow in each vessel be the same. Both air and water environments are examined. For air, k_{air}=0.02622 W/m°C, h_{air}=13.34 W/m^2°C and Bi_{air} = 0.00134. For water, k_{water}=0.5967 W/m°C, h_{water}=235.525 W/m^2°C and Bi_{water} = 0.0237. The inlet boundary conditions are θ_{ab}=1 at z=0 and θ_{vb}=0 at z=20. This calculation was used to guide the design of our rat cremaster muscle experiments. The feasibility of this experiment rested on our ability to detect measurable temperature disturbances at significant distances from the entrance of the artery in the cremaster tissue preparation and on the ability to measure the local difference in temperature between vessels in the artery-vein pair. This feasibility was demonstrated by the solution shown in Figure 9, which shows the temperature decay along the artery-vein axes. The solution predicts that measurable thermal disturbances in a water bath preparation are confined to a dimensionless distance z=4, or a physical distance z^* that is $4Pe\rho_{ar}^*$. Significant artery-vein temperature differences can likewise be detected over this distance. For a 120μm diameter artery with Pe=5 this decay length is only 1 mm. Although this distance can be increased or decreased by pharmacologically induced changes in downstream resistance and consequently blood flow in the cremaster muscle that either increase or decrease $Pe\rho_{ar}^*$, this distance is too short to be observed by high resolution

infrared thermography. However, the model predicts in Figure 9 that if the water is drained from the bath and briefly exposed to the air the thermal equilibration length is about four times larger. The latter experimental design has been employed in chapter 3 to obtain the first experimental measurements of axial countercurrent thermal equilibration length in a microvascular tissue preparation. Obviously, in smaller vessels downstream there is almost no temperature difference across the tissue layer, since the blood has already reached equilibrium with the surrounding tissue in the larger vessels upstream. These calculations suggest that thermal equilibration occurs primarily in the 1A and 2A vessels of the rat cremaster muscle except at very high non-physiological flow rates.

Chapter 3. Microvascular Thermal Equilibration in Rat Cremaster Muscle

A new experimental approach is described in this chapeter which was developed to obtain the first direct measurements of the axial countercurrent thermal equilibration in a microvascular tissue preparation using high-resolution infrared thermography. Detailed surface temperature measurements were obtained for an exteriorized rat cremaster muscle in which vasoactive pharmacological agents were employed to change the local blood flow Peclet number from 1 to 14 in the feeding arteriole. Under normal conditions, only the 1A arterioles (> 70 μm dia.) showed thermal nonequilibration with the surrounding tissue. The theoretical model developed in chapter 2 for a two-dimensional tissue preparation with arbitrarily embedded countercurrent vessels was modified to include axial conduction in the tissue and the presence of the supporting glass slide. This modified model was employed to interpret the experimental results and to relate the surface temperature profiles to the bulk temperature profiles in the countercurrent artery and vein and the local average tissue temperature in the cross-sectional plane. Surface temperature profiles transverse to the vessel axis was found to depend significantly on the tissue inlet temperature. The eigenfunction for the axial thermal equilibration depends primarily on the blood flow Peclet number and the environmental convective coefficient. The theory also predicts the range of vessel size and Pe where the primary mechanism of tissue heat transfer changes from nearly pure conduction to a greatly enhanced effective conductivity due to countercurrent convective energy exchange. When $\rho_w^* Pe$ is less than 1 mm (the range in our experiments), axial conduction is the dominant mode of axial thermal equilibration. For $1 < \rho_w^* Pe < 3$ mm,

countercurrent blood flow becomes comparable to axial conduction, whereas, when $\rho_w^* Pe > 3$ mm, countercurrent blood flow is the dominant mode of axial thermal equilibration. Thus, for $\rho_w^* Pe > 3$ mm the axial equilibration length is proportional to the blood flow Peclet number as previously predicted in chapter 2 where axial conduction was neglected. It is also shown that the axial decay of the tissue temperature at low perfusion rates can be described by a simple one-dimensional Weinbaum-Jiji equation with a newly derived conduction shape factor.

3.1 Introduction

It is well known that the blood flow distribution and detailed microvascular geometry have a profound effect on the heat exchange between the blood and tissue and the heat exchange of the tissue near the surface of the body with the environment. Most investigations of countercurrent heat exchange in humans and mammals prior to 1980 examined the heat transfer between the large countercurrent arteries and veins in the limbs [8, 27, 29, 31]. No equivalent experiments have been successfully performed in microvascular tissue preparations. These experiments require high spatial resolution temperature measurements on a length scale of the diameter of the microvessels. This study, to the best of our knowledge, presents the first measurements of countercurrent axial thermal equilibration in the microcirculation.

Since 1980, several *in vivo* and *in vitro* experiments have been performed to elucidate how and where vascular heat transfer occurs. In Weinbaum *et al.* [37] thermocouple traverses across a rabbit thigh were performed *in vivo* and the arterial temperature was found

to be nearly equal to the venous temperature for any countercurrent pair encountered along the traverse. Subsequently, the experiments performed by Lemons *et al.* [25], in which the thermal disturbances in the vicinity of vessels from 50 to 500 μm diameter were measured by thermocouples, showed that the microvascular artery-vein temperature differences in these primary heat exchange vessels were only of the order of 0.1 to 0.2 °C for vessels 100 μm dia. or larger, whereas for vessels less than 100 μm dia. there were no measurable temperature disturbances. Crezee *et al.* [15] inserted a small plastic tube into the tissue of a bovine kidney and measured the disturbance temperature field in a plane perpendicular to the tube when heated water was circulated through it, and the kidney cortex perfused at different rates. These investigators also used thermocouples to map the temperature distribution in the tissue of isolated perfused bovine tongues at various perfusion rates [14]. Roemer *et al.* [30] measured steady state temperature profiles in canine thighs heated by scanned focused ultrasound. These experiments were performed either *in vitro* with saline perfused blood vessels or *in vivo* without blood perfusion control. In [25] the investigators showed the range of vessels responsible for heat transfer under resting conditions, but did not directly visualize the vessels and measure the blood flow. Moreover, there has been no prior experimental study that has measured the axial thermal equilibration length for different sized microvessels in an *in vivo* tissue preparation and has related this equilibration to the local blood perfusion.

High-resolution infrared thermography is a noninvasive technique for measuring the detailed *in vivo* surface temperature field above individual microvessels in a two-dimension tissue preparation such as the rat cremaster muscle preparation shown in Figure 1. It is well

known that the equilibration length for a particular vessel pair varies with the blood flow Peclet number and hence this length varies as the diameter and the flow velocity change during physiological regulation. Changes in caliber and flow rate of the feeding arteriole can be induced by pharmacological vasoactive agents. It is, therefore, possible to experimentally examine the relationship between the thermal equilibration length and the blood flow Peclet number in the feeding arteriole by introducing vasoactive drugs. In this study, we used the rat cremaster muscle as the tissue preparation to study for the first time the axial thermal equilibration between blood and tissue *in vivo*.

In chapter 2, a simplified model for a two-dimensional tissue preparation shown in Figure 3 was presented. The artery-vein pair is represented by two line sources that are arbitrarily positioned in the cross sectional plane of the preparation. An analytic solution was then derived for a Green's function which satisfied all the tissue boundary conditions for this flow geometry in the cross-sectional plane of the vessels. This solution was shown to be exact when the ratio of blood to tissue conductivity $K'=1$ and highly accurate when $K' \neq 1$. This initial model was used to design and test the feasibility of the present experiment. For the experiment to work one must be able to detect measurable temperature disturbances at significant distances from the entrance of the feeding arteriole in the rat cremaster muscle preparation. However, this initial model did not take into account the axial heat conduction in the tissue region as well as the effect of the glass plate, on which the rat cremaster muscle preparation was placed during the experiments. We found that at low blood flow rates, axial heat conduction is comparable to the axial heat transfer due to countercurrent flow in the blood vessels. A more realistic model, schematically shown in Figure 10, was, therefore,

developed in this study for more detailed comparison with experiments. This modified three-dimensional model considers both axial conduction and the effect of the supporting glass. Following the analysis in chapter 2, a simplified Green's function or fundamental solution for a line source arbitrarily positioned in the tissue region is first developed. We then construct the solution for countercurrent flow by superposing two fundamental solutions. Using this approach, the boundary value problem for the axial interactions between vessels is reduced to a coupled system of ordinary differential equations for the axial bulk temperature variation in each vessel and the axial variation of the average tissue temperature.

3.2 Experimental Methods

3.2.1 Methods

Fourteen male Sprague-Dawley rats (Mean±SD, 153±27g) were used in this study. The animals were anesthetized with an intraperitoneal injection of sodium pentobarbital solution (40mg/kg). Supplemental doses were administered as needed. A tracheal tube was inserted to maintain a patent airway. After anesthesia administration, the rat was placed on a water-jacketed pad to maintain rectal temperature, which was monitored throughout the experiment with a thermocouple inserted into the rectum. The surgical procedure required about half an hour and the subsequent experimental procedure required about one hour.

The left cremaster muscle was dissected free from the scrotal skin and testicle for *in vivo* microvascular observation as described previously [3, 18]. This exteriorized cremaster muscle was extended into a flattened sheet and held with silk sutures over an optical window

in a tissue bath at room temperature. The schematic diagram for the experimental setup is shown in Figure 11. The tissue bathing solution was drawn from stock reservoir 1 containing a modified Krebs solution that consisted of (in g/liter) 6.6 NaCl, 0.35 KCl, 0.28 $MgSO_4$, 0.28 $CaCl_2 \cdot 2H_2O$, 0.16 KH_2PO_4, 2.09 dextrose and 2.14 $NaHCO_3$ dissolved in filtrated water. The muscle is sensitive to PO_2, PCO_2 and pH, which were all monitored by an Anafaze 8LS controller which adjusted the bubbling rate of CO_2 and N_2 in recirculating reservoir 2 to maintain a PO_2 of 15-30 torr, a PCO_2 of 35-45 torr and a pH of 7.4.

The preparation was transilluminated on the microscope stage (Zeiss, ACM) and viewed through a 10X Nikon water immersion objective. During the experiment the field of view was displayed on a closed-circuit camera and videotaped for later analysis. The average blood flow velocity u in the feeding arteriole is equal to the centerline blood velocity V divided by 1.6 [6]. The blood flow Peclet number Pe is given by

$$Pe = 2\gamma_f C_f \rho_m^* u / k_f$$

where γ_f is blood density, C_f is specific heat of blood, k_f is blood thermal conductivity, u is average blood flow velocity of the microvessel and ρ_m^* is vessel radius (μm). Centerline red cell velocity was measured with an optical Doppler velocimeter (Microcirculation Research) and vessel radius was measured from the video tape with an electronic video caliper (Microcirculation Research). The preparation could be positioned either under the light microscope optics or rotated into place under a Hughes Probeye infrared camera for obtaining a high resolution thermal image of the muscle. The infrared camera was 10 cm to the left of the optical axis so movement between the two measurement systems could occur rapidly and a registration mark insured reproducibly accurate placement of the muscle

under the optical axis. The IR camera had an auxiliary 5 mil lens which yields an optical resolution of 125 μm and 0.1 ^{0}C temperature resolution. One calibrated copper-constantan thermocouple was used to measure the environmental temperature and two other thermocouples were held in position beneath the muscle at separate locations to provide an absolute temperature reference for the thermal imaging camera. The experiment was controlled by and the data were acquired and recorded with LabView® software running on a Macintosh computer.

3.2.2 Measurement protocol

Initially, a thirty minute stabilization period followed surgery to allow the preparation to achieve an initial steady state blood flow. There were then four trials in each experiment, one for each of four different microvascular blood flow rates. To induce changes in the blood flow Peclet numbers in a feeding arteriole, a vasoconstrictor, NE (10^{-5} M), or a vasodilator, Na nitroprusside (10^{-7} M, 10^{-6} M and 10^{-5} M), was added for each trial. There was a 10 minute period for the preparation to reach equilibrium after each was added. After all the parameters (temperature, velocity and diameter) were stable, the image of the feeding arteriole-venule pair and the centerline red blood cell velocity were recorded continuously for a two-minute measurement period. Then within 30 seconds the preparation was rotated under the IR camera and the solution inside the tissue bath was drained. The thermal image of the preparation as well as the temperatures measured by thermocouples were recorded. A thin plastic wrap was laid on the muscle surface to prevent evaporation. Immediately after the thermal image was completed, the rat was repositioned under the

optical microscope and the velocity and diameter were again measured to verify that they had remained unchanged while the thermal image was obtained. Next a new concentration of drug was added to obtain a stepwise changes in blood flow to reach a new equilibrium and the procedure described above would be repeated until the trial of Na nitroprusside (10^{-5} M) was finished.

3.2.3 Experimental results

Figure 12 shows a sequence of high resolution infrared images of the same rat cremaster muscle at four different blood flow rates. Figure 13 shows the axial surface temperature profiles above the central arteriole of the cremaster muscle at four different blood flow rates. Increasing the blood flow rate produced a higher inlet temperature at the proximal boundary, which is on the left, at $z^*=0$ mm, and an elevation of the temperature of the entire preparation. The maximum point in the temperature profiles normal to the vessel axial direction was found to be a good indication of the location of the feeding arteriole. As observed in Figure 12 the thermal disturbance due to the blood vessels became more evident as the blood flow rate increased.

The horizontal surface temperature profiles normal to the axial direction of the 1A feeding artery-vein pair will be discussed later. These profiles revealed somewhat surprisingly that this temperature field was almost uniform in the lateral direction. The comparison between experimental data and theoretical predictions presented in section 3D will be used to explain this unexpected observation and interpret the results in Figures 12, 13, 18 and 19.

3.3 Modified 3-D Model for Heat Transfer in 2-D Tissue Preparation Considering Axial Conduction and the Supporting Glass Plate.

3.3.1 Formulation

In this part of study, we will develop a three-dimensional mathematical model to describe the boundary value problem shown in Figure 10. We consider two vessels embedded in a thin tissue layer of thickness $H^*=H_1^*+H_2'^*$. The tissue is supported by a thin glass plate of thickness H_g^*.

The principal simplifying assumptions of the model are the following: (1) Both the flow and temperature fields are steady and the velocity profiles in the blood vessels are parabolic; (2) The glass plate in the cross-sectional plane can be converted into an equivalent tissue layer of thickness $H_g k_t/k_g$ so that the boundary value problem can be simplified into an equivalent tissue layer of thickness $H^*=H_1^*+H_2^*=H_1^*+(H_2'^*+H_g^* k_t/k_g)$; (3) To accurately describe the axial conduction for the new cross-sectional plane, the conductivity in the axial direction can be converted into an equivalent value k_m, if one assumes equal axial temperature gradients in the glass and the tissue regions. k_m is defined in the following expression:

$$k_m(H_1^*+H_2'^*+H_g^*\frac{k_t}{k_g})=k_t(H_1^*+H_2'^*)+k_g H_g^*,\ or\ \frac{k_m}{k_t}=\frac{H_1^*+H_2'^*+H_g^* k_g/k_t}{H_1^*+H_2'^*+H_g^* k_t/k_g}$$

(4) In order to simplify the complexity caused by axial conduction, the axial conduction term in the tissue energy equation, $\partial^2\theta_t/\partial z^2$, is approximated by its average value $d^2\theta_{t,ave}/dz^2$, defined in Eq.3.10, while the axial conduction in the blood vessels is neglected because their cross-sectional area is small compared to that of the tissue; (4) The temperature gradient

$\partial\theta_{a,v}/\partial z$ in the convective term of the vessel energy equations can be approximated by the axial gradient of the vessel bulk temperatures, $d\theta_{ab,\,vb}/dz$ as previously justified [42]; (5) The cross-sectional plane is uniform in the axial direction and perfusion bleed-off from the supply artery-vein pair is neglected. The basic geometry, symbols and coordinate system are sketched in Figures 2 and 10.

Non-dimensional parameters are introduced as follows:

$$\rho_a=\frac{\rho_a^*}{\rho_{at}^*},\ \rho_v=\frac{\rho_v^*}{\rho_{at}^*},\ \rho_{vt}=\frac{\rho_{vt}^*}{\rho_{at}^*},\ x=\frac{x^*}{\rho_{at}^*},\ y=\frac{y^*}{\rho_{at}^*},\ z=\frac{z^*}{\rho_{at}^*(k_w/k_t)^{0.5}},\ H_{1,2}=\frac{H_{1,2}^*}{\rho_{at}^*},\ D=\frac{D^*}{\rho_{at}^*},$$

$$l=\frac{l^*}{\rho_{at}^*},L=\frac{L^*}{\rho_{at}^*},Pe=\frac{2\gamma_f C_f\rho_{at}^* u_a}{k_f},\ Bi_{1,2}=\frac{h_{1,2}\rho_{at}^*}{k_t},\ \theta_{a,v,t}=\frac{T_{a,v,t}-T_\infty}{T_{a0}-T_\infty},\ \bar{u}=\frac{u_v}{u_a}$$

here the subscripts *a*, *v* refer to artery and vein, asterisks denote dimensional variables, and ρ_{at}^* and ρ_{vt}^* are the dimensional radii of the artery and vein. Note that *z* is scaled by $\rho_{at}^*(k_w/k_t)^{0.5}$ rather by $Pe\rho_{vt}^*$, as done in chapter 2, and the anisotropy governing equation becomes a Laplace equation without the k coefficients. Introducing the above assumptions, one obtains the following simplified dimensionless governing equations for the vessels and the tissue

$$\frac{1}{\rho_a}\frac{\partial}{\partial\rho_a}\left(\rho_a\frac{\partial\theta_a}{\partial\rho_a}\right)+\frac{1}{\rho_a^2}\frac{\partial^2\theta_a}{\partial\phi_a^2}=Pe\left(1-\rho_a^2\right)\frac{d\theta_{ab}}{dz}\ ,\qquad \rho_a\le 1 \tag{3.1}$$

$$\frac{1}{\rho_v}\frac{\partial}{\partial\rho_v}\left(\rho_v\frac{\partial\theta_v}{\partial\rho_v}\right)+\frac{1}{\rho_v^2}\frac{\partial^2\theta_v}{\partial\phi_v^2}=Pe\,\bar{u}\left(1-\frac{\rho_v^2}{\rho_{vt}^2}\right)\frac{d\theta_{vb}}{dz}\ ,\qquad \rho_v\le\rho_{vt} \tag{3.2}$$

$$\frac{\partial^2\theta_t}{\partial x^2}+\frac{\partial^2\theta_t}{\partial y^2}=-\frac{d^2\theta_{tave}}{dz^2}\ ,\quad \rho_a>1,\ \rho_v>\rho_{vt},\ -D\le x\le D,\ -H_2\le y\le H_1 \tag{3.3}$$

$$\theta_a = \theta_t , \qquad \rho_a = 1 \tag{3.4a}$$

$$K' \frac{\partial \theta_a}{\partial \rho_a} = \frac{\partial \theta_t}{\partial \rho_a} , \qquad \rho_a = 1 \tag{3.4b}$$

$$\theta_v = \theta_t , \qquad \rho_v = \rho_w \tag{3.5a}$$

$$K' \frac{\partial \theta_v}{\partial \rho_v} = \frac{\partial \theta_t}{\partial \rho_v} , \qquad \rho_v = \rho_w \tag{3.5b}$$

$$\frac{\partial \theta_t}{\partial y} = -Bi_1 \theta_t , \qquad y = H_1 \tag{3.6a}$$

$$\frac{\partial \theta_t}{\partial y} = Bi_2 \theta_t , \qquad y = -H_2 \tag{3.6b}$$

For a preparation, whose width $2D$ is much larger than the tissue thickness H, it is reasonable to assume that there is no heat flow across the boundaries $x = \pm D$. Thus, we shall require the adiabatic condition:

$$\frac{\partial \theta_t}{\partial x} = 0 \qquad x = \pm D \tag{3.7}$$

In Eqs.3.1 and 3.2, θ_{ab}, θ_{vb} and $\theta_{t\,ave}$ are the artery bulk temperature, vein bulk temperature and the average tissue temperature, respectively. These temperatures are defined as

$$\theta_{ab} = \frac{2}{\pi} \int_{-\pi}^{\pi} \int_0^1 \theta_a (1 - \rho_a^2) \rho_a \, d\rho_a \, d\phi_a \tag{3.8}$$

$$\theta_{vb} = \frac{2}{\pi \rho_w^2} \int_{-\pi}^{\pi} \int_0^{\rho_w} \theta_v \left(1 - \frac{\rho_v^2}{\rho_w^2}\right) \rho_v \, d\rho_v \, d\phi_v \tag{3.9}$$

$$\theta_{t\,ave} = \frac{1}{2D(H_1 + H_2) - \pi - \pi \rho_w^2} \iint_{\text{tissue region}} \theta_t(x, y, z) \, dx \, dy \tag{3.10}$$

The fundamental difference between the foregoing formulation and that in chapter 2 is that axial conduction is treated in the tissue (right-hand side of Eq.3.3) and the effective thickness of the tissue in the lower region has been increased to include the glass plate. As we shall see, this substantially changes the boundary value problem in the z direction without significantly changing the boundary value problem in the cross-sectional plane.

3.3.2 Solution for countercurrent flow

A theoretical solution to the complicated boundary value problem summarized in the last section can be obtained by modifying the solution procedure outlined in chapter 2. The simplifications introduced in the governing Eqs.3.1, 3.2 and 3.3 and the boundary conditions enable us to separate variables and solve the boundary value problem in the cross-sectional plane independent of the boundary value problem in the z direction. We first need to develop a Green's function or fundamental solution for a line source arbitrarily positioned within the tissue-vessel region. We then construct the solution for two countercurrent vessels undergoing countercurrent heat exchange by superposing the fundamental solutions. Finally, we solve the boundary value problem for the axial interaction to determine the vessel bulk temperatures and the average tissue temperature.

The fundamental solution or Green's function $W(x,y:\xi,\eta)$ satisfies Laplace's equation in the rectangular region, $-D<x<D$ and $-H_2<y<H_1$, except for the source point (ξ,η) arbitrarily located inside the region. It also satisfies boundary conditions (3.6) and (3.7). The boundary value problem for this singular solution is

$$\begin{cases} \dfrac{\partial^2 W}{\partial x^2}+\dfrac{\partial^2 W}{\partial y^2}=\delta(x-\xi)\delta(y-\eta) \\ \dfrac{\partial W}{\partial x}=0 \qquad\qquad at\ x=\pm D \\ \dfrac{\partial W}{\partial y}=\mp Bi_{1,2}W \qquad at\ y=\pm H_{1,2} \end{cases} \tag{3.11}$$

The solution for W is derived in Appendix 1 and is given by

$$W=(C_1y+C_2)+\sum_{n=1}^{\infty}\frac{1}{D}\cos[\sqrt{\lambda_n}(\xi-D)]\cos[\sqrt{\lambda_n}(x-D)][A_1e^{\sqrt{\lambda_n}y}+B_1e^{-\sqrt{\lambda_n}y}] \qquad y\geq\eta$$

$$W=(D_1y+D_2)+\sum_{n=1}^{\infty}\frac{1}{D}\cos[\sqrt{\lambda_n}(\xi-D)]\cos[\sqrt{\lambda_n}(x-D)][A_2e^{\sqrt{\lambda_n}y}+B_2e^{-\sqrt{\lambda_n}y}] \qquad y\leq\eta$$

where the A_i, B_i, C_i, D_i, i=1,2 are constants, which depend on the Biot number and the tissue geometry, and are listed in (A.8) and (A.10) of Appendix 1 and the eigenvalues $\lambda_n=(n\pi/2D)^2$.

The solution for a countercurrent artery-vein pair is decomposed into a particular solution and a general solution as previously derived in chapter 2. These expressions are

$$\theta_a=(\rho_a^2-\frac{1}{4}\rho_a^4-\frac{3}{4})\frac{Pe}{4}\frac{d\theta_{ab}}{dz}+\frac{a_{a0}}{2}+\sum_{j=1}^{\infty}a_{aj}\rho_a^j\cos(j\phi_a)+b_{aj}\rho_a^j\sin(j\phi_a) \tag{3.12}$$

$$\theta_v=(\rho_v^2-\frac{1}{4}\frac{\rho_v^4}{\rho_w^2}-\frac{3}{4}\rho_w^2)\frac{Pe\bar{u}}{4}\frac{d\theta_{vb}}{dz}+\frac{a_{v0}}{2}+\sum_{j=1}^{\infty}a_{vj}\rho_v^j\cos(j\phi_v)+b_{vj}\rho_v^j\sin(j\phi_v) \tag{3.13}$$

Similarly, the tissue temperature can also be decomposed into a particular solution and a general solution, $\theta_t=\theta_{pt}+\theta_{ht}$. θ_{pt} is given by

$$\theta_{pt}=-\frac{d^2\theta_{tmw}(z)}{dz^2}(\frac{y^2}{2}+I_1y+I_2) \tag{3.14}$$

where,

$$I_1 = \frac{Bi_1 Bi_2 (H_1^2 - H_2^2) + 2(H_1 Bi_2 - H_2 Bi_1)}{2[-Bi_1 Bi_2 (H_1 + H_2) - (Bi_1 + Bi_2)]}$$

$$I_2 = \frac{(2 + H_1 H_2 Bi_1 Bi_2)(H_1 + H_2) + Bi_1 H_1^2 + Bi_2 H_2^2 + 2 H_1 H_2 (Bi_1 + Bi_2)}{2[-Bi_1 Bi_2 (H_1 + H_2) - (Bi_1 + Bi_2)]}$$

This particular solution does not appear in chapter 2. since the right side of Eq.3.3 is homogeneous. θ_{bt} satisfies Laplace's equation in the tissue region and boundary conditions (3.6) and (3.7). The general solution for the tissue can be constructed by placing two anisotropic line sources at the center of the artery and vein with strength C_{at} and C_{vt}, respectively. Therefore, θ_{bt} is a linear combination of Green's functions representing these sources. The tissue temperature is expressed by

$$\theta_t = C_{at} W(x,y:\xi_a,\eta_a) + C_{vt} W(x,y:\xi_v,\eta_v) + \theta_{pt}(y,z) \tag{3.15}$$

where (ξ_a, η_a) and (ξ_v, η_v) are the coordinates of the artery and the vein, respectively. One notes that the tissue temperature also satisfies the governing Eq.3.3 and the outer boundary conditions (3.6) and (3.7).

As shown in section 2.4.1, the coefficients a_{aj}, b_{aj}, a_{vj}, b_{vj}, C_{at} and C_{vt} are determined by athe matching conditions (3.4) and (3.5) for the continuity of temperature and heat flux on the vessel surfaces. One obtains

$$C_{at} = \frac{K' \pi Pe}{2} \frac{d\theta_{ab}}{dz} + \pi \frac{d^2 \theta_{ab}}{dz^2} \tag{3.16a}$$

$$C_{vt} = \frac{K' \pi Pe \rho_w^2 \bar{\mu}}{2} \frac{d\theta_{vb}}{dz} + \rho_w^2 \pi \frac{d^2 \theta_{vb}}{dz^2} \tag{3.16b}$$

$$a_{a0} = \int_{-\pi}^{\pi} \left[\frac{C_{at}}{\pi} W(x,y:\xi_a,\eta_a) + \frac{C_{vt}}{\pi} W(x,y:\xi_v,\eta_v) + \frac{\theta_{pt}}{\pi} \right]_{\rho_a = 1} d\phi_a \tag{3.16c}$$

$$a_{ej}=\int_{-\pi}^{\pi}\left[\frac{C_{ee}}{\pi}W(x,y:\xi_e,\eta_e)+\frac{C_{ev}}{\pi}W(x,y:\xi_v,\eta_v)+\frac{\theta_{et}}{\pi}\right]\frac{\cos(j\phi_e)}{\rho_e^j}\Big|_{\rho_e=1}d\phi_e \quad j=1,2,\ldots\infty \quad (3.16d)$$

$$b_{ej}=\int_{-\pi}^{\pi}\left[\frac{C_{ee}}{\pi}W(x,y:\xi_e,\eta_e)+\frac{C_{ev}}{\pi}W(x,y:\xi_v,\eta_v)+\frac{\theta_{et}}{\pi}\right]\frac{\sin(j\phi_e)}{\rho_e^j}\Big|_{\rho_e=1}d\phi_e \quad j=1,2,\ldots\infty \quad (3.16e)$$

$$a_{v0}=\int_{-\pi}^{\pi}\left[\frac{C_{ee}}{\pi}W(x,y:\xi_e,\eta_e)+\frac{C_{ev}}{\pi}W(x,y:\xi_v,\eta_v)+\frac{\theta_{et}}{\pi}\right]\Big|_{\rho_v=\rho_w}d\phi_v \quad (3.16f)$$

$$a_{vj}=\int_{-\pi}^{\pi}\left[\frac{C_{ee}}{\pi}W(x,y:\xi_e,\eta_e)+\frac{C_{ev}}{\pi}W(x,y:\xi_v,\eta_v)+\frac{\theta_{et}}{\pi}\right]\frac{\cos(j\phi_v)}{\rho_v^j}\Big|_{\rho_v=\rho_w}d\phi_v,\ j=1,2,\ldots\infty \quad (3.16g)$$

$$b_{vj}=\int_{-\pi}^{\pi}\left[\frac{C_{ee}}{\pi}W(x,y:\xi_e,\eta_e)+\frac{C_{ev}}{\pi}W(x,y:\xi_v,\eta_v)+\frac{\theta_{et}}{\pi}\right]\frac{\sin(j\phi_v)}{\rho_v^j}\Big|_{\rho_v=\rho_w}d\phi_v,\ j=1,2,\ldots\infty \quad (3.16h)$$

The $d^2\theta_e/dz^2$ terms in Eqs.3.16a,b do not appear in section 2.4.1, since axial conduction is neglected. The above expressions for a_{ej}, b_{ej}, a_{vj}, b_{vj}, $j>0$ are derived by applying the temperature continuity on the vessel surfaces. They can also be determined by the matching conditions (3.4b) and (3.5b) for the continuity of heat flux on the vessel surfaces. This leads to a second expression for the a_{ej}

$$a_{ej}=\int_{-\pi}^{\pi}\left[\frac{C_{ee}}{\pi}\frac{\partial W(x,y:\xi_e,\eta_e)}{\partial\rho_e}+\frac{C_{ev}}{\pi}\frac{\partial W(x,y:\xi_v,\eta_v)}{\partial\rho_e}+\frac{1}{\pi}\frac{\partial\theta_{et}}{\partial\rho_e}\right]\frac{\cos(j\phi_e)}{K'j\rho_e^{j-1}}\Big|_{\rho_e=1}d\phi_e,\ j=1,2,\ldots\infty \quad (3.17)$$

Following a derivation similar to that in Appendix 2, one can show that the a_{ej} calculated from Eq.3.16d and Eq.3.17 are identical when K', the ratio thermal conductivity of blood to tissue, is unity. One can draw the same conclusion for b_{ej}, a_{vj}, and b_{vj}. Thus, this solution is exact when $K'=1$, while when $K'\neq 1$, this solution is approximate, since it satisfies the heat flux continuity on the vessel surface globally rather than locally.

θ_{eb}, θ_{vb} and $\theta_{t,ew}$ still need to be determined. Substituting Eqs.3.12, 3.13 and 3.15 into the expressions for θ_{eb}, θ_{vb} and $\theta_{t,ew}$, respectively, we obtain

$$\theta_{ab} = -\frac{11Pe}{96}\frac{d\theta_{ab}}{dz} + \frac{a_{a0}}{2} \tag{3.18}$$

$$\theta_{vb} = -\frac{11Pe}{96}\pi\rho_w^2\frac{d\theta_{vb}}{dz} + \frac{a_{v0}}{2} \tag{3.19}$$

$$\theta_{tave} = \iint_{\text{tissue region}} \left\{ \left[\frac{C_{a0}W(x,y;\xi_a,\eta_a) + C_{v0}W(x,y;\xi_v,\eta_v)}{2D(H_1+H_2) - \pi - \pi\rho_w^2} \right] + \left[\frac{d^2\theta_{tave}}{dz^2} \frac{-Pe^2(y^2 + I_1 y + I_2)}{2D(H_1+H_2) - \pi - \pi\rho_w^2} \right] \right\} d\Omega \tag{3.20}$$

One notes that a_{a0}, a_{v0}, C_{a0} and C_{v0} are linear combinations of $d\theta_{ab}/dz$, $d\theta_{vb}/dz$ and $d^2\theta_{tb}/dz^2$. Substituting the expressions for a_{a0}, a_{v0}, C_{a0} and C_{v0} into Eqs.3.18, 3.19, and 3.20, one obtains

$$\theta_{ab} = A_{11}\frac{d\theta_{ab}}{dz} + A_{12}\frac{d\theta_{vb}}{dz} + A_{13}\frac{d^2\theta_{tave}}{dz^2} \tag{3.21}$$

$$\theta_{vb} = A_{21}\frac{d\theta_{ab}}{dz} + A_{22}\frac{d\theta_{vb}}{dz} + A_{23}\frac{d^2\theta_{tave}}{dz^2} \tag{3.22}$$

$$\theta_{tave} = A_{31}\frac{d\theta_{ab}}{dz} + A_{32}\frac{d\theta_{vb}}{dz} + A_{33}\frac{d^2\theta_{tave}}{dz^2} \tag{3.23}$$

where A_{11-33} are listed in Appendix 3. If axial conduction is neglected, as in chapter 2, one obtains a reduced set of equations involving only θ_{ab} and θ_{vb}.

The three coupled equations (Eqs.3.21, 3.22, and 3.23) for the vessel bulk temperatures and the average tissue temperature are linear, ordinary differential equations that can be easily solved once the appropriate boundary conditions in the axial direction are specified. For countercurrent flow, this requires that only the artery bulk inlet temperature be

prescribed since as $z\to\infty$, both the venous inlet temperature and the artery bulk temperature approach T_∞. For the tissue region, the average tissue entrance temperature θ_{t0} can differ from the arterial inlet temperature $\theta_{a0}=1$. These boundary conditions are given by

$$\theta_{ab} = 1 \qquad z = 0 \tag{3.24a}$$
$$\theta_{tave} = \theta_{t0} \qquad z = 0 \tag{3.24b}$$
$$\theta_{ab}, \theta_{vb}, \theta_{tave} \to 0 \qquad z \to \infty \tag{3.24c}$$

The general solution of Eqs.3.21, 3.22 and 3.23 is an eigenfunction of the form of e^{BiZ} where the eigenvalues B_i can be negative, positive or a complex variable and the θ_{ab}, θ_{vb}, and $\theta_{t\,ave}$ are arbitrary combinations of all possible eigenfunctions. Due to boundary condition (3.24c), one can exclude eigenfunctions with positive eigenvalues B_i. One finds that θ_{ab}, θ_{vb}, $\theta_{t\,ave}$ must have the functional forms

$$\theta_{ab} = A_1 e^{-B_1 z} + A_2 e^{-B_2 z} \tag{3.25a}$$
$$\theta_{vb} = C_{11} A_1 e^{-B_1 z} + C_{12} A_2 e^{-B_2 z} \tag{3.25b}$$
$$\theta_{tave} = C_{21} A_1 e^{-B_1 z} + C_{22} A_2 e^{-B_2 z} \tag{3.25c}$$

where $C_{11,\ 12,\ 21,\ 22}$ are coefficients calculated from Eqs.3.21, 3.22 and 3.23. The unknown coefficients A_1 and A_2 are determined by boundary conditions (3.24a) and (3.24b).

Conduction shape factor between the artery and the vein in the cross-sectional plane

The expression for the conduction shape factor significantly simplifies for the case of equal size blood vessels symmetrically positioned relative to the vertical axis. If one analyzes the expressions for the coefficients in Eqs.3.21, 3.22 and 3.23, one finds after requiring that the mass flow in each vessel be the same ($\rho_w^2 \bar{u}=-1$),

$$A_{11}=-A_{22}=Pe(-11/96+\frac{K'\pi}{2}\overline{W}_{a-a})$$

$$A_{12}=-A_{21}=\frac{PeK'\pi}{2}\overline{W}_{v-a}$$

$$A_{13}=A_{23}$$

where the coefficients in the above relations are listed in Appendix 3. Subtracting Eq.3.22 from Eq.3.21, one obtains

$$\theta_{ab}-\theta_{vb}=(A_{11}+A_{12})\frac{d(\theta_{ab}+\theta_{vb})}{dz} \tag{3.26}$$

In reference[4], Baish *et al.* have introduced two shape factors σ_Δ and σ_Σ, describing conduction between the artery and the vein, and between both vessels and the tissue, respectively. σ_Δ is obtained by adding Eqs.10 and 11 in reference [4], which is given by

$$\sigma_\Delta=\frac{\pi\gamma_b C_b \rho_{av}^{*2}\overline{u}}{2k_t(T_{ab}-T_{vb})}\frac{d(T_{ab}+T_{vb})}{dz^*} \tag{3.27}$$

Introducing the dimensionless parameters and comparing Eqs.3.26 and 3.27, one obtains the following expression for σ_Δ,

$$\sigma_\Delta=-\frac{\pi}{4(A_{11}+A_{12})}=\frac{1}{2\overline{W}_{va}-2\overline{W}_{aa}+11/(24\pi)} \tag{3.28}$$

Thermal equilibration length in the axial direction

Once the vessel bulk temperatures and the average tissue temperature are known, one can obtain expressions for the vessel temperatures at any location in the vessel region from Eqs.3.12 and 3.13. For the tissue temperature, one substitutes Eqs.3.25a, 3.25b and 3.25c into Eq.3.15, and obtains

$$\theta_t(x,y,z)=F_1(x,y)e^{-E_1 z}+F_2(x,y)e^{-E_2 z} \tag{3.29}$$

where,

$$F_1(x,y)=-C_{21}A_1E_1^2\left(\frac{y^2}{2}+I_1y+I_2\right)+\left[\frac{PeK'\pi}{2}A_1(-E_1)+\pi C_{21}A_1E_1^2\right]W(x,y:\xi_a,\eta_a)+$$
$$\left[\frac{PeK'\pi\rho_w^2\bar{\mu}}{2}A_1C_{11}(-E_1)+\rho_w^2\pi C_{21}A_1E_1^2\right]W(x,y:\xi_v,\eta_v)$$

$$F_2(x,y)=-C_{22}A_2E_2^2\left(\frac{y^2}{2}+I_1y+I_2\right)+\left[\frac{PeK'\pi}{2}A_2(-E_2)+\pi C_{22}A_2E_2^2\right]W(x,y:\xi_a,\eta_a)+$$
$$\left[\frac{PeK'\pi\rho_w^2\bar{\mu}}{2}A_2C_{12}(-E_2)+\rho_w^2\pi C_{22}A_2E_2^2\right]W(x,y:\xi_v,\eta_v)$$

The tissue axial thermal equilibration length is the distance over which the tissue temperature decreases by a factor of e. Comparing Eq.3.25a and Eq.3.29, one finds that the thermal equilibration length calculated from the surface temperature is not the same as that of the feeding artery, even though they are related. Only when the initial average tissue temperature $\theta_{t,ave}$ is equal to either C_{21} or C_{22}, can the tissue temperature be reduced to an expression containing only a single decaying mode. For these special conditions, the tissue temperature and vessel temperature will follow the same temperature decay pattern in the axial direction. For the more general case the tissue temperature has two decaying modes. However, the difference of thermal equilibration lengths between vessel and tissue will be small, if the tissue thickness H is much smaller than the tissue width $2D$ and the temperature gradient across the tissue thickness is small. Thus, we conclude that the thermal equilibration length calculated from the tissue surface temperature is a good approximation to that of the feeding blood vessels. The tissue temperature distribution in the cross-sectional plane at any z is obtained from Eq.3.29.

3.4 Parameters

The thermal properties of the preparation and the surroundings and the geometrical parameters describing the tissue preparation are summarized in Table 1. The convective coefficient h ranges from 5 to 25 W/m^2 ^{0}C corresponding to free convection conditions. The ranges for most of the geometrical parameters are obtained from our experiments on the rat cremaster muscle.

3.5 Results

3.5.1 Axial variation of artery, vein and average tissue temperature

For these results, the radii of the feeding arteriole and venule are chosen as 50 μm, and the preparation thickness is 150 μm. Thus, H_1=1.5 and H_2=3.214. The ratio of equivalent axial thermal conductivity to tissue conductivity k_m/k_t is found to be 2.56. The ratio of artery and vein velocity $\bar{u}$ is determined by requiring that the mass flow in each vessel be the same.

We have examined the effects of several factors on the axial temperature variation and the thermal equilibration length, such as convective coefficient h of the surroundings, the inlet average tissue temperature θ_{t0}, and the blood flow Peclet number Pe. For Pe=8, Figure 14 shows how the inlet average tissue temperature θ_{t0} influences the axial temperature variation in the vessels and the tissue. One notes from Eqs.3.25a, 3.25b and 3.25c that θ_{t0} affects the axial distributions by altering the weighting of the two eigenfunctions in the solution. An elevation of the tissue inlet temperature means that more of the heat leaving the feeding arteriole can return to the venule and thus be prevented from being lost to the surroundings. Therefore, the larger θ_{t0}, the longer the thermal equilibration length of the

feeding artery and the warmer the blood in the returning vein. One observes in Figure 14 that the average tissue temperature $\theta_{t,av}$ closely follows the vein bulk temperature θ_{vb} and, except near the inlet, lies between the artery and vein bulk temperatures. Figure 6 also shows that the axial variation of the dimensionless artery bulk temperature θ_{ab} is significantly altered by changing the convective coefficient h. For Pe=8 and θ_{t0}=1, the dimensionless thermal equilibration length L is reduced from 95 to 40 when the convective coefficient h is increased from 5 to 25 W/m^2.^{0}C. The axial thermal equilibration length L^* decreases from 7.6 mm to 3.2 mm for this increase in h.

The influences of the blood flow Peclet number and the glass plate on the thermal equilibration of the artery are illustrated in Figure 15. Comparing the thin solid line and the long dashed line in Figure 15, one finds that the thermal equilibration length is increased by more than a factor of two due to the presence of the glass supporting slide. There are two principal sources for the axial temperature decay, one is due to axial conduction, the other is due to blood flow. One notes that the thermal equilibration length is proportional to the blood flow Peclet number when axial conduction can be neglected, heavy solid line in Figure 15. However, in our modified model which considers axial conduction, the thermal equilibration length L increases slowly with blood flow Peclet number when $\rho_{ar}^* Pe$ is less than 1 mm. Figure 16 shows the percentage contribution of countercurrent flow to the axial thermal equilibration at two values of tissue inlet temperature θ_{t0}=1.0 and 0.5. L_{conv} is the thermal equilibration length neglecting axial conduction, while $L_{cond+conv}$ is the thermal equilibration length considering both countercurrent flow and axial conduction. One observes in Figures 15 and 16 that axial conduction is the dominant mode of axial thermal

equilibration for the condition that $\rho_w^* Pe < 1$ mm. For $1 < \rho_w^* Pe < 3$ mm, the effect of countercurrent blood flow becomes comparable to axial conduction, whereas, when $\rho_w^* Pe > 3$ mm countercurrent heat exchange becomes dominant. Both curves in Figure 16 predict that for the condition where $\rho_w^* Pe > 3$ mm, the thermal equilibration length due to countercurrent flow accounts for at least 90% of the total equilibration length. Figures 15 and 16 also show that at high blood perfusion rate, the inlet average tissue temperature θ_{s0} has less influence on the axial thermal equilibration and the axial thermal equilibration length is proportional to the blood flow Peclet number as previously predicted in chapter 2.

3.5.2 Surface temperature profiles.

The surface temperature is obtained from Eq.3.29 by setting $y=H_1$. Since the temperature profile across the tissue thickness is almost uniform for small H, the trends for the axial temperature decay at the surface are similar to those for θ_{sb}. Therefore, the effects discussed in Figures 14 and 15 will be nearly the same for the axial surface temperature profiles as the axial temperature profile of the feeding artery.

Figure 17 is a plot of the surface temperature profiles for different θ_{s0}, at two axial locations, one at the entrance, $z=0$ and one far downstream, $z=70$, for two values of h. This figure shows that at the two higher values of θ_{s0}, θ_{s0}=0.9 and 1.0, less heat is lost from the artery to the environment and the surface thermal fluctuation due to the vessels is smaller near the entrance. At higher tissue temperatures, there is a significant countercurrent rewarming of the vein. For $\theta_{s0} < 0.9$ there is a single maximum with no significant minimum for the vein. When the axial distance z increases from 0 to 70, one notes that the shapes of

the temperature profiles are similar and θ_{w} only affects the level of local average tissue temperature. One can show that the location of the surface maximum lies right above the artery. Thus, the horizontal location of the artery can be determined from the maximum in the surface profiles. Figure 17 also shows the initial surface profile for h=25 W/m ^{2}°C for θ_{w0}=0.75. Changing h affects the axial decay but does not have a significant influence on the initial surface temperature distribution.

3.5.3 Comparison of the experimental data and the theoretical results.

The unknown parameter required to compare the experimental data and the theoretical results is the convective coefficient h. Although h cannot be measured directly in our experiments, we can estimate its value by comparing the equilibration length predicted by the theoretical model with that measured from the axial decay of the surface temperature field. For this comparison we have selected $\theta_{w0}=\theta_{v0}$ based on the results in Figure 14. Figure 18 compares the theoretical predictions for the axial surface temperature distribution for one experiment in which results have been obtained for four different values of Pe by drug induced vasodilation and constriction. One finds that when h is selected as 6 W/m^{2}°C the temperature distributions predicted by the model correlate very well with the experimental data for all four blood flow Peclet numbers. While one might choose h to fit one axial profile, the ability to predict all four profiles with the same h is strong support for the validity of the model, since h doesn't change during the course of one experiment. This value of h is reasonable since the normal value of h for free convection on a horizontal tissue surface in air is from 5 to 25 W/m^{2}°C. In Figure 18, one notes that the theoretical predictions

correlate better for low flows than for high flows. However, this does not mean that the theoretical model is more accurate for low flows than for high flows, since one can select another value of h to fit the axial decay curves for high flows. This small deviation from the experimental data is most due to the simplifications and the limitations of the theoretical model, which will be discussed in section 3.6.

The theoretical and experimental surface temperature profiles normal to the main cremaster vessels are shown in Figure 19 for one of the trials (Pe=7.8), at four axial locations. The theoretical results predict a maximum temperature above the feeding arteriole and an almost uniform temperature distribution in the horizontal direction. The theoretical predictions are consistent with the experimental measurements. However, the small but steep temperature gradient between the countercurrent artery-vein pair predicted by the theoretical model was not clearly visible in our experiments. This small temperature difference may have been camouflaged by the scatter in the experimental data or may be due to the simplifications in the model discussed in section 3.6.

3.5.4 Comparison of the theoretical model and the Weinbaum-Jiji equation

The sophisticated model developed in this study provides an accurate basis for examining the validity of simpler one-dimensional models where an effective conductivity k_{eff} is used to describe the enhancement in conductivity due to blood flow. In particular, one can compare the results of the present model with those obtained from the Weinbaum-Jiji equation. Applying the Weinbaum-Jiji equation [36] to the tissue preparation (without glass plate) and introducing the dimensionless parameters shown in section 3.3.1, one can obtain

a simple one-dimensional energy equation for $\theta_{t,ave}(z)$ as follows

$$\frac{d\theta^2_{t,ave}(z)}{dz^2}\frac{k_{eff}}{k_t}=\frac{2Bi}{H}\theta_{t,ave}(z), \quad \frac{k_{eff}}{k_t}=1+\frac{n\pi^2 Pe^2\rho^{*2}_{av}}{4\sigma_\Delta} \tag{3.30}$$

where σ_Δ is the conduction shape factor for heat transfer between two vessels at different temperatures in the cross sectional plane, and n is the countercurrent vessel pair number density per unit of cross-sectional area, which is equal to $1/(2DH\rho_{av}^{*2})$. The solution of Eq.3.30 for the tissue temperature is

$$\theta_{t,ave}=\theta_{t0}e^{-z/L}$$

where the thermal equilibration length L^* is

$$L^*=L\rho^*_{av}=\rho^*_{av}\sqrt{\frac{Hk_t}{2h\rho^*_{av}}}\sqrt{1+\frac{\pi^2Pe^2}{8DH\sigma_\Delta}} \tag{3.31}$$

Here the shape factor σ_Δ can be calculated from Eq.3.28 with H_b=0. Once one knows the value of the tissue inlet temperature, one can compare the axial thermal equilibration length in Eq.3.31 with our modified model prediction in section 3.3.1. Notice that the main assumption in the Weinbaum-Jiji equation is that the axial gradient of the mean of the artery and vein blood temperatures is equal to the axial gradient of the mean tissue temperature. One notes that L^* in the 1-D Weinbaum-Jiji equation is independent of the inlet tissue temperature, while L^* calculated from the 3-D model in this paper depends on the tissue inlet temperature. To minimize this difference due to inlet conditions we have selected $d\theta_{t,ave}/dz = d[(\theta_{ab}+\theta_{vb})/2]/dz$ at the tissue inlet z=0 in the following comparison. Figure 20 compares the tissue equilibration lengths from these two models as a function of ρ_{av}^*Pe for h=5 and 25 W/m^2°C and a vessel center to center spacings l=3. One finds that at lower blood flow rates,

ρ_w^*Pe (< 1 mm), both models correlate very well, while for larger ρ_w^* Pe, the deviation of the Weinbaum-Jiji model from the 3-D model grows as ρ_w^*Pe increases and this difference is greater for the larger *h*. This larger deviation can be traced to the fact that at high *h* the axial tissue temperature gradient is steep, see Figure 14, and the gradient of the average artery-vein bulk temperature will lag that of the average tissue temperature. For the smaller *h* the deviation is less than 20% from the more accurate model for $\rho_w^*Pe < 6$ mm. In general, the Weinbaum-Jiji equation (3.30) underpredicts the thermal equilibration length and k_{eff} for larger values of ρ_w^*Pe because the artery and vein bulk temperature gradients will deviate significantly from the tissue temperature gradient as ρ_w^*Pe increases, see Discussion.

3.6 Discussion

In this study, the thermal fluctuations surrounding microvessels smaller than 150 μm diameter were successfully measured in exteriorized rat cremaster muscle preparations using high-resolution infrared thermography, and the effect of drug induced changes in vessel diameter and flow on thermal equilibration lengths was explored. The experiments are the first to directly measure axial thermal equilibration in the microcirculation. The study therefore demonstrates an important new experimental approach for evaluating basic energy exchange mechanisms in microvascular heat transfer. Experimental results show that only 1A arteries (> 70 μm dia.) show thermal non-equilibration with the surrounding tissue.

The modified theoretical model for a two-dimensional tissue preparation with arbitrarily embedded countercurrent vessels is found to be in good general agreement with the experimental results. Although this model assumes a uniform axial conduction in the cross-

sectional plane, the prediction of the axial thermal equilibration length is found to be accurately modeled since the model considers the global effect of axial conduction in both the tissue and the glass supporting plate. With this simplification the model is able to accurately evaluate the relative importance of countercurrent flow and axial conduction in the tissue preparation.

Several factors may be responsible for the detailed deviations between the theoretical predictions and the experimental results in the tissue width direction. One is the simplification introduced for the glass plate, in which the glass is replaced by an effective tissue thickness. Even if this simplification does not affect global axial conduction, it may affect the temperature distribution locally, especially in the vicinity of the countercurrent blood vessels. Another complication is vessel branching and capillary bleedoff. Although the model can be extended to several vessel pairs or gradually tapered vessels, the thermal interactions among the blood vessels near a branching are still quite complicated. The vessel branching or capillary bleedoff will generate a direct perfusion or a distributed heat sink in the tissue which may smooth the temperature gradient around the countercurrent vessels.

One of the important predictions of the theoretical model is the range of conditions in which countercurrent blood flow is the dominant mode for axial thermal equilibration. Axial conduction and countercurrent blood flow are of comparable importance and each mechanism contributes almost equally to the heat exchange when $1<\rho_w^* Pe<3$ mm. This critical range is found in blood vessels that lie between 160 to 240 μm dia. for normal flow conditions (see next chapter). Countercurrent heat transfer between the blood and the tissue dominates heat transfer in blood vessels when $\rho_w^* Pe>3$ mm, and for these conditions heat

conduction can be neglected.

The study in chapter 4 has predicted the enhancement in the effective conductivity k_{eff}/k_t by measuring the changes in flow and diameter in 1A to 4A blood vessels due to hyperthermia and drug induced vasodilation and applying the Weinbaum-Jiji expression for k_{eff}, equation 30, for each vessel generation. Results have shown that countercurrent blood flow in vessels less than 75 μm dia. does not significantly contribute to k_{eff}/k_t. However, by extrapolating the experimental data, the theory predicted that significant enhancement should start to occur for vessels larger than 80 μm dia.. The predictions in chapter 4 reveal that a 2-fold increase in the effective conductivity k_{eff}/k_t will occur when ρ_w^*Pe, is approximately 1.5 mm and that a 6-fold increase will occur when ρ_w^*Pe=3.0 mm. The transition from conduction to convection dominated axial transport between ρ_w^*Pe equal to 1 and 3 mm predicted by the present model is, therefore, in close agreement with the theoretical predictions for k_{eff}/k_t in chapter 4.

Using a newly derived shape factor for conduction in the cross-sectional plane of the tissue preparation, we have compared the thermal equilibration lengths calculated by the Weinbaum-Jiji model and the more accurate 3-D model. This newly derived conduction shape factor is a function of the local geometry and the convective coefficient h and is found to be much smaller than that calculated from the well-known bipolar solution [10] for perfect countercurrent heat exchange. For l=3.0 and H=3.0, the new derived conduction shape factor is about one-third of the old one [10] and is found to be almost independent of the convection coefficient h. The axial thermal equilibration lengths of the tissue calculated by applying a simple one-dimensional Weinbaum-Jiji model to the tissue preparation are found

to have similar trends to that predicted by the more accurate 3-D theoretical model. We found the Weinbaum-Jiji equation correctly predicts the shape of the axial thermal equilibration length versus $\rho_w{}^*Pe$ curve, even though it underestimates k_{eff} for larger blood perfusion rates. This underestimation of k_{eff} can be traced to the assumption in the Weinbaum-Jiji equation that the gradient of the mean tissue temperature is equal to the gradient of the mean blood temperature.

Asymptotic analyses presented in reference [35] rigorously shows that the validity of this assumption requires that, $\epsilon = L^*/L^*_{length}$, the normalized thermal equilibration length of the blood vessels be < 0.2. Here L^*_{length} is either the vessel length or the characteristic length of the tissue temperature gradient. When $\rho_w{}^*Pe$ < 1 mm, the conditions of the present experiments, the thermal equilibration lengths of the blood vessels in the countercurrent network are small compared to the length scale of the macroscopic temperature gradients in the tissue. For these conditions, the Weinbaum-Jiji equation is in good agreement with the more accurate 3-D model. However, for $\rho_w{}^*Pe$ > 1 mm, the accuracy of the Weinbaum-Jiji equation depends on the value of h. For small h the decay length is longer and the vessel bulk temperatures will closely follow the tissue temperature gradient, see Figure 14. For this case the thermal equilibration between the artery-vein pairs will not depart significantly from nearly perfect countercurrent exchange and the Weinbaum-Jiji model will still be a good approximation although $\rho_w{}^*Pe$ > 1 mm. However, for larger h the tissue decay length will be short, ϵ will be > 0.2, and the criterion for the validity of the Weinbaum-Jiji equation will be exceeded.

Chapter 4. Vasomotor Responses to Local Heating in the Rat Cremaster Preparation

In this chapter we shall first experimentally examine the hyperthermic response of individual microvessels in skeletal muscle tissue subject to local heating and then predict the enhancement in thermal conductivity that results from the observed changes in vascular diameter and flow. In contrast to existing studies, which have tried to relate changes in tissue thermal conductivity to local blood perfusion using thermal clearance and self-heated thermistor techniques, we have developed a two-dimensional muscle tissue preparation in which the hyperemic response has been quantified by measuring the *in vivo* changes in diameter and blood flow of 1A to 4A generation vessels of rat cremaster muscle when the temperature was raised in two-degree increments from 34 to 42 ^{0}C. Only 3A and 4A vessels showed vasodilation when subject to hyperthermia indicating that the measured increase in flow in the 1A and 2A vessels was the result of a decrease in downstream resistance. Our cremaster muscle preparations have also been used to obtain the first detailed anatomic measurements of the number density and length of countercurrent vessel pairs between 50 to 200 μm diameter. These combined measurements have been used to establish the limits of validity of the Weinbaum-Jiji theory. Our experimental data indicate that the Weinbaum-Jiji expression for k_{eff} is valid in the cremaster muscle and the cat mesentery tissue for both normal and hyperthermic conditions provided the largest vessels are < 200 μm diameter. The theory predicts that significant enhancements in k_{eff} is present for vessels that are 70 μm dia. or larger, that a 2.5 fold increase in k_{eff} can be achieved for maximally dilated 200 μm dia.

1A vessel pair in cremaster muscle of larger rats and a sixfold increase predicted for maximally dilated 200 μm dia. vessels in the cat mesentery.

4.1 Introduction

Many previous investigators have measured the effective thermal conductivity of the perfused tissue using heat clearance techniques in which a self-heated thermistor probe is placed in the tissue [2, 7, 9, 28, 33] and the local blood perfusion rate is either predicted using various heat transfer models that relate the measured conductivity to perfusion rate or calibrated by comparison with *in vitro* measurements in which the flow to an entire artificially perfused organ is measured rather than the local perfusion in the vicinity of the probe. Three recent investigations [1, 15, 41] have attempted to evaluate the accuracy of various heat transfer models using thermal clearance measurements in the renal cortex of isolated bovine, pig and dog kidneys perfused with saline. The studies [1, 41] have also tried to relate the vascular anatomy of the cortex to the conductivity of the perfused tissue using the expression for the effective conductivity derived in Weinbaum and Jiji [36] for countercurrent heat exchange between thermally significant artery-vein pairs in the microcirculation. The theory is difficult to apply in this organ because of the complexity of the vascular anatomy and the fact that, unlike skeletal muscle tissue, the arteries and veins in the renal cortex do not occur primarily as countercurrent pairs [1].

In this chapter, we shall present a new experimental approach to microvascular heat transfer and the enhancement in conductivity that is associated with the hyperemic response to hyperthermia using an *in vivo* two-dimensional tissue preparation, the

exteriorized rat cremaster muscle. We first examined the flow and diameter in 1A to 4A arterioles at 34 °C, the normal tissue temperature for these vessels *in vivo*. This is considered to be the reference state. To establish bounds on the magnitude of the microvascular thermal response to local tissue heating, we attempted to separate the direct and indirect thermal responses. Direct effects of temperature are those associated with direct changes in cellular pathways leading to changes in the state of the contractile proteins of the vascular smooth muscle [34]. Such temperature induced cellular changes include alteration in cell membrane potential, Ca^{2+} ion channel conductance and intracellular enzymatic activity. In contrast, indirect thermal effects are associated with temperature induced changes in the smooth muscle response to extracellular chemical substances including endothelial released factors, hormones and neurotransmitters [34]. These chemical substances initiate vascular smooth muscle contraction and vasodilation by binding to smooth muscle adrenergic and other membrane receptors or diffusing into the cell and activating intracellular responses. To separate the two responses we minimized the indirect thermal effect by introducing antagonists which block the α, and β adrenergic receptor pathways. The direct thermal effect that remained could be treated as the lower bound for the hyperemic response to local tissue heating.

The pioneering studies by Flavahan and Vanhoutte [19] showed that the constriction of the large superficial veins initiated by the neurotransmitter norepinephrine (NE) released from the sympathetic nerves and binding to the α_2 receptor, is greater after moderate cooling and reduced following warming. A similar effect of local tissue cooling in a microvascular bed was then observed by Faber [18] in the rat cremaster muscle.

Unfortunately, no equivalent study of the indirect thermal effects on microvascular smooth muscle has been performed for local tissue heating. It is therefore difficult to establish temperature-dependent upper bounds which exhibit the combined effects of the direct and indirect thermal response. To reach a maximum response for a standard point of comparison we have added Na nitroprusside, a vascular smooth muscle relaxant, to achieve the maximum dilation of the microvascular bed.

Earlier theoretical studies [10, 12, 37] have predicted that the smallest thermally significant microvessels are approximately 50 μm dia. In the present study we have measured the velocity in vessels which lie in the range 10 to 80 μm diameter and have obtained detailed anatomical data for vessels up to 200 μm diameter. The upper limit in vessel diameter is determined by the limitations of our optical Doppler velocimeter to accurately measure the red cell velocity in larger vessels. For vessels > 80 μm diameter we have used the more extensive velocity vs. diameter measurements in House and Lipowsky [22] on the rat cremaster and Zweifach and Lipowsky [44] on the cat mesentery, and have applied the velocity vs. diameter regression relations in [22, 44] for vessels up to 200 μm diameter. The enhancement in effective conductivity k_{eff} will be calculated from our velocity and anatomical measurements using the theory for k_{eff} developed in Weinbaum and Jiji [36]. It was shown through asymptotic analysis [35] and comparison with detailed numerical solutions of a three-equation model where the artery and vein temperatures were calculated [11] that there are important limitations on the validity of the Weinbaum-Jiji model equation from which the expression for k_{eff} is obtained. In particular, the Weinbaum-Jiji model requires that all thermally significant

microvessels appear as countercurrent artery-vein pairs and that the ratio of L^*/L^*_{length} of the thermal equilibration length L^* to the vessel length L_{length} be < 0.2. In [11] it is shown that the requirement that the axial gradients of the artery and vein temperatures closely follow the gradient of the tissue temperature, the criterion for the validity of the Weinbaum-Jiji equation, is well satisfied for $L^*/L^*_{length} < 0.2$. Thus, the predictions in this paper contain the first reliable estimates as to the size of the vessels that can be treated within the framework of the Weinbaum-Jiji approach for both normal and hyperthermic conditions and the increase in k_{eff} due to flow and diameter changes. The rat cremaster is an ideal preparation for this evaluation since, as observed in Figure 1, all thermally significant vessels (vessels > 50 μm dia.) occur as countercurrent artery-vein pairs and, as will be shown, all vessel pairs satisfy the criterion, $L^*/L^*_{length} < 0.2$.

While rough estimates have been made to evaluate the key flow and anatomical parameters that have appeared in the Weinbaum-Jiji model, such as L^*, L^*_{length}, Peclet number Pe, and vessel pair number density n, this is the first time that careful anatomical and flow measurements have been made to evaluate all the key parameters in the model.

Three very important results have emerged from this study. First, it will be shown that there is negligible enhancement in tissue conductivity in the rat cremaster muscle for vessels less than 60 μm dia. and that significant enhancements in effective conductivity start to occur for vessels that are 80 μm or larger. Second, it will be shown, at least for the direct thermal response, that changes in vessel diameter with local tissue heating occur only in the thermally insignificant 3A and 4A vessels and that changes in the flow upstream (1A and 2A vessels) are due primarily to the change in the vascular resistance

downstream. It is thus possible to establish bounds on the changes in conductivity that will result from the hyperemic response in the larger vessels upstream by using our experimental data obtained from the 3A and 4A vessels where the vessel diameter is changing and the local microvascular flow is regulated. Third, it will be shown that the criterion for the validity of the Weinbaum-Jiji expression for k_{eff} are valid in cremaster muscle and cat mesentery tissue for both normal and hyperthermic conditions provided the vessels do not exceed 200 μm dia..

In this chapter, we first present our experimental investigation of the direct temperature effect on blood vessels in rat cremaster muscle due to local heating and the maximum vasodilation due to Na nitroprusside. We then apply the velocity vs. diameter regression relations in [22, 44] to larger vessels up to 200 μm dia. and predict the range of enhancement of thermal conductivity for normal flow conditions. The approximate enhancement in flow in larger vessels due to hyperthermia is then estimated from the enhancement in flow in 1A and 2A vessels that we measured in our own experiments. Finally, we use this enhancement in flow to predict the enhancement of thermal conductivity for the direct thermal and maximum hyperemic response.

4.2 Experimental Method

4.2.1 Method

Thirty-six male Sprague-Dawley rats (Mean±SD, 53±7g) were used in this study. The animals were anesthetized with an intraperitoneal injection of sodium pentobarbital solution (40mg/kg). Supplemental doses were administered as needed. A tracheal tube was inserted

to maintain a patent airway. After anesthesia, the rat was placed on a water-jacketed pad to maintain rectal temperature, which was monitored throughout the experiment with a thermocouple inserted into the rectum. The surgical procedure required about 0.5 hour and the subsequent experimental procedure required about 2 hours.

The left cremaster muscle was dissected free from the scrotal skin and testicle for *in vivo* microvascular observation as described previously [4, 13]. This exteriorized cremaster muscle was extended into a flattened sheet with silk sutures over an optical window in a tissue bath initially set at 34 ^{0}C, which is close to the *in vivo* scrotal temperature. The schematic diagram for the experimental setup is shown in Figure 21. There was a jacket of water around the bath and its tubing. The out-layer water was circulated to control the tissue bath temperature. The tissue bathing solution was recirculated from a stock reservoir containing a modified Krebs solution that consisted of (in g/liter) 6.6 NaCl, 0.35 KCl, 0.28 $MgSO_4$, 0.16 KH_2PO_4, 2.09 dextrose and 2.14 $NaHCO_3$ dissolved in filtrated water as well as the α_1/α_2 and β blocking drugs phentolamine (10^{-6} M) and propranolol (10^{-6} M), respectively. The muscle is sensitive to PO_2, PCO_2 and pH, which were all monitored by an Anafaze 8LS controller which adjusted the bubbling rate of CO_2 and N_2 in the stock reservoir to maintain a PO_2 of 15-30 torr, a PCO_2 of 35-45 torr and a pH of 7.4.

The preparation was transilluminated on the microscope stage (Zeiss, ACM) and viewed through a 20X or 40X Nikon water immersion objective. The microcirculation during the experiment was displayed on a closed-circuit camera and recorded for further analysis. The volume flow in the individual arteriole was estimated [6] using the equation

$$Q = \frac{\pi \rho_w^{*2} V}{1.6 \times 1000} \tag{4.1}$$

where Q is volume flow (nl.s^{-1}), V is centerline red cell velocity of the microvessel (mm.s^{-1}) which was measured with an optical Doppler velocimeter (Microcirculation Research) during the experiment and ρ_w^* is vessel radius (μm) measured from the video tape with an electronic video caliper (Microcirculation Research). The bath temperature was measured by three calibrated copper-constantan thermocouples held on three locations inside the water-jacketed bath to insure that bath temperature was uniform. The experiment was controlled and data were acquired and recorded with LabView® software running on a Macintosh computer.

4.2.2 Measurement protocol

The preparation was examined before the start of the measurement protocol and if there was any bleeding or low blood flow, the experiment was interrupted until either the bleeding was stopped or the experiment was terminated.

Only one microvessel (1A, 2A, 3A or 4A) was chosen for study in each experiment. The classification scheme identifies the main arteriole feeding the cremaster muscle as the first-order arteriole (1A). Successive branches from the 1A were defined as second-order arterioles (2A). Similarly, branches from 2A were designated as third-order arterioles (3A), etc. This classification scheme is indicated directly on the photomontage in Figure 1. Initially, a 30 to 60 min stabilization period at 34 °C followed surgery to allow the preparation to achieve an initial steady state. There were then five trials in each experiment

representing five bath and local tissue temperatures (34 °C, 36 °C, 38 °C, 40 °C, 42 °C). After the bath temperature was increased there was a 10 min. period for the preparation to reach each new equilibrium. After all the parameters (temperature, velocity and diameter) were stable, the image of the vessel, the centerline red blood cell velocity and the bath and the rectal temperatures were recorded continuously for a three-minute measurement period. Bath temperature was increased in two degree increments by the changing temperature of the water circulating through the water jacket of the bath and reservoir. After each increment the preparation would reach a new equilibrium with the bath solution and the procedure described above would be repeated until the trial at 42 °C was finished. At the end of the experiment, Na nitroprusside ($10^{-4.5}$ M) was added to achieve the maximum dilation of the microvascular bed. All the velocity and diameter data were expressed as a percentage of this maximally dilatory dose. This drug induced maximum dilation was used as an upper bound for the hyperemic response.

4.2.3 Statistical analysis.

For each experiment, the average values during the 3-minute data collecting period of the velocity and diameter of 1A, 2A, 3A or 4A vessels were calculated. The differences among the mean values for each bath temperature were determined using one-way ANOVA. The post-hoc comparisons between control temperature(34 °C) and other temperatures were performed by Dunnett's method [38]. Significance was evaluated at the 5% confidence level.

4.3 Experimental Results

The data obtained at the control temperature of 34 °C (velocity, diameter and flow rate) for both the normal and maximum vasodilatory response elicited after Na nitroprusside injection are listed in Tables 2 and 3. One observes that the ratio of volumetric flow rate to the cube of vessel diameter, $Q/(2\rho_w)^3$, is nearly constant for different vessel generations, at 34 °C for either normal flow. This indicates that Murray's Law is approximately satisfied in the branches of rat cremaster muscle for normal conditions [24].

Figure 22 shows the temperature-dependence of diameter and centerline velocity of 1A, 2A, 3A and 4A arterioles due to the direct thermal response. All the values are expressed as a percentage of the maximum dilatory response elicited by Na nitroprusside. The 1A and 2A arterioles showed no significant dilation for temperatures up to 42 °C. The 3A arterioles dilated about 10% above the control state at 42 °C and showed a smaller response at lower temperatures. The average diameter of 4A arterioles had a maximum increase of 30% at the highest temperature. However, large increases from 25% to 37% in the blood velocity were observed for all arterioles. Volume flow increase over the control state is showed in Figure 23. In comparison with the control state, the volume flow rate increased about 40 percent when the preparation was heated to 42 °C for most arterioles. In contrast, the maximum dilatory response produced a roughly two-fold increase in flow for the 1A and 2A vessels, a threefold increase for the 3A vessels and a fivefold increase in the 4A arterioles. The average rectal temperature of all the rats rose about two degrees over the course of the experiment.

4.4 Enhancement in Conductivity

In the foregoing *in vivo* experiments, we measured both vessel diameter and blood flow velocity for different arterioles ranging in size from 10 to 70 μm dia. in the normal state (34 ^{0}C) and for 12 to 87 μm dia. vessels for conditions of maximum dilation. We shall show, however, that nearly all the thermally induced vasoregulation occurs in 3A and 4A vessels and thus it is possible to predict the increase in flow in larger 1A and 2A vessels using the results of our experiments with small rats for both the normal state and for hyperthermic conditions.

Figure 1 shows a photomontage of rat cremaster muscle preparation provided by Dr. H. H. Lipowsky. The weight of the rat was 70 g. All 1A and 2A vessels and most 3A vessels in the preparation appear as countercurrent artery-vein pairs. All 4A vessels are transverse vessels that supply the capillary beds. Depending on rat age and size, the 1A feeding arteriole can range in size from 50 to 200 μm dia. and the countercurrent veins are typically 50 percent larger. Previous theoretical studies suggest that these are the most important vessels in blood-tissue energy exchange [12, 37]. Thus, the rat cremaster muscle provides a realistic *in vivo* model for evaluating the enhancement of thermal conductivity due to countercurrent flow. The general expression for the tensor conductivity $(k_{ij})_{eff}$ derived in Weinbaum and Jiji [36] is given by

$$(k_{ij})_{eff}=k_f\left(\delta_{ij}+\sum_i \frac{k_b^2}{k_t^2}\frac{n_i\pi^2\rho_{av}^{*2}Pe^2}{4\sigma}l_i l_j\right), \qquad Pe=2\gamma_f C_f \rho_{av}^{*} u/k_f \tag{4.2}$$

where l_i are the direction cosines of the vessel axis relative to the local tissue temperature gradient, Pe is the blood flow Peclet number, u is the average velocity of the blood flow. σ

is the shape factor defined below and n_i is the vessel pair number density per unit cross-sectional area in generation i. Eq.4.2 is for countercurrent arteries and veins of equal radius ρ_w^*. This theory has been generalized in Zhu *et al.* [43] for vessel pairs of unequal diameter. Instead of using this more complicated expression we have let ρ_w^* be the mean radius of the artery-vein pair. In the following analysis we have also set k_f equal to k_t for convenience and simplified the expression for the effective thermal conductivity in Eq.4.2 for the case where $l_j = 1$,

$$k_{eff} = k_t\left(1 + \sum_i \frac{n_i \pi^2 \rho_w^{*2} Pe^2}{4\sigma}\right) = k_t\left(1 + \sum_i n_i \sigma L_i^{*2}\right) \tag{4.3}$$

Here $L_i^* = \pi\rho_w^* Pe/(2\sigma)$ is the characteristic thermal equilibration length for vessel generation i. Eq.4.3 is the summation of enhancement contributions from different generations of countercurrent pairs. The expression for σ, the conduction shape factor for heat transfer between two vessels at different temperatures [10], is

$$\sigma = \pi / \cosh^{-1}[l^*/(2\rho_w^*)] \tag{4.4}$$

where l^* is the center to center spacing between vessels. For most 1A to 3A vessel pairs l^*/ρ_w^* lies in the range 2.2 to 3.0. σ decreases from 7.14 to 3.26 over this range. For 1A and 2A vessels a good average approximation for l^*/ρ_w^* is 2.5 for which σ=4.53.

4.4.1 Enhancement in k_{eff} for blood vessels < 80 μm diameter

To evaluate the enhancement in thermal conductivity described by Eq. 4.3 and the criterion $L^*/L^*_{length} < 0.2$ for its validity, we need to determine η, the vessel pair number density per unit cross-sectional area in generation i, and vessel length $(L^*_{length})_i$, as well as

the relationship between the vessel blood flow velocity and vessel diameter. As noted earlier the latter relationship is approximately given by $Q/(2\rho_{rbc}^{*})^3$ = constant. The determination of n_i and $(L^{*}_{length})_i$ requires a detailed analysis of the microvascular network structure of the countercurrent artery-vein pairs in the rat cremaster muscle. Engelson *et al.* [17] have studied the bifurcation pattern of various arterioles in the rat spinotrapezius muscle preparations and Meininger *et al.* [26] have studied the anatomic arrangement of the feeding arteries located upstream in the rat cremaster microcirculation. However, neither study gives anatomic data for n_i and L_i. To our knowledge this is the first time these parameters have been carefully evaluated for a microvascular tissue preparation. The data for n_i and $(L^{*}_{length})_i$ have been obtained from five photomontages of rat cremaster muscle preparations using rats weighing from 70 to 200 g in addition to the photomontage shown in Figure 1. Each montage contains 60 to 100 photographs. The procedure for obtaining cremaster preparations is the same as that described in section 4.2.

In Table 4, L^{*}_{vessel} is the total length of countercurrent vessel pairs for each generation in the photomontage. $A^{*}_{surface}$ is the surface area of the montage. N is the number of vessels of each generation in the micrograph. $(L^{*}_{length})_i$ is the average vessel length for each generation. The value of n_i has been estimated by the following formula

$$n_i = \frac{L^{*}_{vessel} / A^{*}_{surface}}{thickness\ of\ tissue\ preparation} \qquad (4.5)$$

where the average thickness of the tissue preparation is from 0.3 to 0.4 mm. Vessel size is based on the average countercurrent artery-vein pair diameter for each generation. As obtained in Table 3 data has been obtained for 1A to 3A vessel pairs that vary in size form

30 to 187 μm dia.. This covers the entire range of values for which Eq.4.3 for k_{eff} will be used.

To obtain suitable regression formulas for analysis, we have plotted in Figure 24 all the data for L_i and n_i as a function of vessel diameter and the regression formula calculated by SlideWrite*plus*™ software. The curve fits are performed using a least squares regression fit according to specific formulas. The R values for both curves are 0.90. R value is the square root of the coefficient of determination (usually called R squared), which is an indication of how well the curve fits the scatter of the data. A R value of 1 indicates a "perfect" fit. The regression formulas are given by

$$\begin{aligned} n_i &= 95.95(2\rho_{av}^*)^{-1.18} \\ (L_{length}^*)_i &= 0.025(2\rho_{av}^*)^{1.144} \end{aligned} \tag{4.6}$$

In Tables 5 and 6 we have calculated the value of $n_i \rho_{av}^{*2} Pe^2$ in Eq.4.3 for each vessel generation in the rat cremaster muscle at 34 °C, where the relationship between vessel blood flow velocity and vessel diameter is obtained from our experimental results in Tables 2 and 3. Since the vessel number density n_i and vessel length $(L_{length}^*)_i$ do not change when we vasodilate the vessels, these parameters are the same in Tables 5 and 6. The shape factor σ in k_{eff} is a function of vessel spacing l^*/ρ_{av}^* and does not change significantly when the vessels are dilated. To a first approximation the thickness of the tissue gap between the vessels does not change, since this dimension is small compared to the spacing between vessel pairs. In effect, the tissue between the countercurrent pairs can be treated as nearly incompressible and the center to center spacing of the vessels increased to accommodate the vasodilation. This behavior is qualitatively confirmed by microscopic observation. One can

show theoretically for an elastic solid that most of the displacement of the tissue occurs on the outer aspect of the vessels since the normal force on the vessel walls is constant and the normal strain in the tissue must be equalized. If this is the case, the change in σ for a vasodilation from 60 to 74 μm dia. (1A vessels in Tables 5 and 6) is only about 10% if the initial vessel spacing $l^*/\rho_{av}^* \approx 2.5$. Thus in this study, we assume that the shape factor is a constant with a average value of 4.53, which corresponds to an average vessel spacing l^*/ρ_{av}^* ~ 2.5, for both normal and hyperthermic conditions.

The important point to be drawn from the next to last column of Tables 5 and 6 is that the decrease in the contribution to k_{eff} with each vessel generation is very rapid and for practical purposes only the largest vessels in the cross section need be considered. Therefore, when we calculate the enhancement of thermal conductivity due to different generations of countercurrent pairs, we can neglect the contributions of all but the first one or two generations. This simplification had been previously suggested in Weinbaum and Jiji [36], but not previously documented by adequate anatomical data. The ratio of k_{eff}/k_t for the 1A vessels is < 1.02 for normal conditions and <1.05 for conditions of maximum dilation where the 1A vessels have a diameter of 74.3 μm and the flow (~ $\rho_{av}^* Pe$) has increased by a factor of 2.1.

Previous studies have placed a lower bound of 50 μm [12, 37] on the diameter of vessels that are thermally significant. The present model indicates that a more realistic lower bound is probably closer to 70 μm diameter even if the vessels are maximally dilated. One notes that the value of L^*/L^*_{length} in Table 5 is less than 0.03 and thus all vessels in our preparations will equilibrate in a distance which is much less than their length. These predictions are

consistent with the experimental measurements in Lemons *et al.* [25] where the smallest arteries with a detectable thermal disturbance were > 100 μm diameter.

4.4.2 k_{eff} for vessels > 80 μm and limit of validity of the WJ equation

In our experimental studies, we only measured the relationship between blood flow velocity and vessel diameter for vessels up to 75 μm dia.. However, the data clearly show that the relationship $Q/(2\rho_w^*)^3$ is approximately satisfied for both normal and vasodilatory condition, see Tables 2 and 3. A more detailed analysis of this relationship is given in Zweifach and Lipowsky [44]. The distribution of centerline velocity in cat mesentery preparations (CMP) has been measured in over 40 animals, and House and Lipowsky [22], where this relationship has been examined in 30 rat cremaster muscle preparations (RCP) in vessels up to 120 μm dia.. For the purposes of this study we shall use the regression formulas in Zweifach and Lipowsky [44] and in House and Lipowsky [22] to evaluate the velocity vs. diameter relation in larger vessels. Their regression formulas for the mean velocity u vs. vessel diameter $2\rho_w^*$ are given by

$$\textit{rat cremaster}: \quad u(mm/s) = 0.28\,(2\rho_w^*\,(\mu m))^{0.73} \tag{4.7a}$$

$$\textit{cat mesentery}: \quad u(mm/s) = 0.21\,(2\rho_w^*\,(\mu m))^{0.91} \tag{4.7b}$$

The R values for Eqs.4.7a and 4.7b are 0.85. Also note that Eqs.4.7a and 4.7b are close to the condition $u/\rho_w^* = \text{constant}$ that follows from the relationship $Q/(2\rho_w^*)^3 = \text{constant}$. The increase in thermal equilibration length of vessels, $L^*=\pi\rho_w^*Pe/(2\sigma)$, with diameter as well as the dimensionless parameter $\epsilon=L^*/L^*_{length}$ can be evaluated to check the validity of the Weinbaum-Jiji equation using the relationships between velocity and diameter in Eqs.4.7a

and 4.7b. Table 7 shows the range of the dimensionless parameter ϵ and the enhancement of thermal conductivity k_{eff}/k_t in the normal state. The values of L^* and n are calculated from the regression curves in Eq.4.6. The shape factor σ is again selected to be 4.53.

As shown by the asymptotic analysis in Weinbaum and Jiji [36] the Weinbaum-Jiji bioheat equation provides reasonable accuracy provided $L^*/L^*_{krogh} < 0.2$. As shown in Charny *et al.* [11] this condition guarantees that $\partial T/\partial x \sim \partial T_a/\partial x \sim \partial T_v/\partial x$ and that the local tissue temperature T be close to the mean of the artery-vein temperature. Using this criterion, one concludes from Table 6 that the Weinbaum-Jiji equation and Eq.4.3 for $(k_{ij})_{eff}$ is satisfied for normal flow condition in both the rat cremaster and cat mesentery for vessels up to 200 μm dia.. Table 7 reveals that for countercurrent artery-vein pairs with vessel diameter > 80 μm, the enhancement of thermal conductivity can be appreciable even for the normal flow conditions and that the ratio k_{eff}/k_t can exceed 2.2 in the cat mesentery when $2\rho_w^* \sim 200$ μm dia..

4.4.3 Evaluation of enhancement in effective thermal conductivity due to local heating

Our next objective is to estimate the enhancement of thermal conductivity due to countercurrent flow associated with the direct thermal response and the maximum dilatory response due to local heating in vessels from 80 to 200 μm dia.. The data obtained from the direct temperature response in rat cremaster muscle can be treated as a lower bound for the hyperemic responses while the maximum dilation responses can be treated as the upper bound for hyperthermia due to any factor.

Our experiments reveal that the local thermal vasomotor response is largely confined

to the 3A and 4A vessel generations, but the change in flow is also present in upstream 1A and 2A vessels. The local volume flow increase due to heating in 1A and 2A arterioles is achieved by the decrease of microvascular resistance in the cremaster muscle due to the dilation of 4A arterioles and some 3A arterioles. Table 8 provides the volume flow increase due to local heating. We consider two cases, one is for the direct temperature response, the other is for the maximum dilatory response of the microvascular bed following Na nitroprusside injection. The latter is considered as the maximum response the microvascular bed can achieve. We found that the percentage changes in flow in 1A and 2A countercurrent pairs are nearly the same. This suggests that there will be a nearly uniform flow response in the thermally significant vessels > 75 μm diameter (see Table 4 for largest 3A vessels) throughout the local microvascular bed since flow regulation occurs downstream. The volume flow increase due to local heating in blood vessels 75 μm dia. or larger which lie upstream of the 1A vessels should, therefore, be the same as the measured increases in the 1A and 2A arterioles in our rat cremaster muscle experiment. If this is the case, we can estimate the enhancement of thermal conductivity of countercurrent flow in vessels from 80 to 200 μm dia. due to local heating using the measured increases in our 1A and 2A vessels. For our lower bound we assume that local heating can induce approximately 36% increase in volume flow, the direct thermal effect, while for our upper bound we assume that the volume flow increases approximately 116% compared with the normal state, the maximum dilatory response.

In Table 9, we estimate the upper and lower bounds on effective thermal conductivity due to local heating. Since $\rho_w{}^*Pe$ is proportional to the local volume flow Q, the expression

for the effective thermal conductivity in Eq.4.3 can be rewritten as

$$k_{eff} = k_f(1 + AQ^2) \tag{4.8}$$

where $A = (n\gamma_f^2 C_f^2)/(4\alpha k_f^2)$. If the geometric parameters and thermal properties are kept constant, the enhancement in thermal conductivity due to the countercurrent flow is proportional to the square of local volume flow Q. Therefore, the ratio of k_{eff} during hyperthermia, denoted by subscript h, to k_{eff} under normal conditions, denoted by subscript n, is given by

$$\frac{(k_{eff})_h}{(k_{eff})_n} = \frac{1 + AQ_h^2}{1 + AQ_n^2} = \frac{1 + AQ_n^2\left(\frac{Q_h}{Q_n}\right)^2}{1 + AQ_n^2} \tag{4.9}$$

This k_{eff} ratio can be easily calculated from the ratio of blood flow rate Q_h during hyperthermia to that in the normal state Q_n given in Table 8. Although the same volume flow increases, 36% and 116% are assumed for each vessel size in Table 9, the absolute enhancement in thermal conductivity increases sharply as the vessel size increases since total enhancement is proportional to the enhancement in the normal state AQ_n^2, which is given in Table 8. For the 200 μm dia. vessel pairs k_{eff} has increased 2.5 fold for the RCP and more than sixfold for the CMP for conditions of maximum dilation. We also note that the condition $L^*/L^*_{length} < 0.2$ is not exceeded, even for conditions of maximum vasodilation, unless the mean diameter of the vessel pair exceeds 200 μm.

4.5 Concluding Comments

Our measurements for the direct temperature response in rat cremaster muscle

demonstrate that this response is only about one third of the maximal flow response that can be achieved. It is not known at this time whether the temperature and drug induced flow enhancement in Table 8 is typical of most muscle tissue or differs significantly between tissues. We have assumed in our predictions a similar enhancement for cat mesentery, but this is still to be measured. The local volume flow increase is achieved by the decrease of microvascular resistance on the cremaster muscle due primarily to the dilation of 4A arterioles. The question is whether 4A arterioles exhibit a similar dilation in other tissues. Since the adrenergic receptors were blocked by drugs, nerve and hormonal effects via the adrenergic pathways had been eliminated. Thus, the hyperemic response must be primarily due to the temperature influence on the vascular smooth muscle or endothelium. The part of the vasodilator pathway which is affected by heating is still unknown. This pathway could be involved in maintaining smooth muscle tone.

These experiments when combined with the Weinbaum-Jiji bioheat theory have provided the first direct predictions of the enhancement in thermal conductivity in a local microvascular bed as well as the hyperemic response to hyperthermia. We found that for blood vessels less than 75 μm dia. there is no significant enhancement of thermal conductivity. The relationships between blood flow velocity and vessel diameter when applied in evaluating L^*/L^*_{length} show that the criterion for the validity of the Weinbaum-Jiji equation is satisfied in vessels up to approximately 200 μm dia.. For larger vessels the blood perfusion contribution to k_{eff} does not continue to increase as $\rho_w^{*\,2}Pe^2$ or Q^2 increases since the vessel pairs do not behave as nearly perfect countercurrent heat exchanges. The power of $\rho_w^* Pe$ decreases and eventually approaches a Pennes type enhancement proportional to

$\rho_{ar}{}^{*}Pe$ or Q. while the present analysis has been able to establish a lower bound on vessel diameter of approximately 70 μm for k_{eff} enhancement, the theory is not valid for predicting an effective upper bound since for vessels > 200 μm dia., $L^{*}/L^{*}_{length} > 0.2$.

The results of this study indicate that a combined modeling approach should be adopted in which vessels larger than 200 μm are modeled discretely, or a heat source term is used as in the Pennes bioheat equation, and that the tissue surrounding these vessels be modeled by an effective conductivity to describe the blood perfusion in all vessels less than 200 μm dia.. The model for these small vessels depends on the tissue. For skeletal muscle nearly all vessels > 70 μm, the threshold for blood flow enhanced conductivity, occur as closely spaced countercurrent pairs. Other tissues, such as the kidney cortex and tumors, do not have a dominant countercurrent architecture. The model for k_{eff} for these tissues still needs to be developed. This general philosophical approach has just been examined in Crezee *et al.* [13]. A principal difficulty at this time is that vessels between about 200 and 500 μm dia. are too numerous to treat individually and are not well described by either the Pennes or Weinbaum-Jiji models.

Chapter 5. Conclusion

The basic three-dimensional mathematic model presented in chapter 2 has provided the starting point for analyzing the heat transfer in two-dimensional tissue preparations with two or more axially interacting eccentrically embedded blood vessels. The primary objective in obtaining this new solution was the design of an experimental method to study the mechanism of microvascular thermal equilibration between thermally significant countercurrent artery-vein pairs in muscle tissue. We have been able to derive a relatively simple closed form expression for a Green's function for conduction heat transfer from a line source in a plane perpendicular to the vessel axes which satisfies all the boundary conditions on the tissue layer and matching conditions at the vessel surface when K', the ratio of the blood to tissue conductivity, is unity. By superposition of Green's functions we are able to treat the axial thermal interaction between a countercurrent vessel pair. In this new approach the axial temperature gradients in the vessels are approximated by the bulk temperature gradients while the vessel wall temperatures are allowed to be non-uniform. This approximation greatly simplified the equations so that the axial interaction was reduced to two linear first-order ordinary equations. The theoretical model predicts that the axial distance, over which measurable thermal disturbances can be detected in an air bath preparation are about four times longer than in a water bath preparation. This prediction is employed in the design of our experimental setup described in chapter 3.

A new experimental approach was developed in chapter 3 to obtain the first direct measurements of microvascular axial countercurrent thermal equilibration in a muscle tissue.

These measurements, performed on a rat cremaster muscle, represent a major advance in microcirculatory heat transfer analysis. A non-invasive high-resolution infrared thermographic technique was used to measure the detailed *in vivo* surface temperature field above individual microvessels. Vasoactive pharmacological agents were employed to change the local blood flow Peclet number from 1 to 14 in the feeding artery. This experiment elucidates where vascular heat transfer occurs and how the axial equilibration length is related to the local blood perfusion rate. Measurable temperature disturbances due to countercurrent blood flow were found only above the 1A and 1V feeding pairs (>70 μm in diameter). The dependence of the axial thermal equilibration length on the local blood flow rate was demonstrated. Increasing the blood flow rate also produced a higher inlet temperature at the proximal boundary. This increase in blood flow rate, due to the decrease in the flow resistance in the 3A and 4A vessels, enables much warmer blood to be carried into the tissue preparation. The experimental technique presented in chapter 3 provides high spatial resolution temperature measurements on a length scale of the diameter of the thermally significant microvessels. This non-invasive experimental approach can be used in the future to quantitatively study the effect of blood flow on local heat exchange in other tissue preparations and to test the validity of the assumptions in various bioheat equations.

The modified theoretical model developed in chapter 3 has shown that to obtain detailed agreement with the experiments one must include axial conduction in the tissue and the supporting glass slide. The important simplifying assumptions in the modified theoretical model in chapter 3 are (i) uniform axial conduction in the tissue and the glass plate in the cross-sectional plane and (ii) uniform axial temperature gradients in the vessel cross-

sections. These simplifications enable us to separate variables and to solve the boundary value problem in the cross-sectional plane independent of that in the axial direction. The results show that the axial thermal equilibration will be accurately modeled provided the model considers the global effect of axial conduction in both the tissue and the glass supporting plate. Since the modified model in chapter 3 is valid for all Peclet numbers, it also predicts the blood vessel size and Peclet number for which there is a transition from axial conduction to countercurrent convection as the dominant model of axial energy exchange. Axial conduction and countercurrent blood flow are found to be of comparable importance and each mechanism contributes almost equally to the heat exchange when $1<\rho_m^*Pe<3$ mm. This transition range occurs in blood vessels that lie between 160 and 240 μm diameter for normal flow conditions in the rat cremaster and cat mesentery preparations.

Note that the theoretical models presented in chapters 2 and 3 are exact when the ratio of blood to tissue conductivity, K', is unity. In real applications in muscle tissue, this condition is well satisfied since tissue conductivity does not deviate significantly from that of the blood. Even when the ratio of blood to tissue conductivity is not unity, the solution is shown to be a highly accurate approximation compared with a complicated exact solution which is valid for all values of K'. The theoretical models can be generalized to consider any number of vessels in an embedded medium of more general cross-sectional geometry. One may derive a more general conduction shape factor in a cross-sectional plane of arbitrary geometry for the countercurrent heat exchange between the major paired vessels provided that a Green's function can be derived for the cross-sectional geometry. With minor modification the method of solution can be applied to the case where axial bleed off as well

as the axial variation of the vessel cross-sectional geometry and the embedding medium are taken into consideration. Therefore, it should be possible to obtain a general close form expression for the relationship between the local blood perfusion and the local arterial-venous temperature difference. Currently, it is assumed that the local perfusion source term in the Pennes equation is proportional to the local artery-tissue temperature difference since the venous return temperature is unknown.

The hyperthermic response of individual microvessels in skeletal muscle tissue subject to local heating has been investigated in chapter 4. Several important parameters, such as vessel number density, diameter, blood flow in several successive generations of blood vessels and the hyperthermic response of individual microvessels in rat cremaster muscle were measured directly. The measurements for the direct temperature response demonstrate that this direct response is only about one third of the maximal flow response that can be achieved in rat cremaster muscle. The local volume flow increase due to local heating is achieved by the decrease of microvascular resistance in the cremaster muscle due primarily to the dilation of 4A arterioles. It is still unknown whether 4A arterioles exhibit a similar dilation in other tissues. In measuring the direct temperature response, the adrenergic receptors were blocked by drugs so that the hyperemic response must be primarily due to the temperature influence on the vascular smooth muscle or endothelium. However, we did not completely separate the direct effect and the indirect effect in our experiments because of the effect of endothelium and other unblocked receptors. This separation of effects is possible only in isolated vessels. Using the techniques for studying isolated microvessels, one may study the direct temperature effect on the vascular smooth muscle using isolated

microvessels to gain a better understanding of the effect of local heating and cooling on each successive generation of the microvascular network. Similar experiments can also be conducted to examine the temperature effect on the receptor-mediated vasomotor pathways as well as the nitroprusside activated pathways that are associated with endothelial regulation. These temperature effects are required to construct a theory for the vasomotor regulation of local tissue heat transfer.

The observed changes in vascular diameter and flow due to local heating are also combined with the Weinbaum-Jiji equation to predict the enhancement in thermal conductivity due to local blood perfusion and to establish the limits of validity of the Weinbaum-Jiji theory in chapter 4. The Weinbaum-Jiji theory predicts that countercurrent blood flow in blood vessels less than 75 μm diameter does not significantly contribute to k_{eff}/k_t whereas a 2.5-fold increase in k_{eff} can be achieved for a maximally dilated 200 μm diameter 1A vessel pair in cremaster muscle and a 6-fold increase is predicted for maximally dilated 200 μm diameter vessels in the cat mesentery. However, in our study we have only measured the velocity in vessels that lie in the range 10-80 μm diameter due to the limitations of the rat size and the optical Doppler velocimeter. This range of measurement is too low to accurately extrapolate the data to vessels up to 200 μm diameter. To more directly and effectively study the countercurrent heat exchange between paired arteries and veins, it is better to select other muscle tissues, such as spinotrapezius muscle, where the major feeding vessels are significantly larger and are more representative than the cremaster muscle of the other skeletal muscle tissues in the body. For future study, the experiments can be designed to cover the entire range of Peclet numbers from 1 to 50 where the theory

predicts that the primary mechanism for tissue heat transfer changes from nearly pure conduction to a greatly enhanced conductivity due to countercurrent convective energy exchange.

Our experimental and theoretical results indicate that the Weinbaum-Jiji expression for k_{eff} is valid in cremaster muscle and cat mesentery tissue for both normal and hyperthermic conditions provided the largest blood vessels are <200 μm in diameter. However, during heavy exercise, the muscle blood flow can increase 50 to 100 fold. Therefore, this theory is not valid for predicting the enhancement in conductivity for vessels > 200 μm diameter during heavy exercise, since the thermal equilibration length L^* will not be short compared with the vessel length L^*_{length}. For larger vessels where $L^*/L^*_{length} \geq 1$, the perfusion contribution to k_{eff} may eventually approach a Pennes type enhancement proportional to the first power rather than the second power of the flow rate as described by the Weinbaum-Jiji theory. It is known that for skeletal muscle, such as rat cremaster muscle, nearly all vessels > 50 μm diameter occur as closely spaced countercurrent pairs. However, other tissues, such as the kidney cortex and tumors, do not have a dominant countercurrent architecture. Therefore, a more general model for various tissues under all possible conditions still needs to be developed to elucidate the blood perfusion contribution to the enhancement in conductivity.

In conclusion, the present research has led to a better understanding of the importance of countercurrent blood flow at the microvascular level in tissue-vessel heat exchange. It has demonstrated the flow conditions and vessel sizes where microvascular heat transfer occurs and predicted the relative contribution of tissue conduction and countercurrent blood

flow to local heat exchange. The theoretical and experimental study has provided a much more accurate description of the temperature profiles and the heat transfer mechanisms in tissue preparations than previous studies.

Appendix 1

In this Appendix we shall derive the Green's function W(x,y:ξ,η) for a line source at x=ξ, y=η that is described by the Eq.2.14 and 2.33 in chapter 2. The governing equation and boundary conditions for W are the following:

$$\begin{aligned} &\nabla^2 W(x,y:\xi,\eta) = \delta(x-\xi)\delta(y-\eta) \\ &y=H_1, \qquad \partial W/\partial y = -Bi_1 W \\ &y=-H_2, \qquad \partial W/\partial y = Bi_2 W \\ &x=\pm D, \qquad \partial W/\partial x = 0 \end{aligned}$$

We assume that W(x,y:ξ,η) can be written in the separable form,

$$W(x,y:\xi,\eta) = \sum_{n=0}^{\infty} X_n(x) Y_n(y:\xi,\eta) \tag{A.1}$$

where $X_n(x)$ satisfies

$$\begin{aligned} &\frac{d^2 X_n(x)}{dx^2} = -\lambda_n X_n(x) \\ &x=\pm D, \qquad \frac{dX_n(x)}{dx} = 0 \end{aligned} \tag{A.2}$$

The eigenfunction $X_n(x)$ is obtained as

$$\begin{aligned} &X_0(x) = 1, \qquad \lambda_0 = 0 \qquad n=0 \\ &X_n(x) = \cos[\sqrt{\lambda_n}(x-D)], \qquad \lambda_n = (n\pi/2D)^2, \; n=1,2,.....\infty \end{aligned} \tag{A.3}$$

Substituting (A.3) into (A.1), we obtain

$$\sum_{n=0}^{\infty} \left[\frac{d^2 Y_n(y:\xi,\eta)}{dy^2} - \lambda_n Y_n(y:\xi,\eta)\right] \cos[\sqrt{\lambda_n}(x-D)] = \delta(x-\xi)\delta(y-\eta) \tag{A.4}$$

Multiplying both sides of equation (A.4) by $\cos[\sqrt{\lambda_n}\,(x-D)]$ and integrating from $-D \le x \le D$, we obtain

$$\frac{d^2Y_0}{dy^2} = \frac{1}{2D}\delta(y-\eta) \qquad n=0 \qquad \text{(A.5)}$$

$$\frac{d^2Y_n}{dy^2} - \lambda_n Y_n = \frac{\cos[\sqrt{\lambda_n}(\xi-D)]}{D}\delta(y-\eta) \qquad n=1,2,3..... \qquad \text{(A.6)}$$

Equation (A.5) and its boundary condition can also be written as

$$\begin{aligned}
&\frac{d^2Y_0}{dy^2} = 0 && at \quad y \neq \eta \\
&\frac{dY_0}{dy}\Big|_{y=\eta^+} - \frac{dY_0}{dy}\Big|_{y=\eta^-} = \frac{1}{2D}, \quad Y_0|_{y=\eta^+} = Y_0|_{y=\eta^-} && \\
&\frac{dY_0}{dy} = -Bi_1 Y_0 && at \quad y = H_1 \\
&\frac{dY_0}{dy} = Bi_2 Y_0 && at \quad y = -H_2
\end{aligned} \qquad \text{(A.7)}$$

The solution of the boundary value problem (A.7) for Y_0 is

$$\begin{aligned}
Y_0(y:\xi,\eta) &= C_1 y + C_2 && \eta \le y \le H_1 \\
Y_0(y:\xi,\eta) &= D_1 y + D_2 && -H_2 \le y \le \eta
\end{aligned} \qquad \text{(A.8)}$$

where

$$C_1 = (\eta + H_2 + \frac{1}{Bi_2}) / [2D(H_1 + H_2 + \frac{1}{Bi_1} + \frac{1}{Bi_2})]$$

$$D_1 = (\eta - H_1 - \frac{1}{Bi_1}) / [2D(H_1 + H_2 + \frac{1}{Bi_1} + \frac{1}{Bi_2})]$$

$$C_2 = -C_1(H_1 + \frac{1}{Bi_1})$$

$$D_2 = D_1(H_2 + \frac{1}{Bi_2})$$

Similarly, the boundary value problem for Y_n in equation (A.6) can be written as

$$
\begin{aligned}
&\frac{d^2Y_n}{dy^2}-\lambda_n Y_n=0 && at\ y\neq\eta\\
&\frac{dY_n}{dy}\Big|_{y=\eta^+}-\frac{dY_n}{dy}\Big|_{y=\eta^-}=\frac{\cos[\sqrt{\lambda_n}(\xi-D)]}{D}, \quad Y_n|_{y=\eta^+}=Y_n|_{y=\eta^-} && \\
&\frac{dY_n}{dy}=-Bi_1Y_n && at\ y=H_1\\
&\frac{dY_n}{dy}=Bi_2Y_n && at\ y=-H2
\end{aligned}
\tag{A.9}
$$

The solution for Y_n is:

$$
\begin{aligned}
Y_n(y;\xi,\eta) &= \frac{\cos[\sqrt{\lambda_n}(\xi-D)]}{D}[A_1e^{\sqrt{\lambda_n}y}+B_1e^{-\sqrt{\lambda_n}y}] \quad y\geq\eta\\
Y_n(y;\xi,\eta) &= \frac{\cos[\sqrt{\lambda_n}(\xi-D)]}{D}[A_2e^{\sqrt{\lambda_n}y}+B_2e^{-\sqrt{\lambda_n}y}] \quad y<\eta
\end{aligned}
\tag{A.10}
$$

where

$$
\begin{aligned}
P_1 &= (\sqrt{\lambda_n}+Bi_1)/(\sqrt{\lambda_n}-Bi_1)\\
P_2 &= (\sqrt{\lambda_n}-Bi_2)/(\sqrt{\lambda_n}+Bi_2)\\
A_1 &= \frac{1}{2\sqrt{\lambda_n}}\frac{1+P_2e^{-\sqrt{\lambda_n}(2H_2+2\eta)}}{[-P_1+P_2e^{-\sqrt{\lambda_n}(2H_2+2H_1)}]}e^{-\sqrt{\lambda_n}(2H_1-\eta)}\\
B_1 &= \frac{1}{2\sqrt{\lambda_n}}\frac{1+P_2e^{-\sqrt{\lambda_n}(2H_2+2\eta)}}{[-P_1+P_2e^{-\sqrt{\lambda_n}(2H_2+2H_1)}]}P_1e^{\sqrt{\lambda_n}\eta}\\
A_2 &= \frac{1}{2\sqrt{\lambda_n}}\frac{P_1+e^{-\sqrt{\lambda_n}(2H_1-2\eta)}}{[-P_1+P_2e^{-\sqrt{\lambda_n}(2H_2+2H_1)}]}e^{\sqrt{\lambda_n}\eta}\\
B_2 &= \frac{1}{2\sqrt{\lambda_n}}\frac{P_1+e^{-\sqrt{\lambda_n}(2H_1-2\eta)}}{[-P_1+P_2e^{-\sqrt{\lambda_n}(2H_2+2H_1)}]}P_2e^{-\sqrt{\lambda_n}(2H_2+\eta)}
\end{aligned}
$$

Substituting (A.8) and (A.10) into (A.1), we obtain the following expressions for the Green's function $W(x,y;\xi,\eta)$, which are used in section 2.4.2,

$$W=(C_1y+C_2)+\sum_{n=1}^{\infty}\frac{1}{D}\cos[\sqrt{\lambda_n}(\xi-D)]\cos[\sqrt{\lambda_n}(x-D)][A_1e^{\sqrt{\lambda_n}y}+B_1e^{-\sqrt{\lambda_n}y}] \quad y\geq\eta$$
$$W=(D_1y+D_2)+\sum_{n=1}^{\infty}\frac{1}{D}\cos[\sqrt{\lambda_n}(\xi-D)]\cos[\sqrt{\lambda_n}(x-D)][A_2e^{\sqrt{\lambda_n}y}+b_2e^{-\sqrt{\lambda_n}y}] \quad y<\eta \qquad \text{(A.11)}$$

where (A.11) are Eqs.2.33a,b in chapter 2.

If the source is located at $\xi=\eta=0$, the expression for the Green's function simplifies to:

$$W=(C_1y+C_2)+\sum_{n=1}^{\infty}\frac{1}{D}\cos[\frac{n\pi}{2}]\cos[\sqrt{\lambda_n}(x-D)][A_1e^{\sqrt{\lambda_n}y}+B_1e^{-\sqrt{\lambda_n}y}] \quad y\geq0$$
$$W=(D_1y+D_2)+\sum_{n=1}^{\infty}\frac{1}{D}\cos[\frac{n\pi}{2}]\cos[\sqrt{\lambda_n}(x-D)][A_2e^{\sqrt{\lambda_n}y}+B_2e^{-\sqrt{\lambda_n}y}] \quad y<0 \qquad \text{(A.12)}$$

(A.12) are Eqs.2.14a, b in chapter 2.

Appendix 2

In this Appendix we shall show that Eq.2.19 is valid only when the ratio K'=1. This proof rests on the use of Green's theorem.

If we decompose K' into two terms, 1 and K'-1, the left side of Eq.2.19 becomes

$$\frac{C_{sn}}{\pi}\int_{-\pi}^{\pi}[\frac{W(\rho_s,\phi_s:0,0)}{\rho_s^j}\ \frac{\partial W(\rho_s,\phi_s:0,0)}{\partial\rho_s}\ \frac{}{j\rho_s^{j-1}}]\cos(j\phi_s)|_{\rho_s=1}d\phi_s\ \frac{(K'\ 1)C_{sn}}{\pi}\int_{-\pi}^{\pi}W(\rho_s,\phi_s:0,0)\frac{\cos(j\phi_s)}{\rho_s^j}|_{\rho_s=1}d\phi_s \qquad \text{(A.13)}$$

The first integral in Eq.A.13 can also be written as

$$\frac{C_{sn}}{\pi}\oint_\Gamma[\rho_s^{j-1}\cos(j\phi_s)W(\rho_s,\phi_s:0,0)-\frac{\rho_s^j}{j}\cos(j\phi_s)\frac{\partial W(\rho_s,\phi_s:0,0)}{\partial\rho_s}]|_{\rho_s=1}d\Gamma, \qquad \text{(A.14)}$$

where Γ is the vessel surface $\rho_s=1$. Considering that $\partial[\rho_s^j\cos(j\phi_s)/j]/\partial\rho_s=\rho_s^{j-1}\cos(j\phi_s)$ and applying Green's theorem to expression (A.14), one obtains

$$\int\int_{\Omega}\{W(\rho_s,\phi_s:0,0)\nabla^2[\cos(j\phi_s)\rho_s^j/J]-\cos(j\phi_s)\rho_s^j/J\nabla^2 W(\rho_s,\phi_s:0,0)\}d\Omega$$

$$=\int\int_{\Omega}\{-[\cos(j\phi_s)\rho_s^j/J]\nabla^2 W(\rho_s,\phi_s:0,0)\}d\Omega \qquad \text{(A.15)}$$

where Ω refers to the region inside the vessel. Since the Green's function $W(\rho_s,\phi_s:0,0)$ satisfies Laplace's equation, within Γ except at the source point, expression (A.15) reduces to

$$[\cos(j\phi_s)\rho_s^j/J]|_{\rho_s=0}=0$$

The above derivation shows that the first integral in (A.13) vanishes for any j. The second integral of in (A.13) is the integral of the Green's function multiplied by the weighing function $\cos(j\phi_s)$. This integral is equal to zero for any j only if the Green's function is a constant, which is not the case. Only when $K'=1$ does this second term vanish for any j. Since the left side of Eq.2.19 and (A.13) are equivalent, Eq.2.19 is valid for all j only when K'=1.

Appendix 3

Coefficients in Eqs.2.21, 2.22, and 2.23

$$A_{11}=Pe(-\frac{11}{96}+\frac{K'\pi}{2}\overline{W}_{s-s})$$

$$A_{12}=PeK'\pi\rho_w^2\overline{u}\,\overline{W}_{v-s}/2$$

$$A_{13}=\pi\overline{W}_{s-s}+\pi\rho_w^2\overline{W}_{v-s}-(\frac{\eta_s^2}{2}+I_1\eta_s+I_2)-\frac{1}{4}$$

$$A_{21}=PeK'\pi\,\overline{W}_{s-v}/2$$

$$A_{22} = Pe\left(-\frac{11}{96}\rho_w^2\bar{u} + \frac{K'\pi\rho_w^2\bar{u}}{2}\overline{W}_{v-v}\right)$$

$$A_{23} = \pi\overline{W}_{a-v} + \pi\rho_w^2\overline{W}_{v-v} - \left(\frac{\eta_v^2}{2} + I_1\eta_v + I_2\right) - \frac{\rho_w^2}{4}$$

$$A_{31} = \frac{PeK'\pi}{2}\overline{W}_{a-t}$$

$$A_{32} = \frac{PeK'\pi\rho_w^2\bar{u}}{2}\overline{W}_{v-t}$$

$$A_{33} = \pi\overline{W}_{a-t} + \pi\rho_w^2\overline{W}_{v-t} + \left\{-2D\left[\frac{H_1^3+H_2^3}{6} + \frac{I_1(H_1^2-H_2^2)}{2} + I_2(H_1+H_2)\right]\right.$$

$$\left. + \pi\left(\frac{\eta_a^2}{2} + I_1\eta_a + I_2\right) + \frac{\pi}{8} + \rho_w^2\pi\left(\frac{\eta_v^2}{2} + I_1\eta_v + I_2\right) + \frac{\rho_w^4\pi}{8}\right\} / \left[2D(H_1+H_2) - \pi - \pi\rho_w^2\right]$$

where,

$$\overline{W}_{a-a} = \frac{1}{2\pi}\int_{-\pi}^{\pi} W(x,y:\xi_a,\eta_a)\big|_{\rho_a=1}\, d\phi_a$$

$$\overline{W}_{v-a} = \frac{1}{2\pi}\int_{-\pi}^{\pi} W(x,y:\xi_v,\eta_v)\big|_{\rho_a=1}\, d\phi_a$$

$$\overline{W}_{a-v} = \frac{1}{2\pi}\int_{-\pi}^{\pi} W(x,y:\xi_a,\eta_a)\big|_{\rho_v=\rho_w}\, d\phi_v$$

$$\overline{W}_{v-v} = \frac{1}{2\pi}\int_{-\pi}^{\pi} W(x,y:\xi_v,\eta_v)\big|_{\rho_v=\rho_w}\, d\phi_v$$

$$\overline{W}_{a-t} = \frac{1}{\left[2D(H_1+H_2) - \pi - \pi\rho_w^2\right]} \iint_{tissue\,region} W(x,y:\xi_a,\eta_a)\, d\Omega$$

$$\overline{W}_{v-t} = \frac{1}{\left[2D(H_1+H_2) - \pi - \pi\rho_w^2\right]} \iint_{tissue\,region} W(x,y:\xi_v,\eta_v)\, d\Omega$$

Table 1 Key parameters

Thermal Properties	Geometric Properties
γ_f = 1000 kg/m^3	ρ_w^* = 40-75 μm
C_f = 4180 J/kg.^{0}C	ρ_m^* = 40-125 μm
$k_f = k_t$ = 0.6 W/m.^{0}C	H^* = 100-400 μm
k_s = 1.4 W/m.^{0}C	H_s^* = 200 μm
h = 5-25 W/m^2.^{0}C	D^* = 50 mm
	Pe = 1-15

Table 2. Average values of diameter, velocity and flow for different vessel types at 34℃.

Vessel Type	1A arteriole n_a=8	2A arteriole n_a=9	3A arteriole n_a=11	4A arteriole n_a=8
Diameter $2\rho_{ar}^*$ (μm)	60.2±7.8	44.4±11.2	26.9±6.9	10.7±2.5
Centerline red cell velocity V (mm s^{-1})	24.2±6.9	16.2±4.6	14.8±6.6	4.8±1.4
Flow Q (nl s^{-1})	43.0	15.6	5.23	0.27
$Q/(2\rho_{ar}^*)^3$	1.98×10^{-4}	1.79×10^{-4}	2.69×10^{-4}	2.23×10^{-4}

Table 3. Average values of diameter, velocity and flow in maximum dilation.

Vessel Type	1A arteriole n_a=8	2A arteriole n_a=9	3A arteriole n_a=11	4A arteriole n_a=8
Diameter $2\rho_{ar}^*$ (μm)	74.3	53.3	37.8	18.0
Centerline red cell velocity V (mm s^{-1})	33.4	24.8	21.7	8.3
Flow Q (nl s^{-1})	90.3	34.6	15.2	1.32
$Q/(2\rho_{ar}^*)^3$	2.21×10^{-4}	2.28×10^{-4}	2.82×10^{-4}	2.27×10^{-4}

Table 4. Anatomic parameters of rat cremaster muscle for 1A, 2A and 3A vessels

Muscle	Vessel	L^*_{length} (mm)	$L^*_{length}/A_{surface}$ (mm/mm^2)	N	Vessel diameter $2\rho_{av}{}^*$ (μm)	L^* (mm)	n (no. mm^{-2})
1	1A	10.7	0.164	2	110.0	5.37	0.548
	2A	17.3	0.266	5	80.0	3.46	0.886
	3A	37.0	0.567	23	30.0	1.61	1.895
2	1A	9.9	0.073	1	160.0	9.90	0.183
	2A	20.7	0.152	5	115.0	4.13	0.380
	3A	35.3	0.260	12	65.0	2.94	0.650
3	1A	12.0	0.086	1	187.0	12.0	0.215
	2A	20.3	0.145	4	125.0	5.03	0.363
	3A	42.7	0.305	14	75.0	3.05	0.763
4	1A	24.2	0.082	2	143.0	12.1	0.205
	2A	51.0	0.172	10	118.0	5.10	0.430
	3A	78.5	0.265	26	72.0	3.02	0.663
5	1A	11.0	0.074	1	168.0	11.0	0.185
	2A	20.0	0.134	6	106.0	3.33	0.335
	3A	28.7	0.193	11	50.0	2.61	0.475

Table 5. Effective thermal conductivity for various vessel generations at 34 °C

	Vessel diameter $2\rho_{ar}^*$ (μm)	Centerline red cell velocity V (mm s^{-1})	L^*_{length} (mm)	n (no. mm^{-2})	Pe	L^*/L^*_{length}	$n\rho_{ar}^{*2}Pe^2$	k_{eff}/k_t
1A	60.2	24.2	2.71	0.76	5.16	0.017	1.84×10^{-2}	1.010
2A	44.4	16.2	1.92	1.09	2.54	0.009	3.46×10^{-3}	1.001
3A	26.9	14.8	1.08	1.97	1.41	0.006	7.01×10^{-4}	~1.0
4A	10.7	4.8	0.37	5.85	0.18	0.0008	5.51×10^{-6}	~1.0

Table 6. Effective thermal conductivity for various vessel generations at maximum dilation

	Vessel diameter $2\rho_{ar}^*$ (μm)	Centerline red cell velocity V (mm s^{-1})	L^*_{length} (mm)	n (no. mm^{-2})	Pe	L^*/L^*_{length}	$n\rho_{ar}^{*2}Pe^2$	k_{eff}/k_t
1A	74.3	33.40	2.71	0.76	8.78	0.038	8.10×10^{-2}	1.05
2A	53.3	24.78	1.92	1.09	4.68	0.023	1.69×10^{-2}	1.01
3A	37.8	21.71	1.08	1.97	2.90	0.017	5.91×10^{-3}	~1.0
4A	17.8	8.29	0.37	5.85	0.52	0.005	1.31×10^{-4}	~1.0

Table 7. ϵ and k_{eff}/k_t for vessels > 80 μm dia. in normal state

Vessel Diameter $2\rho_{av}^*$(μm)	Mean Velocity u (mm s^{-1})		Peclet Number Pe		L^* (mm)		L^*_{length} (mm) Eq.4.6	n (no.mm^{-2}) Eq.4.6	$\epsilon = L^*/L^*_{length}$		k_{eff}/k_t	
	RCP	CMP	RCP	CMP	RCP	CMP			RCP	CMP	RCP	CMP
80	6.86	11.3	3.89	6.39	0.05	0.09	3.76	0.545	0.013	0.023	1.01	1.02
100	8.07	13.8	5.73	9.78	0.10	0.17	4.85	0.419	0.020	0.035	1.01	1.08
120	9.23	16.3	7.86	13.9	0.17	0.29	5.98	0.337	0.028	0.048	1.05	1.18
150	10.9	19.9	11.6	21.2	0.30	0.55	7.72	0.259	0.039	0.071	1.09	1.31
200	13.4	25.9	19.0	36.7	0.66	1.27	10.7	0.185	0.061	0.119	1.32	2.20

* RCP: rat cremaster preparation. CMP: cat mesentery preparation.

Table 8. Local volume flow increase due to local heating

Ratio of volume flow in local heating to that in normal state, Q_l/Q_n	1A	2A	3A	4A	Average values from 1A and 2A vessels
direct temperature response	1.25	1.47	1.50	2.25	1.36
maximum dilation	2.10	2.21	2.90	4.88	2.16

Table 9. ϵ and k_{eff}/k_t for vessels > 80 μm dia. due to local heating

Vessel Dia. $2\rho_{av}^*$ (μm)	$\rho_{av}^* Pe$(mm) direct thermal response		$\epsilon = L^*/L^*_{length}$ direct thermal response		$\rho_{av}^* Pe$ (mm) maximum dilation		$\epsilon = L^*/L^*_{length}$ maximum dilation		k_{eff}/k_t direct thermal response		k_{eff}/k_t maximum dilation	
	RCP	CMP	RCP	CMP	RCP	CMP	RCP	CMP	RCP	CMP	RCP	CMP
80	0.21	0.35	0.02	0.03	0.34	0.55	0.03	0.05	1.01	1.03	1.03	1.09
100	0.39	0.66	0.03	0.05	0.62	1.05	0.04	0.07	1.03	1.12	1.07	1.25
120	0.64	1.13	0.04	0.07	1.02	1.78	0.06	0.11	1.10	1.32	1.25	1.87
150	1.18	2.16	0.06	0.11	1.87	3.43	0.08	0.18	1.18	1.58	1.47	2.46
200	2.58	4.98	0.10	0.20	4.10	7.91	0.12	0.24	1.65	3.22	2.49	6.58

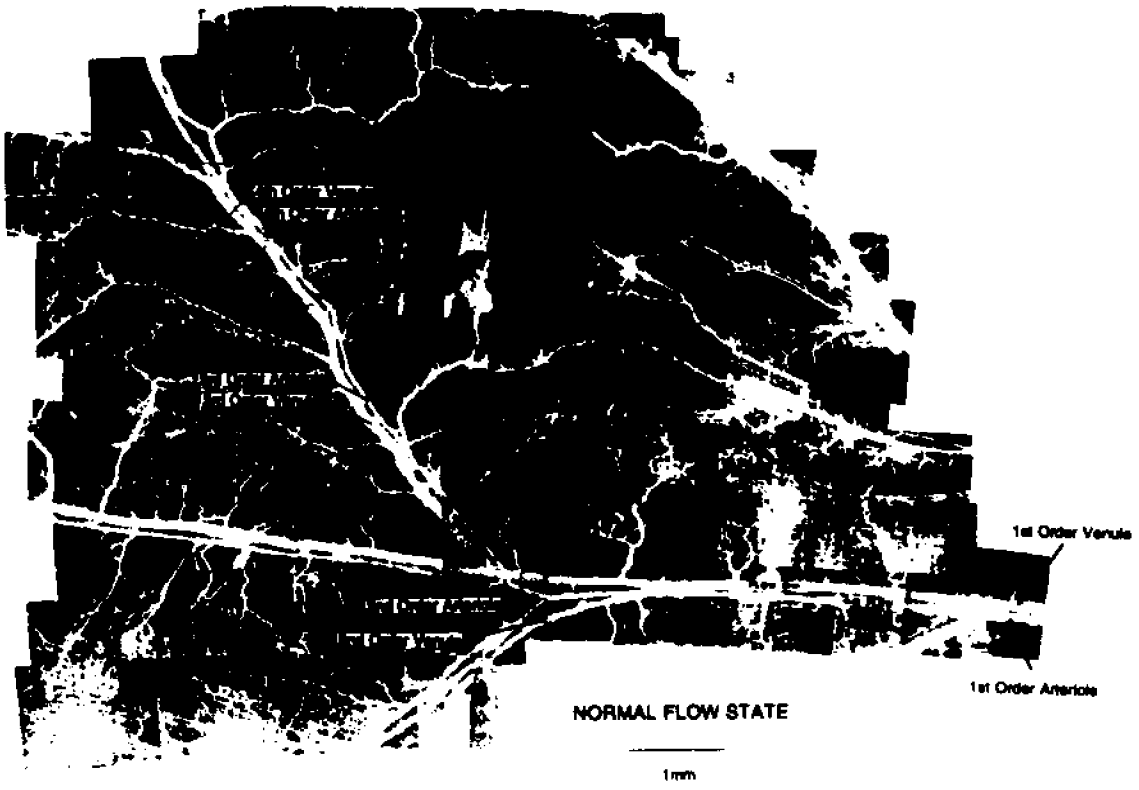

Figure 1. Photomontage of the rat cremaster preparation provided by Dr. H. H. Liposwky.

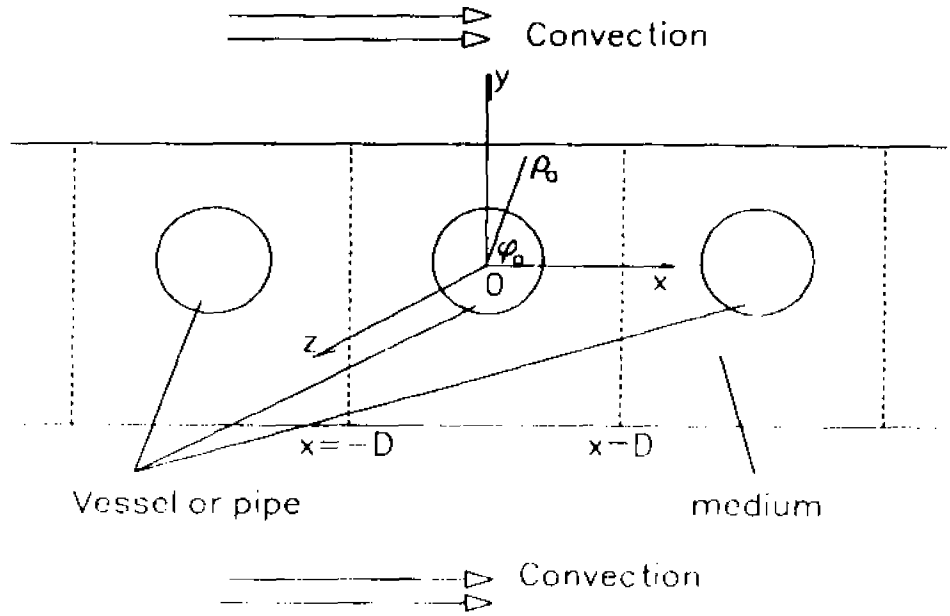

Figure 2. Schematic of vessels or pipes embedded in surrounding medium with surface convection.

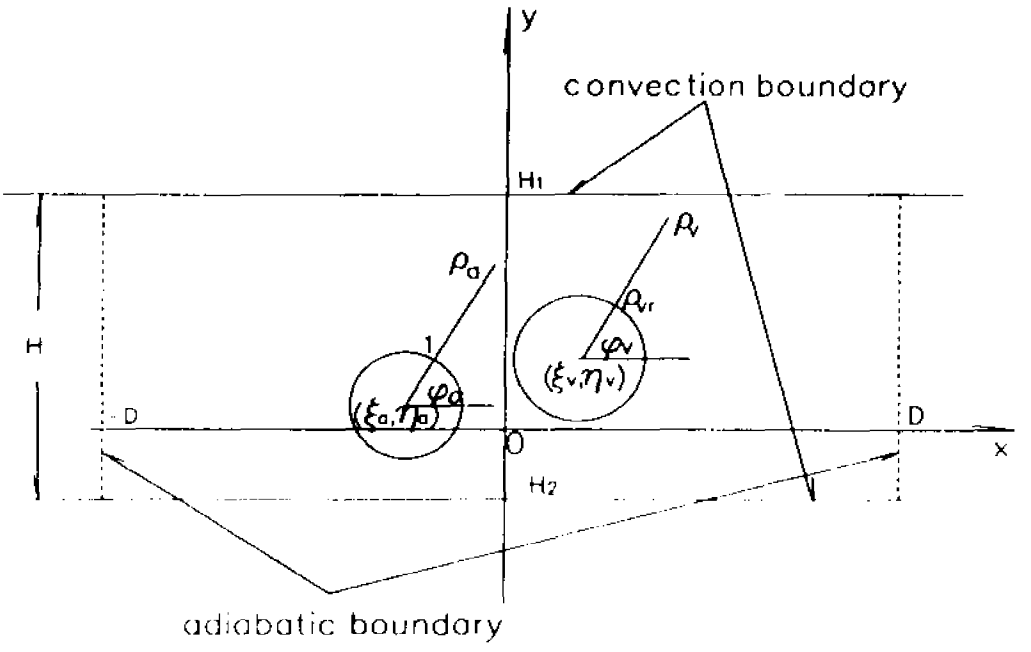

Figure 3. The geometry of the cross-sectional plane and coordinate system for two vessels.

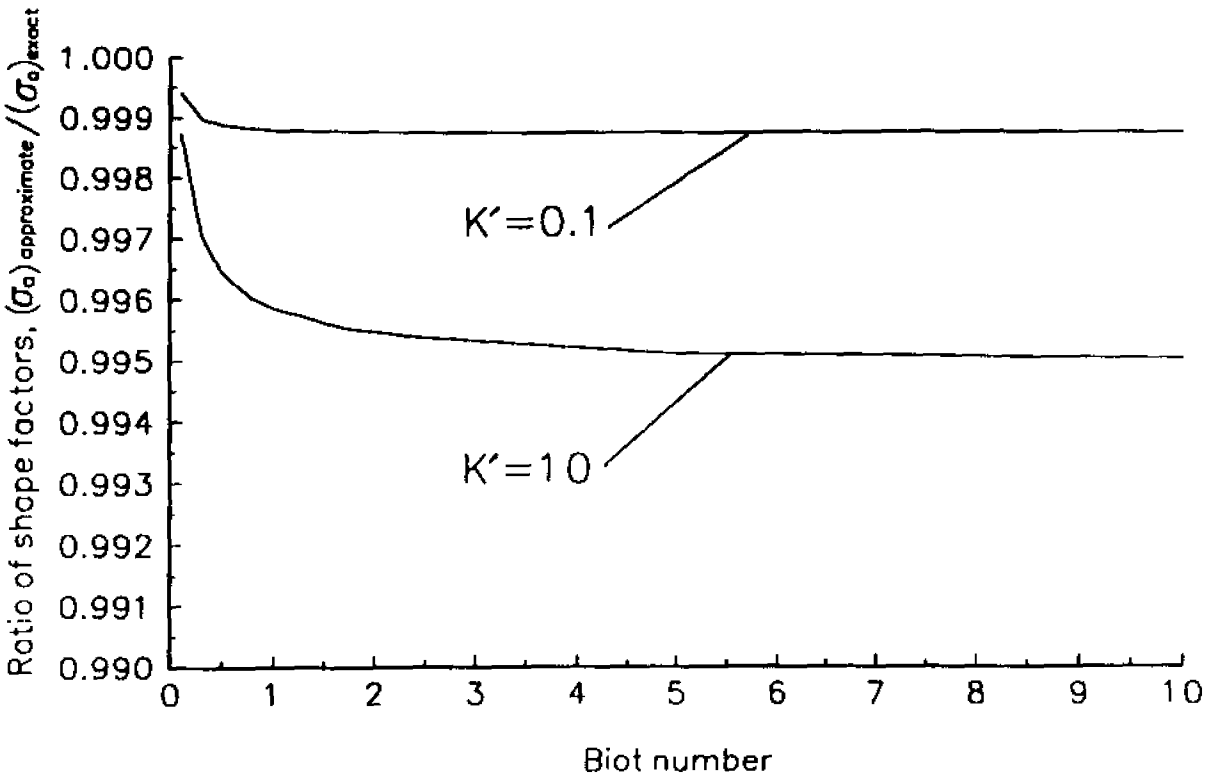

Figure 4. The effect of Biot number on the accuracy of the shape factor of single vessel using the approximate solution in section 2.3.1, where $(\sigma_o)_{exact}$ is the result from exact solution in section 2.3.2, for case $2D$=20 and H=8.

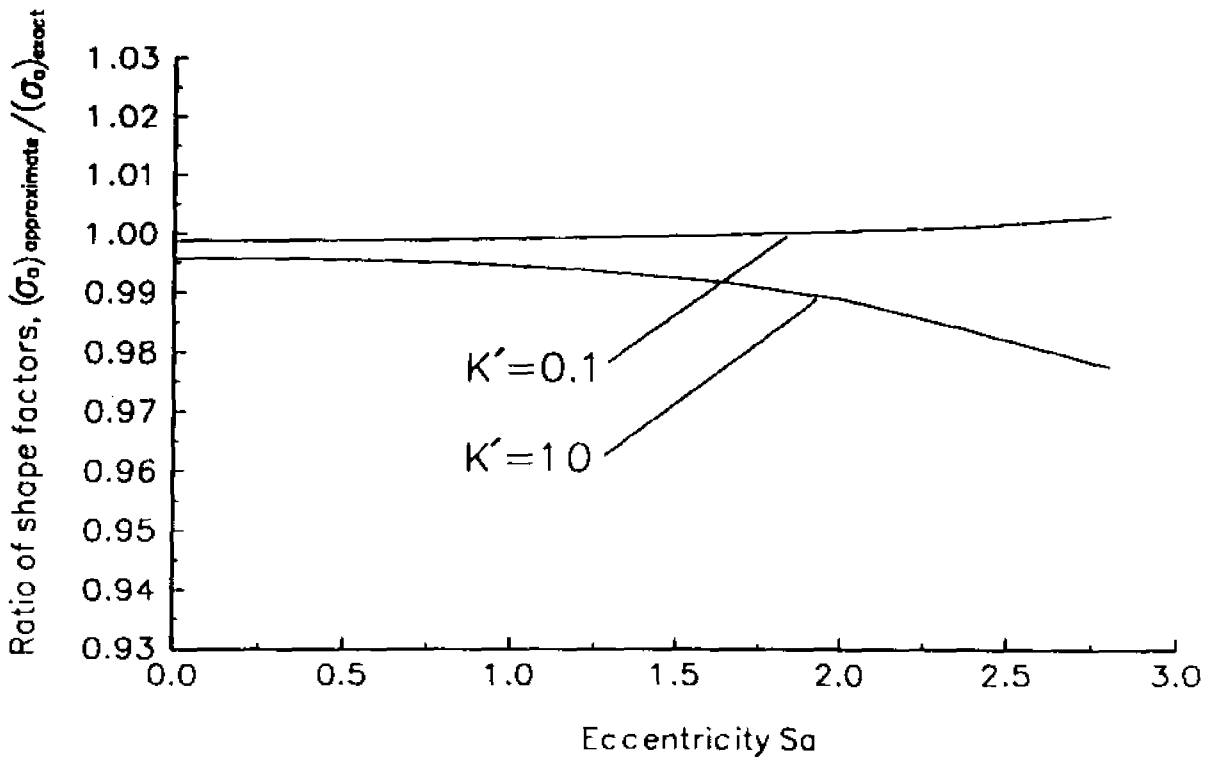

Figure 5. The effect of vessel eccentricity *Sa* on the accuracy of the shape factor for a single vessel using the approximate solution for the case $2D=20$, $Bi_1=Bi_2=1$ and $H=8$.

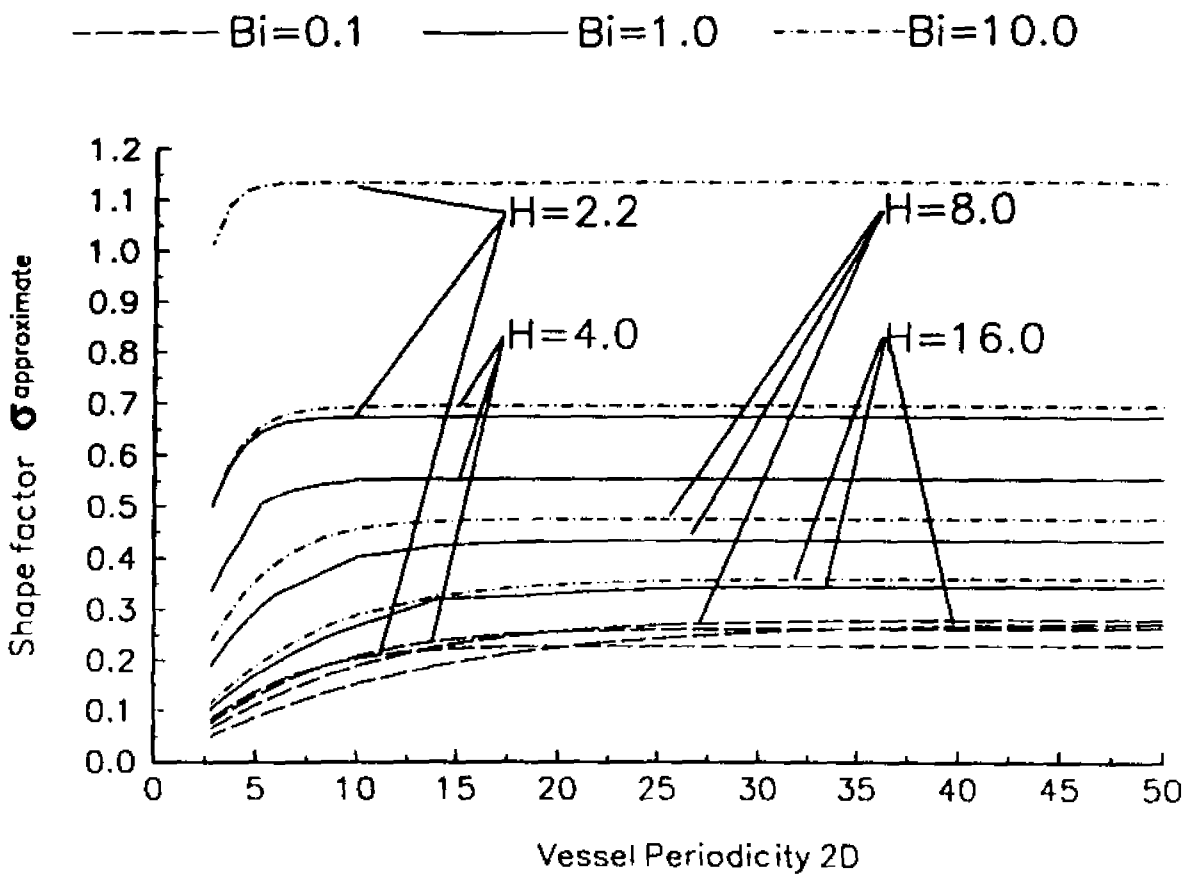

Figure 6. Shape factor of periodic array of single vessels as a function of vessel periodicity *2D* for various tissue thicknesses *H* and Biot numbers Bi. $H_1=H_2$.

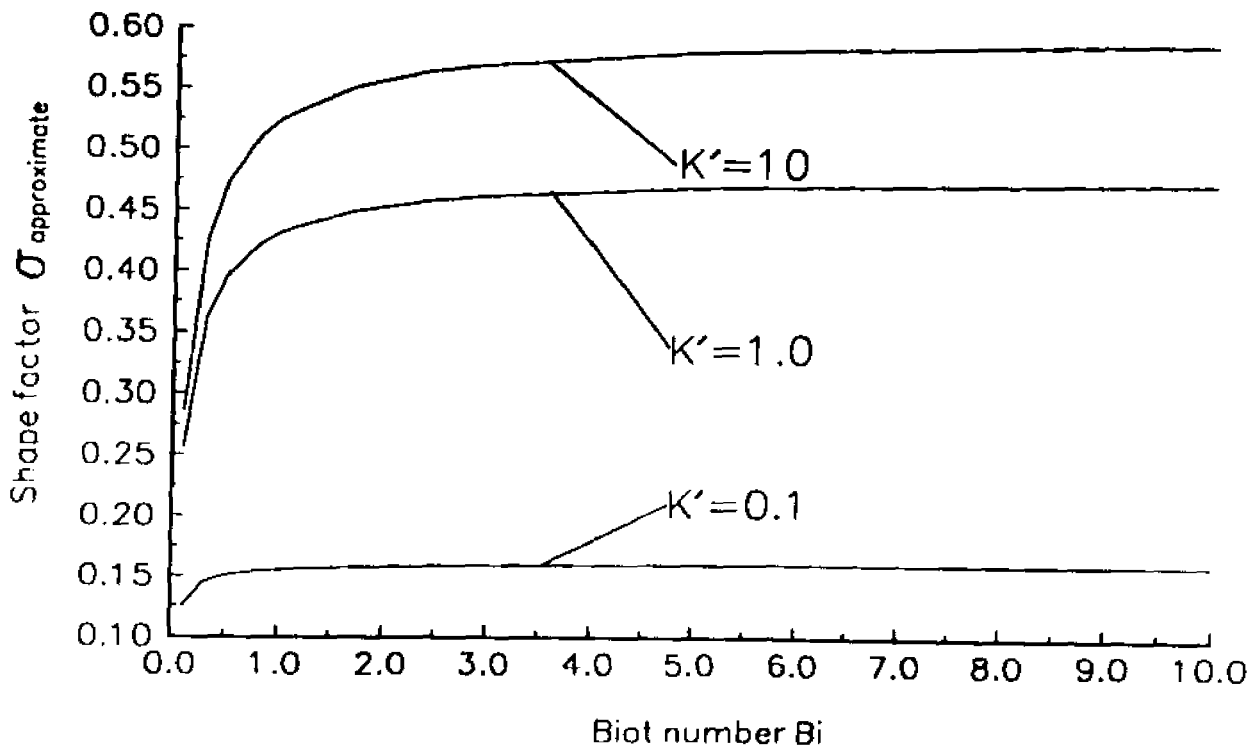

Figure 7. Shape factor for symmetrically located single vessel as a function of Bi for different K' for $2D=20$, $H=8$

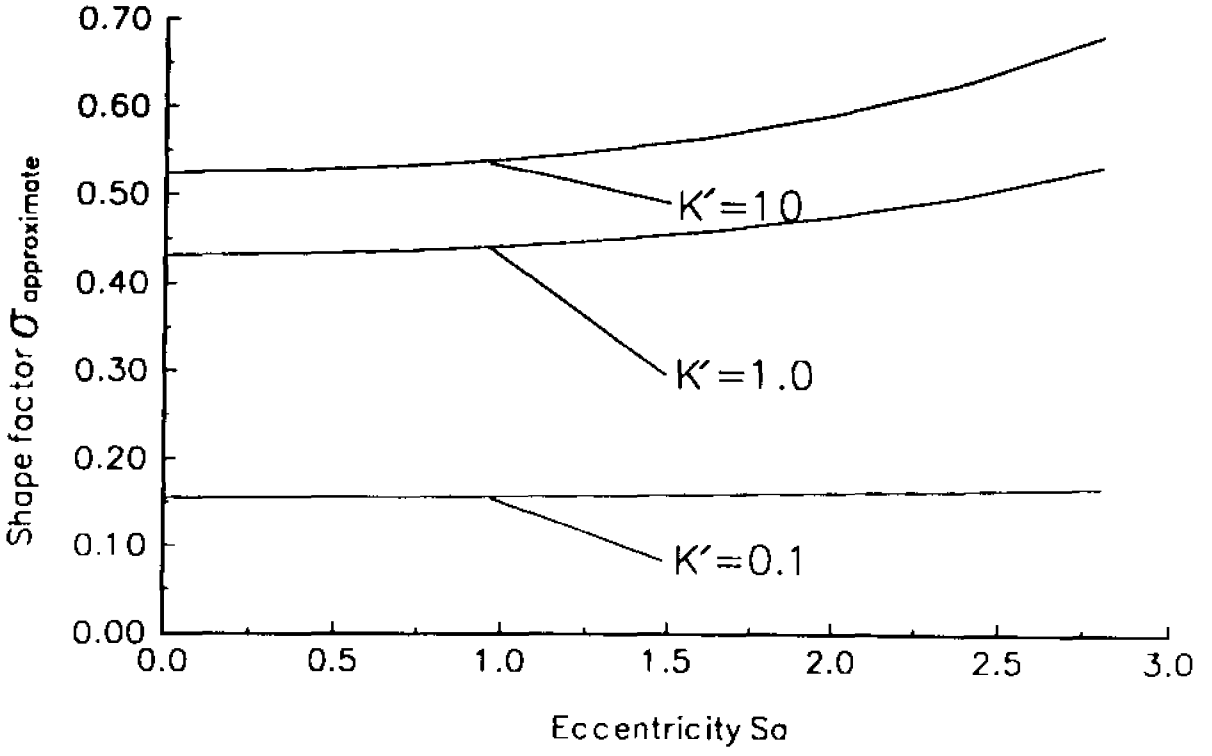

Figure 8. Shape factor of single vessel as a function for vessel eccentricity Sa for different K' for $2D$=20, H=8 and Bi_1=Bi_2=1.

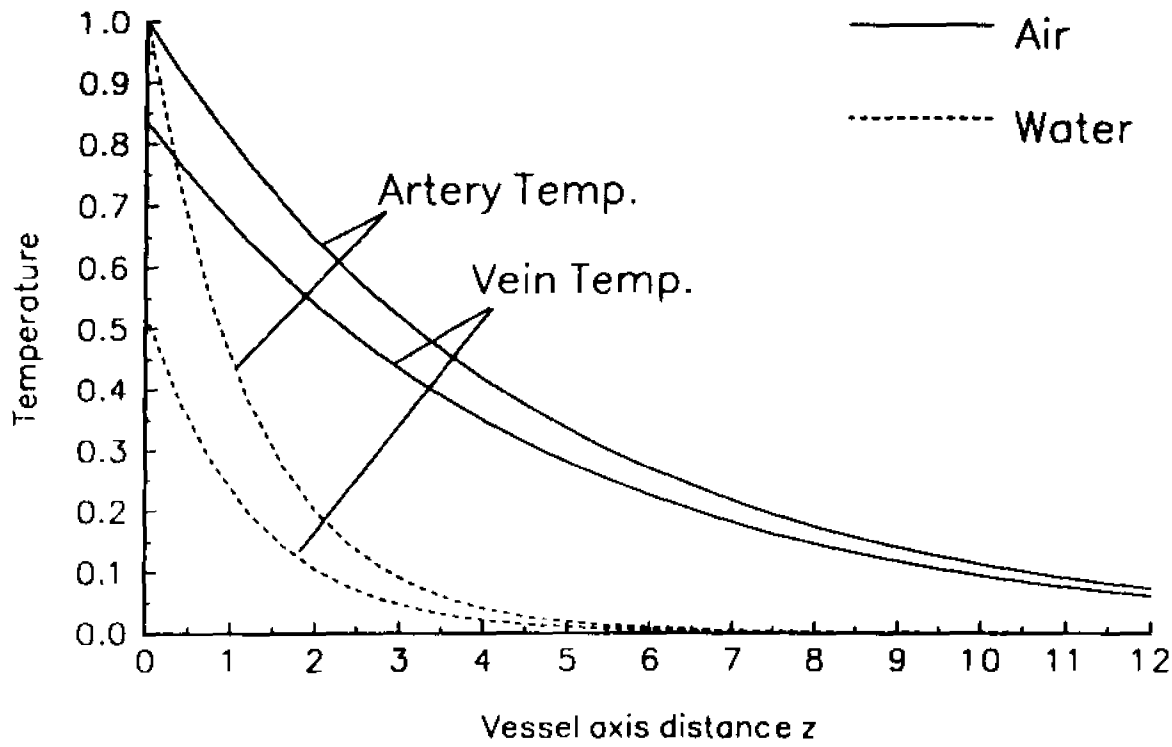

Figure 9. Temperature distribution along artery-vein axes in both air and water environments. $(\xi_a, \eta_a) = (-2, 0)$, $(\xi_v, \eta_v)=(1, 0)$, $\rho_w=1.6$ and $u_w=-1/1.6^2$.

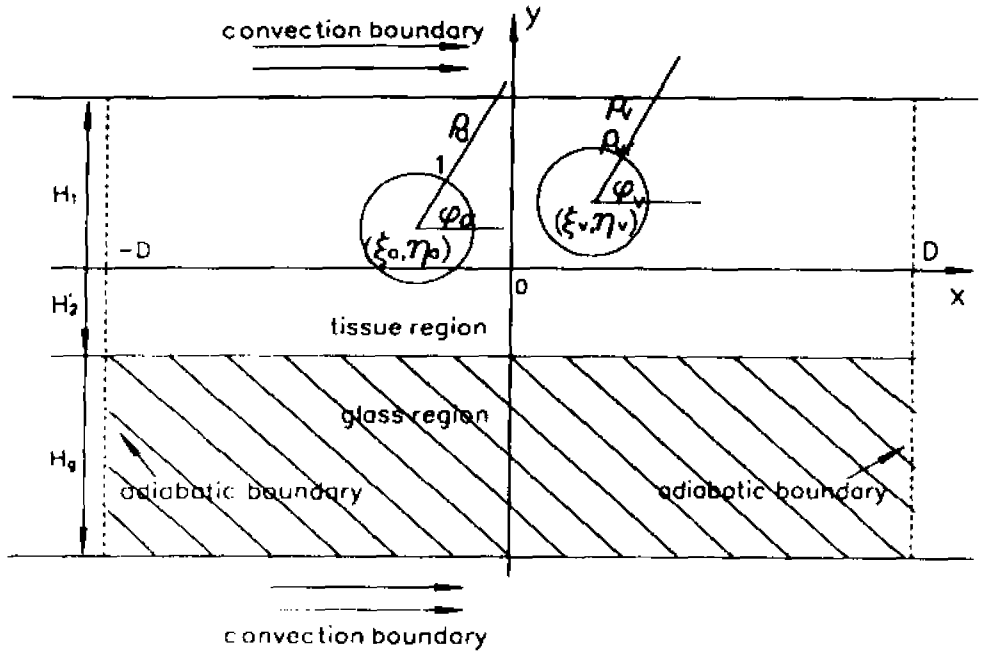

Figure 10. Schematic of the cross-sectional plane with the glass plate.

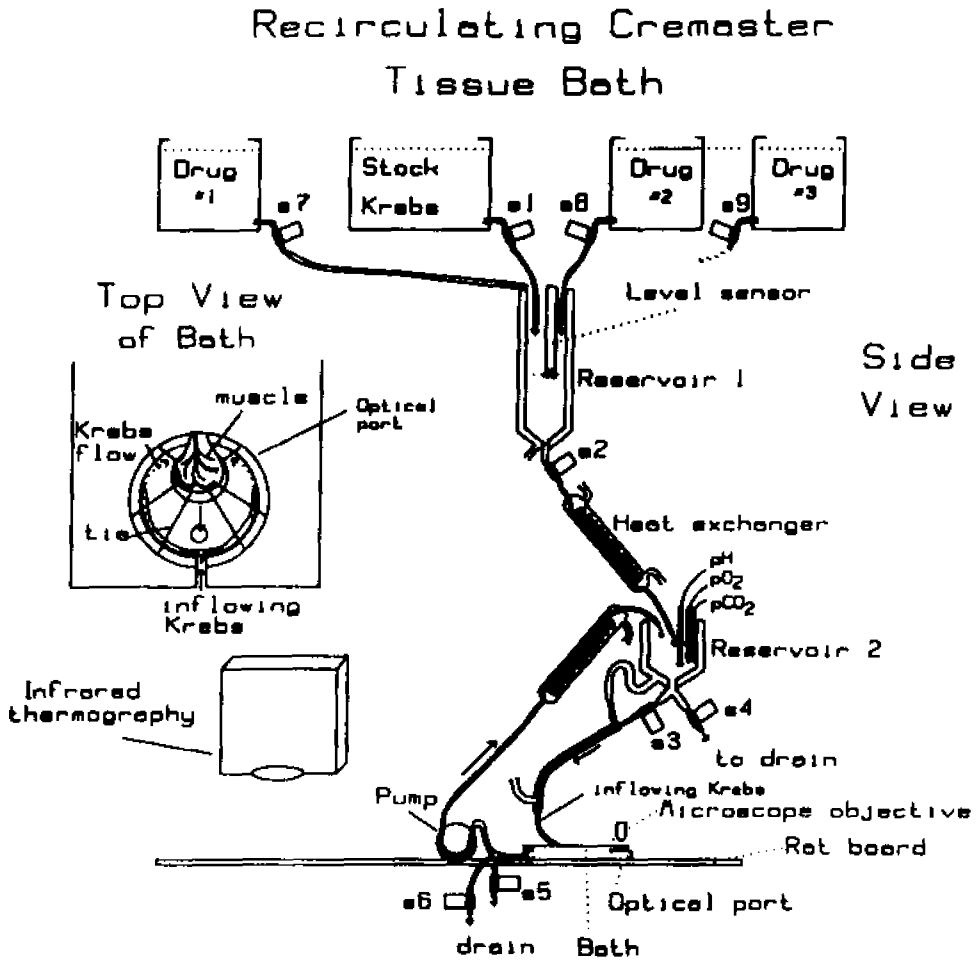

Figure 11. Schematic of the experimental setup used to study thermal equilibration in rat cremaster muscle preparation.

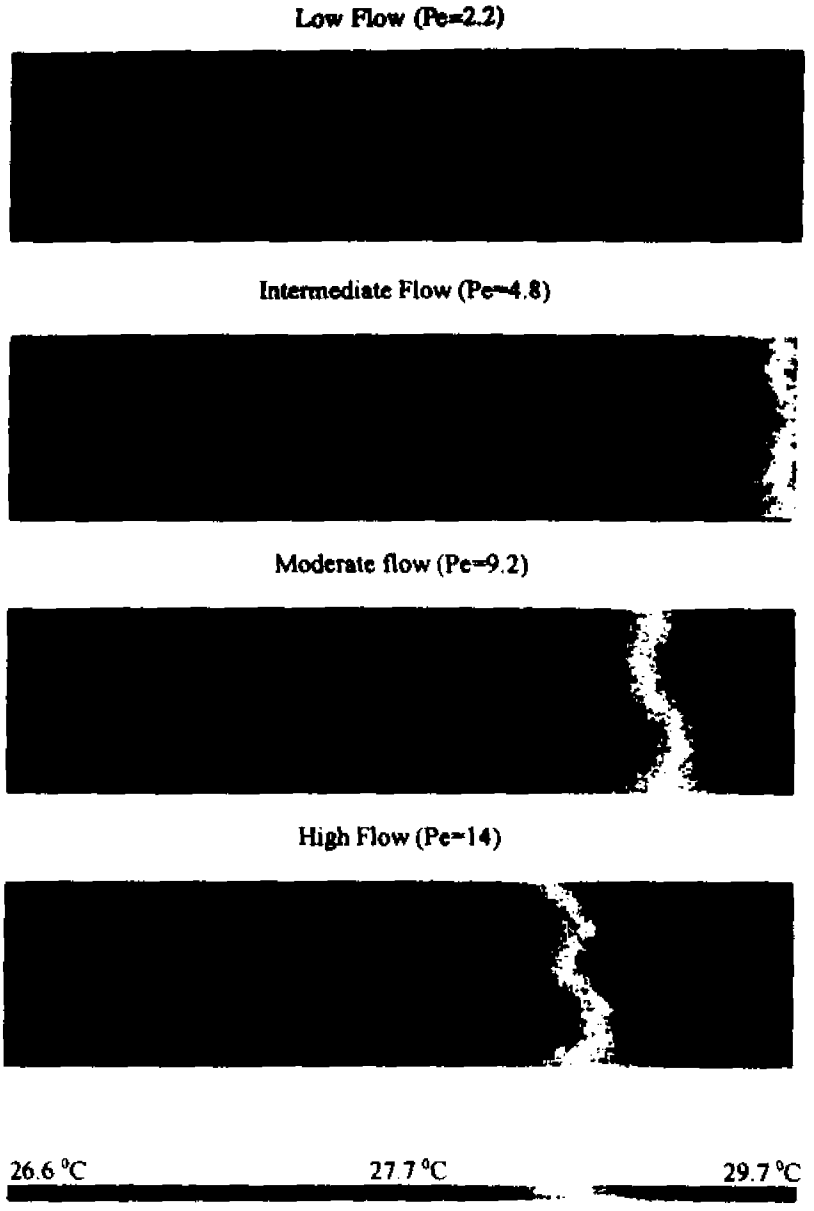

Figure 12. Thermal images of the cremaster muscle at four different levels of the Peclet number of the main 1A arteriole. The spectrum at the bottom shows the relationship of image color to temperature. The right side of each image is the proximal edge of the muscle.

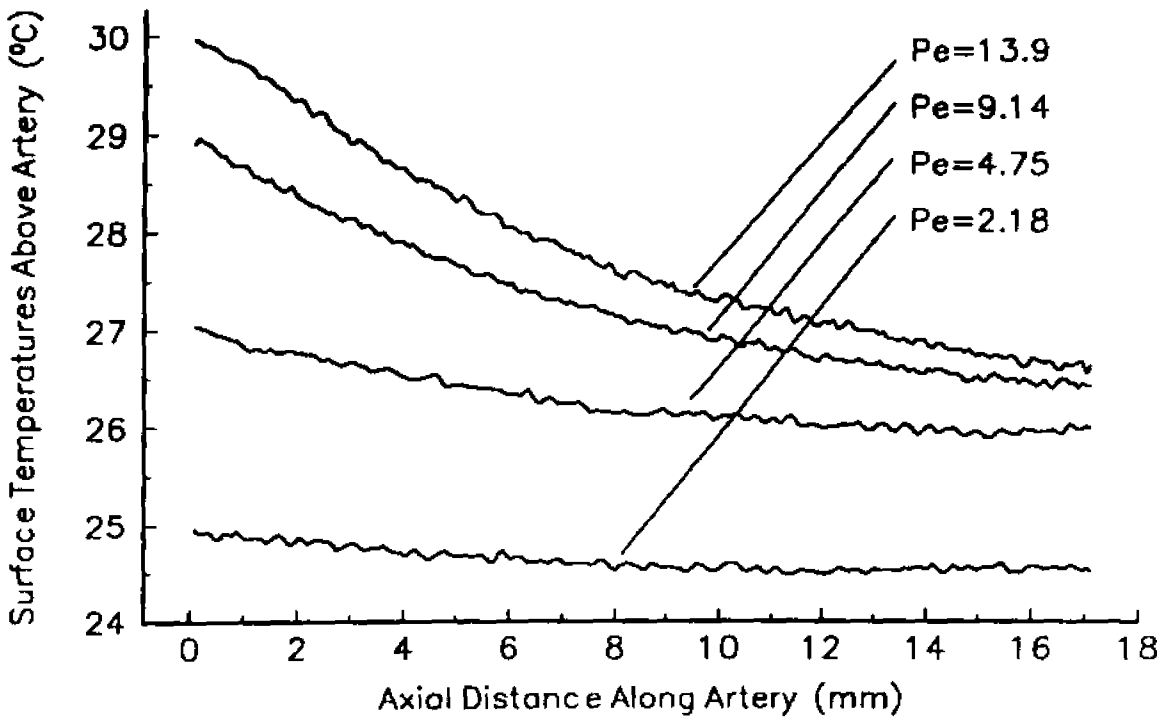

Figure 13. Temperature profiles along the central arteriole and venule of the cremaster at four different blood flow rates. z^*=0 mm is the proximal end of the artery as it enters the tissue bath and z^*=17 mm is the distal end of the recording area.

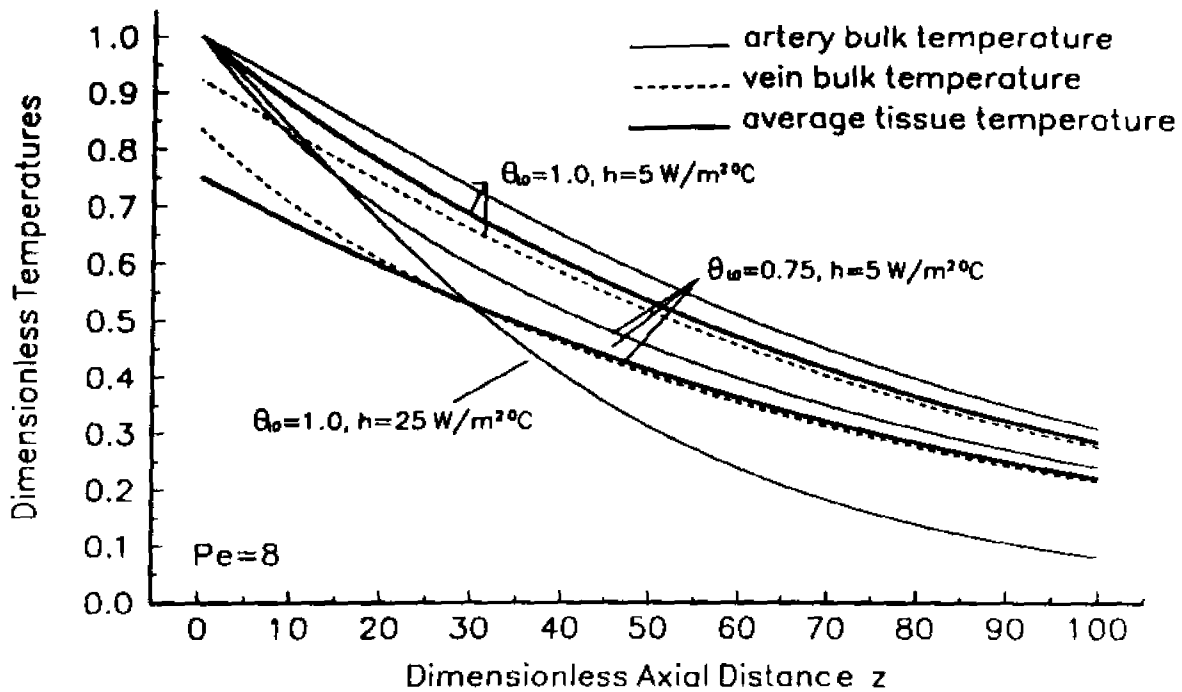

Figure 14. The effect of inlet tissue temperature and convection coefficient on the axial temperature distribution. Note that Pe=8 and the dimensionless axial distance z is scaled by $\rho_a^*(k_a/k)^{0.5}$. The dimensionless artery bulk temperature at the entrance is always equal to 1.

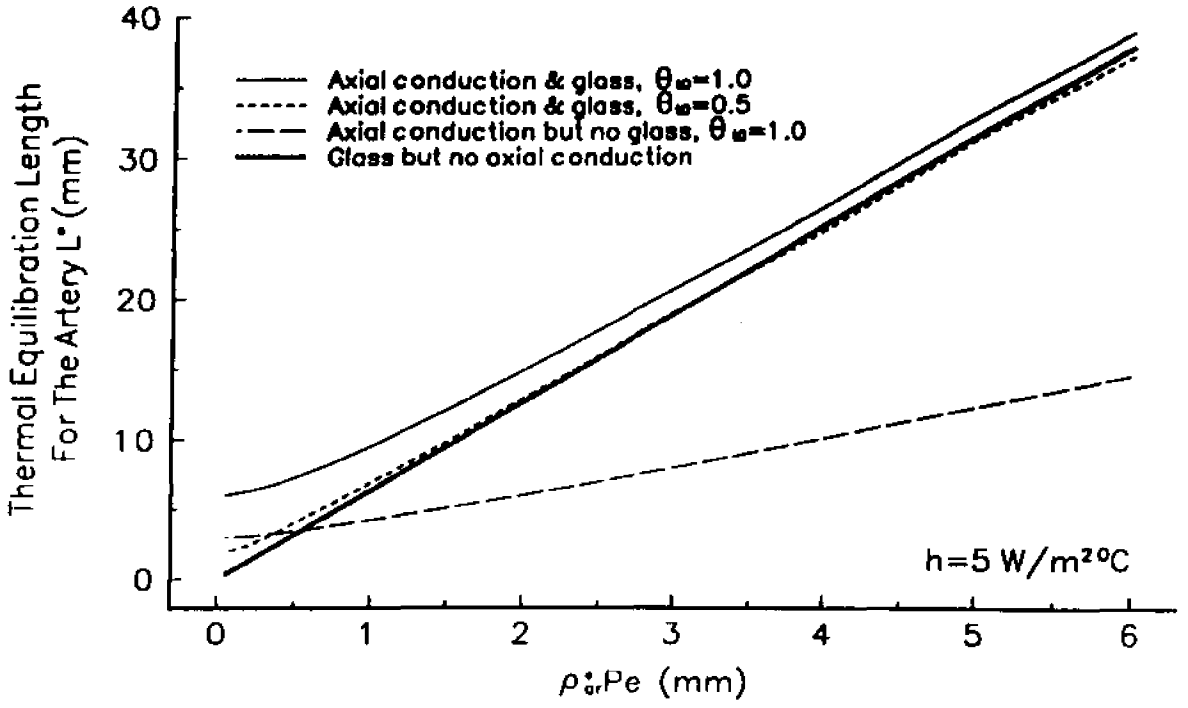

Figure 15. The effect of axial conduction and countercurrent flow on the axial thermal equilibration length for different ρ_a^*Pe.

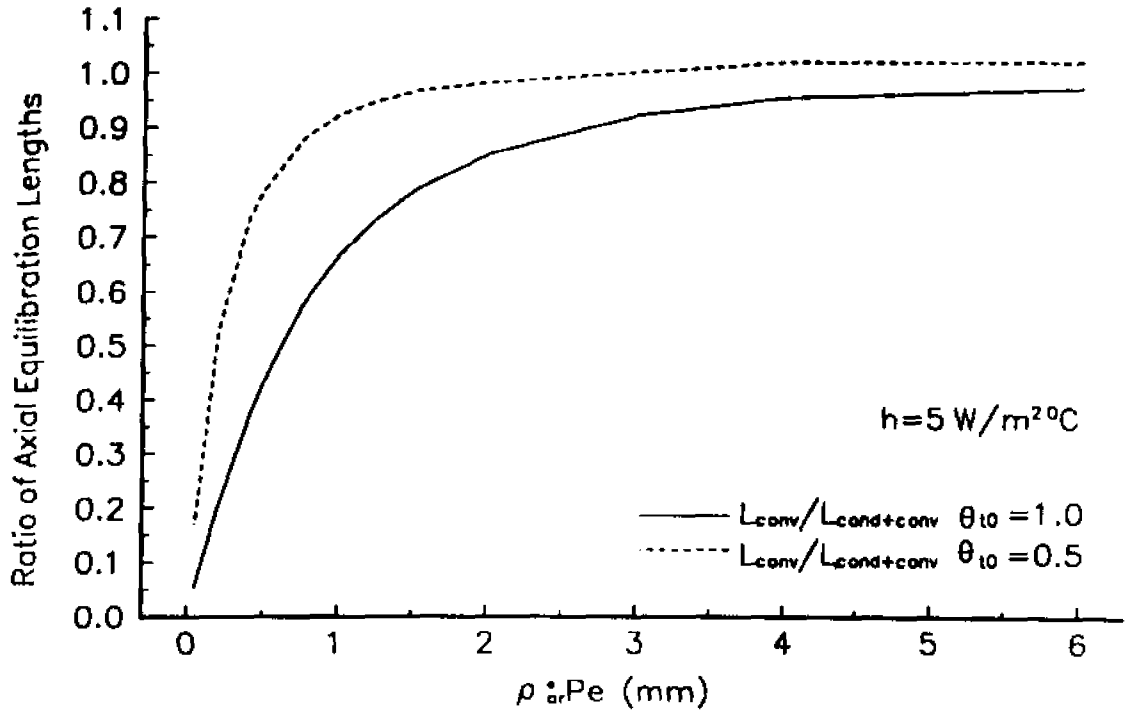

Figure 16. The percentage contributions of countercurrent flow and axial conduction to the axial thermal equilibration length at two values of tissue inlet temperature θ_{t0}=0.5 and 1.0. L_{conv} is the thermal equilibration length neglecting axial conduction (heavy solid line in Figure 15) and $L_{cond+conv}$ is the thermal equilibration length considering axial conduction (solid and short dashed line in Figure 15).

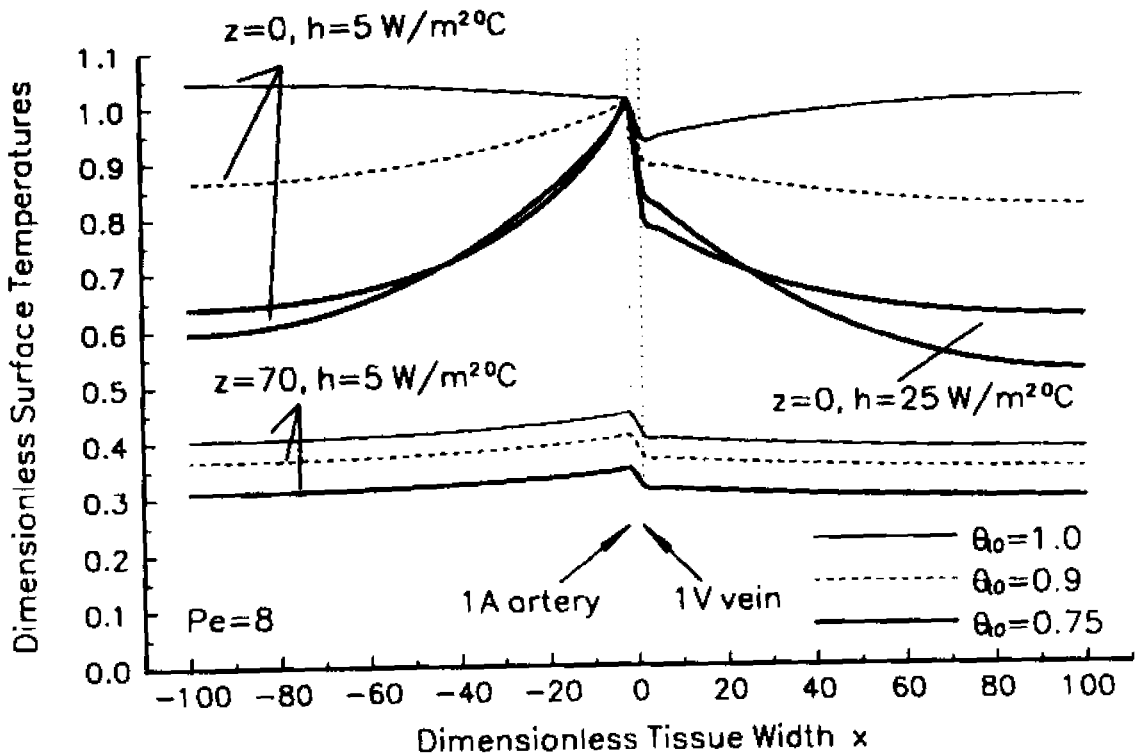

Figure 17. Surface temperature profiles at different axial locations (z=0, 70) for different inlet tissue temperatures and convective coefficients. (Pe=8)

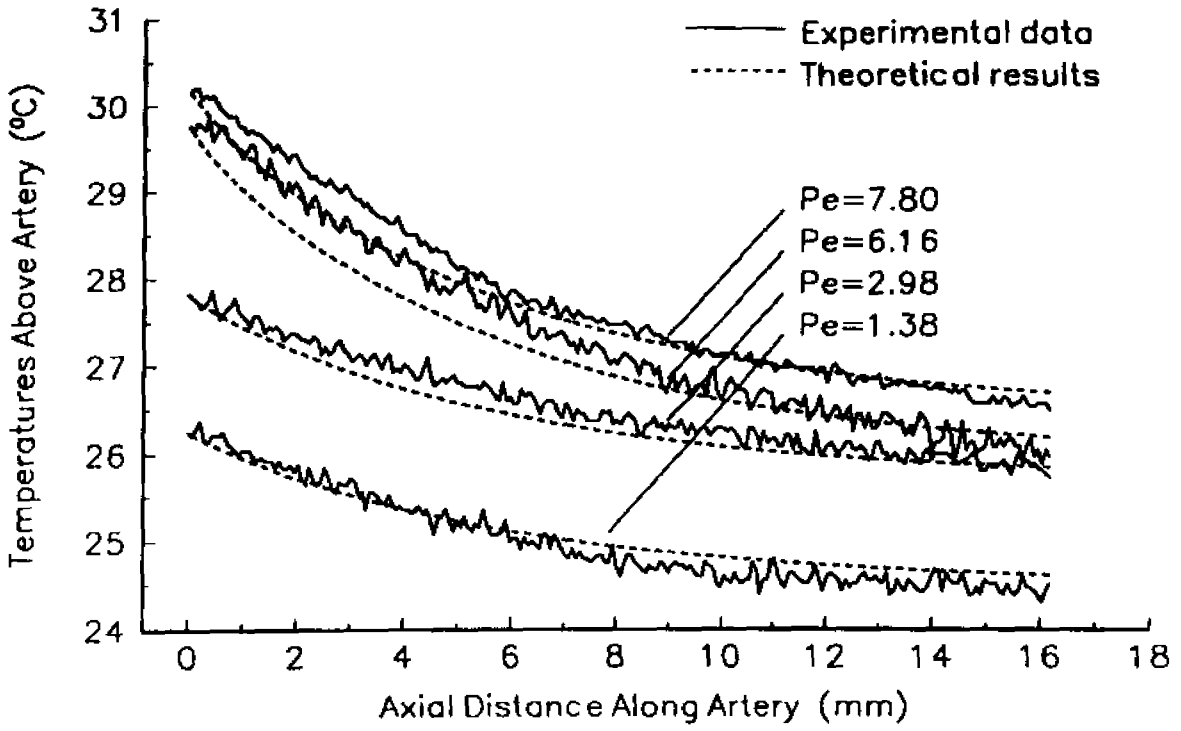

Figure 18. Comparison of the theoretical and experimental results for axial surface temperature decay at different blood flow Peclet numbers.

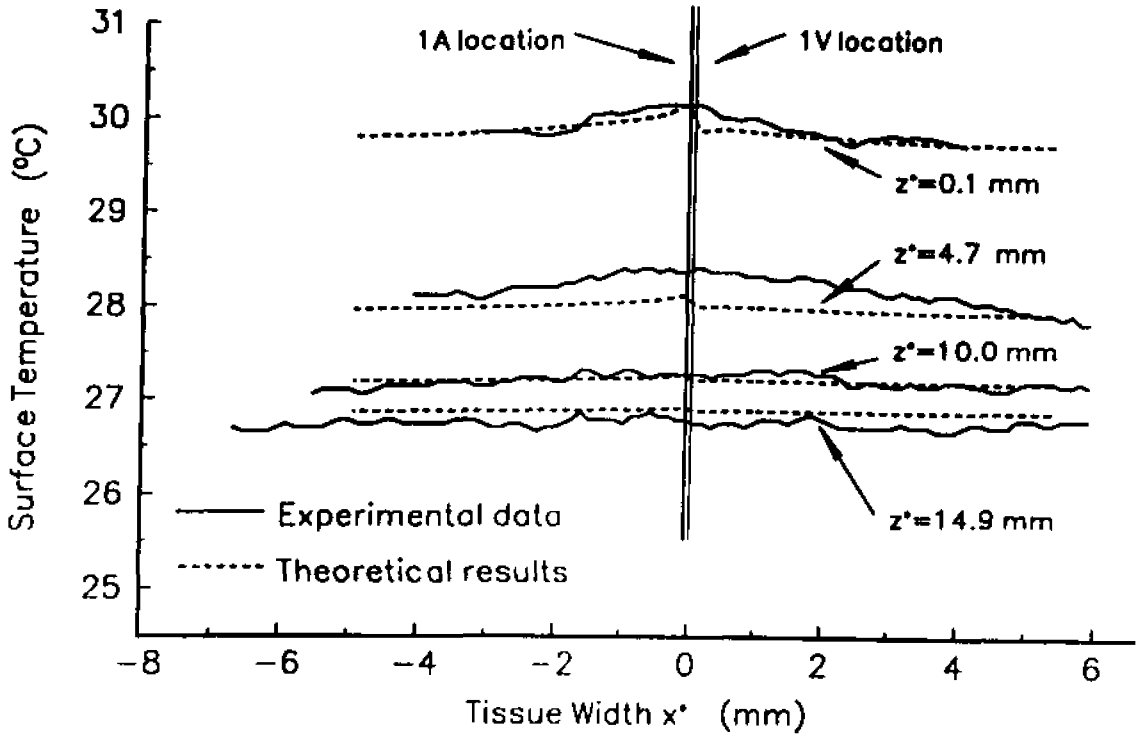

Figure 19. Comparisons of the theoretical and experimental results for the surface temperature profiles at four different axial locations.

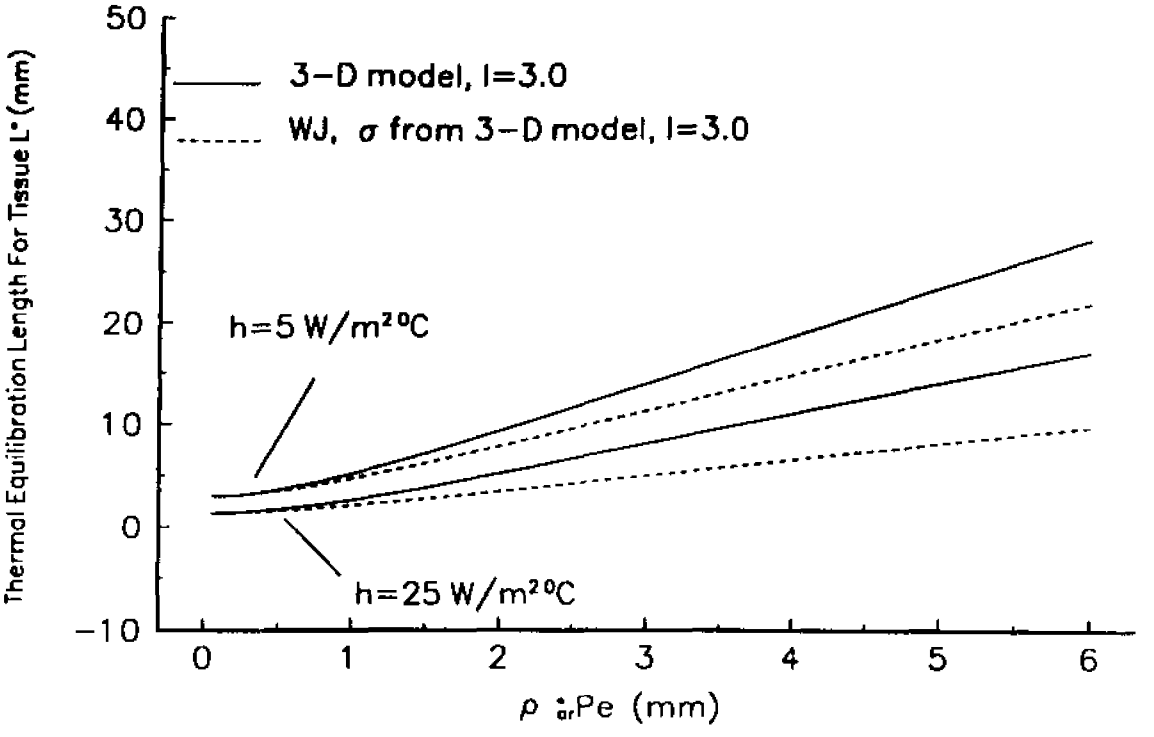

Figure 20. Comparison of tissue axial thermal equilibration lengths using present 3-D theoretical model and 1-D Weinbaum-Jiji model as a function of ρ_w*Pe for different convective coefficients *h*. Note that the average tissue temperature at the entrance z=0 is selected such that $d\theta_{t,av}/dz = d[(\theta_{ab}+\theta_{vb})/2]/dz$.

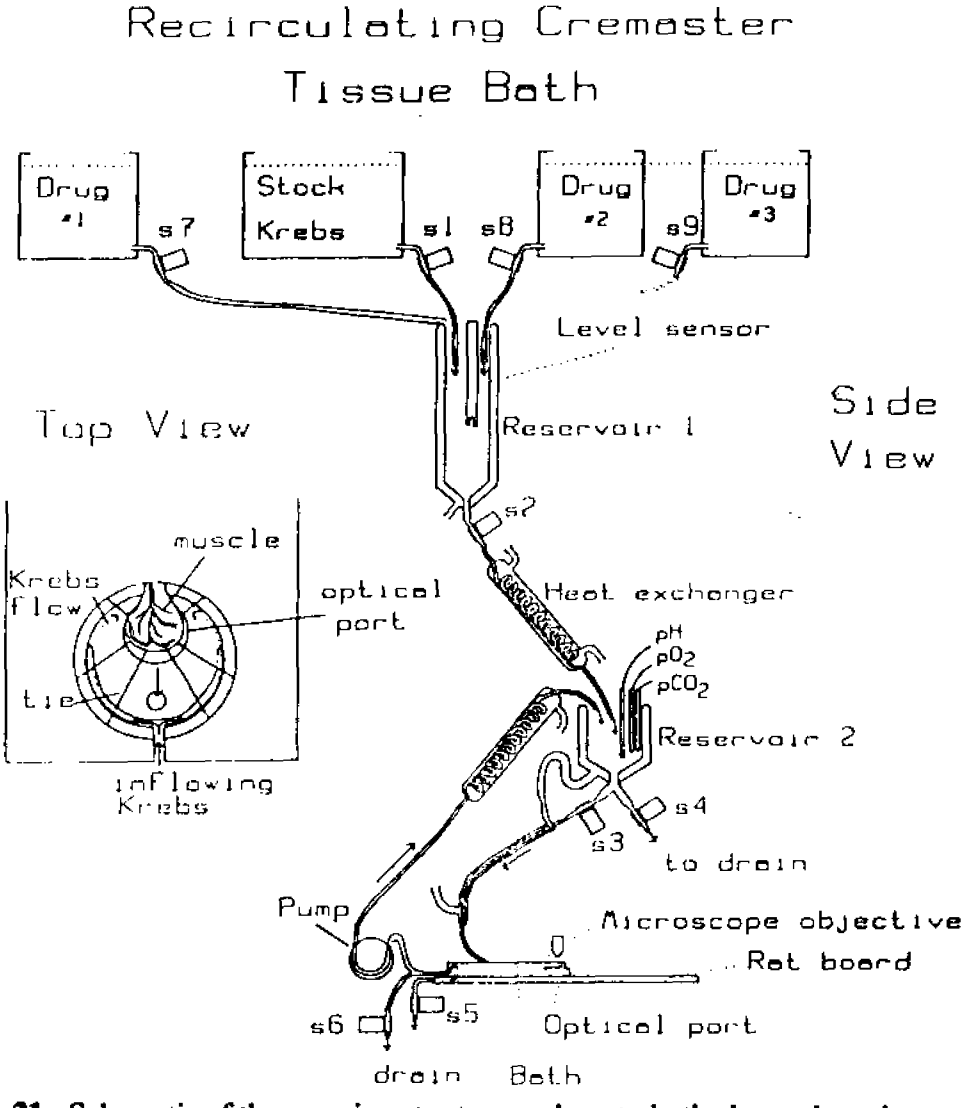

Figure 21. Schematic of the experiment setup used to study the hyperthermic response in rat cremaster muscle preparation.

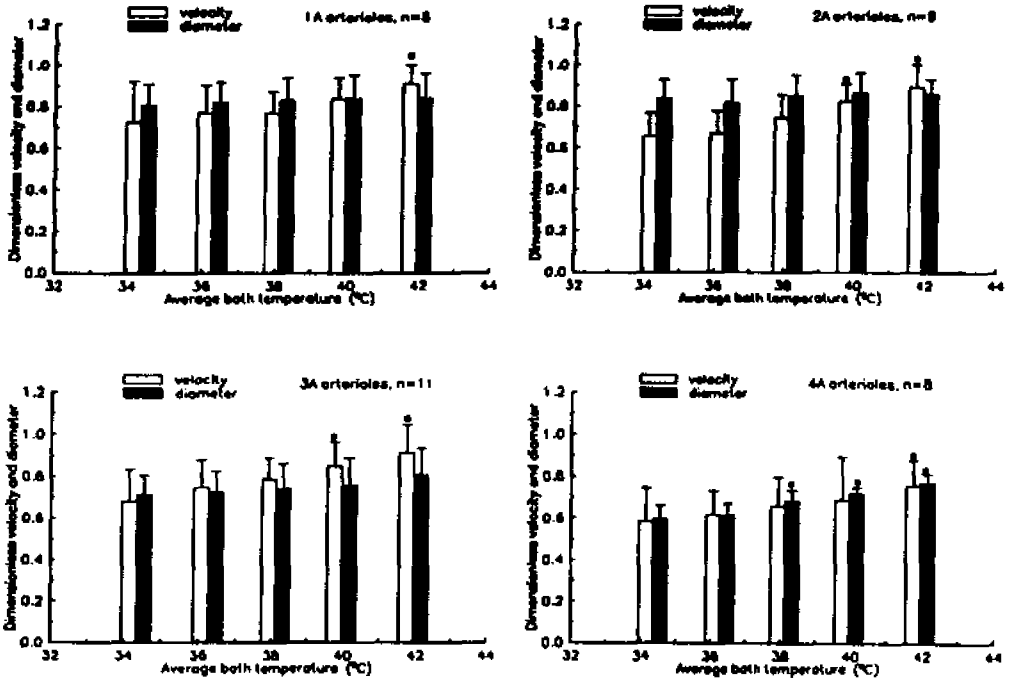

Figure 22. Temperature-dependence of diameter and centerline velocity for 1A, 2A, 3A, and 4A arterioles for direct thermal response. The data were normalized to the maximum dilation induced by Na nitroprusside ($10^{-4.5}$M). Vertical bars denote means±SD. * Diameter or velocity that was significantly different ($P<0.05$) from those at control temperature (34°C).

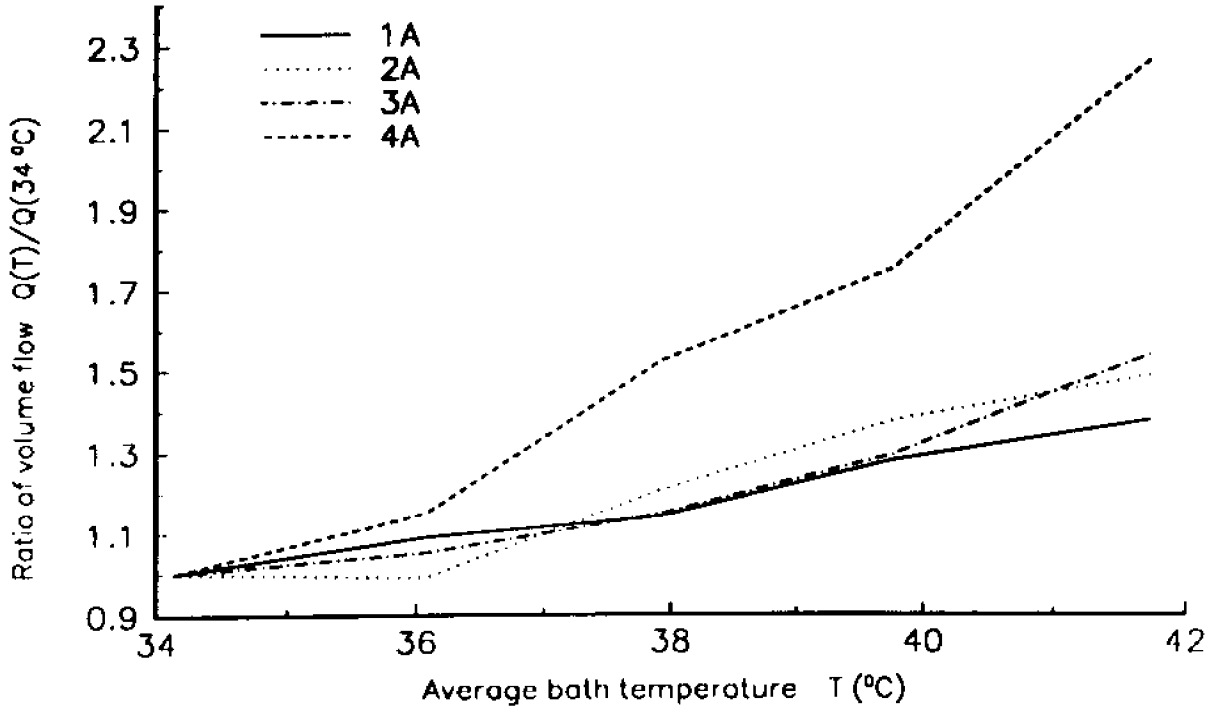

Figure 23. Volume flow changes over the control state (34°C) as a function of local tissue temperature for 1A, 2A, 3A, and 4A arterioles due to direct thermal response.

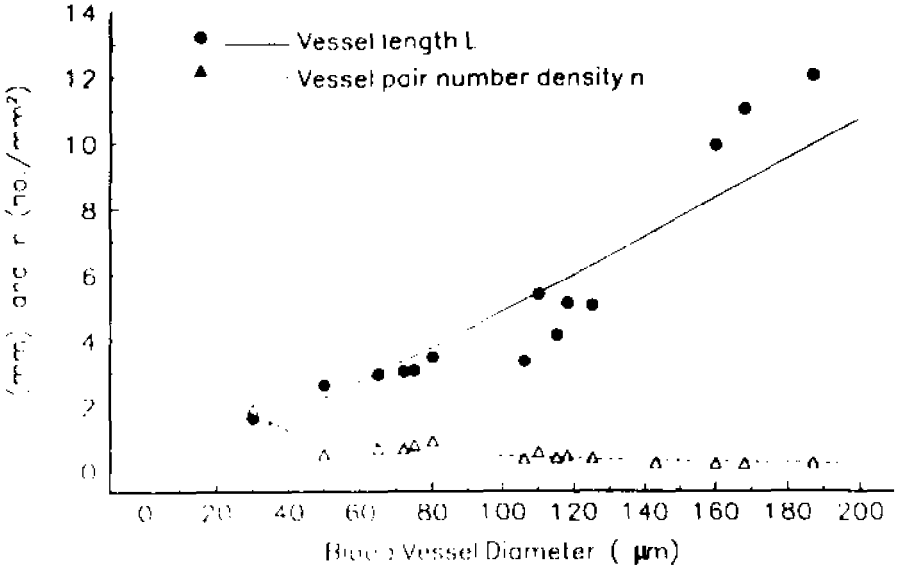

Figure 24. Measurements of vessel L (mm) and vessel pair number density n (no. mm^{-2}) from the photomontages of five rat cremaster muscel preparations. Lines are their regression curves.

Bibliography

1. Anderson, G. T., and J. W. Valvano, A small artery heat transfer model for self-heated thermistor measurements of perfusion in the kidney cortex. ASME *Journal of Biomechanical Engineering*, 116:71-78, 1994.

2. Anderson, G. T., J. W. Valvano, and R. R. Santos. Self-heated thermistor measurements of perfusion. *IEEE Transactions on Biomedical Engineering*, 39(9):877-885, 1992.

3. Baez, S.. A open cremaster muscle preparation for the study of blood vessels by *in vivo* microscopy. *Microvasc. Res.*, 5:384-394, 1973.

4. Baish, J. W., P. S. Ayyaswamy, and K. R. Foster. Heat transport mechanism in vascular tissues: a model comparison. ASME *Journal of Biomechanical Engineering*, 108:324-331, 1986.

5. Baish, J. W., P. S. Ayyaswamy, and K. R. Foster. Small-scale temperature fluctuations in perfused tissue during local hyperthermia. ASME *Journal of Biomechanical Engineering*, 108:246-250, 1986.

6. Baker, M., and H. Wayland. On-line volume flow rate and velocity profile measurement for blood in microvessels. *Microvasc. Res.*, 7:131-134, 1974.

7. Balasubramaniam, T. A., and H. F. Bowman. Thermal conductivity and thermal diffusivity of biomaterials: a simultaneous measurement technique. ASME *Journal of Biomechanical Engineering*, 99:148-154, 1977.

8. Bazett, H. C., I. Love, M. Newton, I. Eisenberg, R. Day, and R. Forest. Temperature changes in blood flowing in the arteries and veins in man. *J. Appl. Physiol.*, 1:3-19, 1948.

9. Chato, J. C.. A method for the measurement of thermal properties of biologic materials. *Symposium on Thermal Problems in Biotechnology*, ASME, N.Y., LCN068-58741, 1968, pp.16-25.

10. Chato, J. C.. Heat transfer to blood vessels. ASME *Journal of Biomechanical Engineering*, 102:110-118, 1980.

11. Charny, C. K., S. Weinbaum, and R. L. Levin. An evaluation of the Weinbaum-Jiji bioheat equation for normal and hyperthermic conditions. ASME *J. Biomechanical Engineering*, 112:80-87, 1990.

12. Chen, M. M., and K. K. Holmes. Microvascular contributions to tissue heat transfer. *Annals of the NY Acad. of Science*, 335:137-150, 1980.

13. Crezee, J., J. Mooibroek, J. J. W. Lagendijk, and G. M. J. van Leeuwen. The theoretical and experimental evaluation of the heat balance in perfused tissue.*Phys. Med. Biol.* 39:813-832, 1994.

14. Crezee, J., J Mooibroek, C. K. Bos, and J. J. W. Lagendijk. Interstitial heating: experiments in articially perfused bovine tongues. *Physics in Medicine and Biology*, 36:823-833, 1991.

15. Crezee, J., and J. J. W. Lagendijk. Experimental verification of bioheat transfer theories: measurement of temperature profiles around large artificial vessels in perfused tissue. *Physics in Medicine and Biology*, 35(7):905-923, 1990.

16. DiFelice, R. F. Jr., and H. H. Bau. Conductive heat transfer between eccentric cylinders with boundary conditions of the third kind. *J. Heat Transfer*, 105:678-680, 1983.

17. Engelson, E. T., T. C. Skalak, and G. W. Schmid-Schonbein. The microvasculature in skeletal muscle: I. arteriolar network in rat spinotrapezius muscle. *Microvasc. Res.*, 30:29-44, 1985.

18. Faber, J. E.. *In situ* analysis of α-adrenoceptors on arteriolar and venular smooth muscle in rat skeletal muscle microcirculation. *Circ. Res.*, 62:37-50, 1988.

19. Flavahan, N. A., and P. M. Vanhoutte. Effect of cooling on alpha-1 and alpha-2 adrenergic responses in canine saphenous and femoral veins. *J. Pharm. Exp. Ther.* 238:139-147, 1986.

20. Hahne, E., and U. Grigull. A shape factor scheme for point source configurations. *Int. J. Heat Mass Transfer*, 17:267-273, 1974.

21. Hogan, R. D., T. D. Franklin, K. S. Avery, and K. M. Burke. Arteriolar vasoconstriction in rat cremaster muscle induced by local heat stress. *Am. J. Physiol.*, 242:H996-H999, 1982.

22. House, S. D., and H. H. Lipowsky. Microvascular hematocrit and red cell flux in rat cremaster muscle. *Am. J. Physiol.*, 252:H211-H222, 1987.

23. Jain, R. K., and K. A. Ward-Hartley. Tumor blood flow: characterization, modifications, and role in hyperthermia. *IEEE Trans.*, SU-31, 1984, pp. 504-526.

24. Kamiya, A., R. Bukhari, and T. Togawa. Adaptive regulation of wall shear stress optimizing vascular tree function. *Bull. Math. Biol.*, 46:127-137, 1984.

25. Lemons, D. E., S. Chien, L. I. Crawshaw, S. Weinbaum, and L. M. Jiji. The significance of vessel size and type in vascular heat transfer. *Am. J. Physiol.*, 253:R128-R135, 1987.

26. Meininger, G. A., K. L. Fehr, and M. B. Yates. Anatomic and hemodynamic characteristics of the blood vessels feeding the cremaster skeletal muscle in the rat. *Microvascular Research*, 33:81-97, 1987.

27. Mitchell, J. W., and G. R. Myers. An analytical model of the counter-current heat exchange phenomena. *Biophysical Journal*, 8:897-911, 1968.

28. Patel, P. A., J. W. Valvano, J. A. Pearce, S. A. Prahl, and C. R. Denham. A self-heated thermistor technique to measure effective thermal properties from the tissue surface. ASME *Journal of Biomechanical Engineering*, 109:330-335, 1987.

29. Pennes, H. H.. Analysis of tissue and arterial blood temperatures in the resting human forearm. *J. Applied Physiology*, 1:93-122, 1948.

30. Roemer, R. B., E. G. Moros, and K. Hynynen. A comparison of bio-heat transfer and effective conductivity equation predictions to experimental hyperthermia data. *Adv. Bioeng.*, ASME WAM, pp11-15, 1989.

31. Scholander, P. F. and J. Krog. Countercurrent heat exchange and vascular bundles in sloths. *J. Appl. Physiol.* 10:405-411, 1957.

32. Thiyagarajan, R. and M. M. Yovanovich. Thermal resistance of a buried cylinder with constant flux boundary condition. *J. Heat Transfer*, 96:249-250, 1974.

33. Valvano, J. W., J. T. Allen, and H. F. Bowman. The simultaneous measurement of thermal conductivity, thermal diffusivity and perfusion in small volumes of tissue. ASME *Journal of Biomechanical Engineering*, 106:192-197, 1984.

34. Vanhoutte, P. M., "Physical factors of regulation," In *handbook of physiology*, Section 2, Circulation, Vol. 2, Vascular smooth muscle, ed. Bohr, D. F., Somlyo, A. P. and Sparks, H. V., pp. 443-474, 1980.

35. Weinbaum, S., and L. M. Jiji. The matching of thermal fields surrounding countercurrent microvessels and the closure approximation in the Weinbaum-Jiji bioheat equation. ASME *Journal of Biomechanical Engineering*, 111:271-275, 1989.

36. Weinbaum, S., and L. Jiji. A new simplified bioheat equation for the effect of blood flow on average tissue temperature. ASME *Journal of Biomechanical Engineering*, 107:131-139, 1985.

37. Weinbaum, S., L. Jiji, and D. E. Lemons. Theory and experiment for the effect of

vascular microstructure on surface tissue heat transfer -- Part 1: anatomical foundation and model conceptualization. ASME *Journal of Biomechanical Engineering*, 106:321-330, 1984.

38. Wallenstein, S., C. L. Zucker, and J. L. Flwiss. Some statistical methods useful in circulation research. *Circulation Res.*, 47:1-9, 1980.

39. Wissler, E. H.. An analytical solution countercurrent heat transfer between parallel vessels with a linear axial temperature gradient. ASME *J. Biomechanical. Eng.*, 110:254-256, 1988.

40. Wu, Y. L., S. Weinbaum, and L. M. Jiji. A new analytic technique for 3-D heat transfer from a cylinder with two or more axially interacting eccentrically embedded vessels with application to countercurrent blood flow. *Int. J. Heat Mass Transfer*, 36:1073-1083, 1993.

41. Xu, L. X., M. M. Chen, K. R. Holmes, and H. Arkin. The theoretical evaluation of the Pennes, the Chen-Holmes and the Weinbaum-Jiji bioheat transfer models in the pig renal cortex. ASME Winter Annual Meeting, Atlanta, HTD-Vol. 189, pp. 15-22, 1991.

42. Zhu, M., S. Weinbaum, and L. M. Jiji. Heat exchange between unequal countercurrent vessels asymmetrically embedded in a cylinder with surface convection. *Int. J. Heat Mass Transfer*, 33:2275-2284, 1990.

43. Zhu, M., S. Weinbaum, L. M. Jiji, and D. E. Lemons. On the generalization of the Weinbaum-Jiji bioheat equation to microvessels of unequal size; the relation between the near field and local average tissue temperature. ASME *Journal of Biomechanical Engineering*, 110:74-81, 1988.

44. Zweifach, B. W., and H. H. Lipowsky. Quantitative studies of microcirculatory structure and function: III. microvascular hemodynamics of cat mesentery and rabbit omentum. *Circulation Research*, 41(3):380-390, 1977.